Atomic-Scale Visualisation of Fermion-Pair Condensates in Strongly Correlated Quantum Materials

Wangping Ren

St. Catherine's College

University of Oxford

A thesis submitted for the degree of

Doctor of Philosophy

Trinity 2023

In memory of my grandma, Li Gongyi.

Acknowledgements

First and foremost, I would like to thank my mom, M. Chen, and my dad, Q. Ren, for their endless support and love. Covid-19 had kept me thousands of miles away from them for almost four years. Their faith in me to pursue my dream as a scientist has been the strongest encouragement. I thank my family for always being by my side. This thesis is dedicated to them.

As the first DPhil student in the Davis group, Oxford, who started from a new and empty lab space, I feel fortunate to be part of a truly international group; the help, support, and guidance I received from colleagues in Oxford (UK), Cork (Ireland) and Ithaca (US) could not be emphasized enough.

I am grateful to members of the Davis group at Oxford with whom I share unforgettable memories. The development of the Gemini STM was in close collaboration with two postdocs, Shuqiu Wang and Weijiong Chen. I thank them for teaching me most of the laboratory skills and problem-solving approaches I learned. Among all doctoral students in the Davis group, Niall Kennedy has had the most time overlap with me. It was a pleasure working with him during his visits to Oxford. Sam O'Sullivan joined the Gemini team in my final year, and I was fortunate to have collaborated with her. I thank Harris Pirie for always being willing to help and sharing his STM expertise freely. I especially thank him for introducing me to the Python programming language for STM data analysis. I thank Chun-Chih Hsu, Hiroto Takahashi and Yutong Dai for sharing the basement lab with me. The conversations we had down in the Beecroft basement were most enjoyable. And, of course, all the fun times having 'hot pot' dinners that we had. Many thanks also go to Jack Enright, Jan Knapp, and Fabian Jerzembeck, who provided great sources of help. I would also like to thank the staff members in the Oxford physics department, especially Pierre Van Zijl, David Sharp, Bradley Harsant, Robert Storey, Kieran McCall, Paul Bircher and Mike Tacon. Their support is instrumental to the successful construction and operation of the instrument.

In the Cork team, I was lucky to have worked most closely with Shane O'Mahony, with whom we made important discoveries on the mechanism of the cuprate superconductor. I thank him for all our stimulating discussions and all the hard work we put into tackling this challenging problem. I thank two amazing post-docs at the Aquilon STM team – Jiahao Yan and Ge He. Not only did I learn a lot from

them on the technical details, but their creativity and self-motivation in solving challenging problems set a role model for me. Many thanks also to my colleagues and friends in the UCC lab, who have helped me and had stimulating conversations with me during my DPhil – Siyuan Wan, Catherine Dawson, Huiyu Zhao, Joe Carroll, Jonathan Ward, Jahn Dasini, Jack Murphy and Reza Arkani.

At Cornell, I thank Xiaolong Liu, Yi Xue Chong and Ruhul Shama, who provided help and guidance to me during the initial stages of my DPhil. I thank Qiangqiang Gu for the helpful discussions.

I thank all my friends at Oxford for all our enjoyable moments and my friends outside Britain for all the fun remote hangouts. With their support, my DPhil journey couldn't have been richer.

Finally, I would like to extend my sincere gratitude to my advisor, Professor Séamus Davis. He has not only taught me to sharpen my goals and think strategically but also to ask the right questions and persevere until answers are found. Graduate school is a mix of fun and frustrations, and he always left me motivated after each meeting. His unwavering passion for science is a continual source of inspiration for me.

Abstract

Since its discovery in 1986, high-temperature superconductivity in copper oxides has puzzled researchers. Its intricate phase diagram, which unveils unusual physical properties, is particularly challenging to understand because of its strongly correlated nature. Despite numerous efforts, a consensus on the mechanism that forms electron-pair condensate underpinning the high-temperature superconductivity remains elusive. The research presented in this thesis endeavours to shed new light on the electron-pairing mechanism.

In this thesis, I use advanced scanning tunnelling microscopy (STM) techniques to study the mechanisms behind the high-temperature superconductor $Bi_2Sr_2CaCu_2O_{8+x}$ (Bi-2212). Chapter 1 presents an introduction to conventional superconductivity which leads to a review of the cuprate superconductivity from both theory and experiment. Chapter 2 is devoted to introducing two novel STM techniques that are instrumental to the scientific findings presented in this thesis. In Chapter 3, I present the development of a next-generation STM, Gemini, that I built and operated during my DPhil. This home-built STM is designed to function at milli-kelvin temperatures with a 14 Tesla superconducting magnet. An in-depth examination of the design details and various testing results are presented. In Chapter 4, using the innovative STM techniques, an experimental discovery of an exotic quantum state in optimally doped Bi-2212 called the nematic pair-density wave (PDW) state is presented. Towards identifying the electron-pairing mechanism in Bi-2212, Chapter 5 first introduces a modern numerical technique called the dynamical mean-field theory (DMFT) that predicts the paring mechanism as the charge-transfer superexchange interaction. Then, this chapter presents an analogue isotope effect experiment that identifies the distance between the Cu atom and its apical O atom as the tuning parameter that alters the pairing strength. The anti-correlation relationship between the charge-transfer energy and the pairing amplitude is established whose slope conforms to the predictions of DMFT, which indicates that the charge-transfer superexchange interaction is key to the electron-pairing mechanism in optimally doped Bi-2212. Lastly, in Chapter 6, I present my recent STM experiments on candidate excitonic insulator $1T$-$TiSe_2$. The results reveal directly the charge-transfer process between the Ti and Se atoms which is responsible for exciton formation. Furthermore, visualisation of the excitonic energy gap reveals a highly heterogeneous spatial pattern inconsistent with a conventional CDW but which indicates strong electron-electron interactions.

Contents

List of Figures

List of Abbreviations

1D, 2D, 3D . . One- , two or three-dimension
4KP . . . . . 4-kelvin plate
1KP . . . . . 1-kelvin plate
ARPES . . . . Angle-resolved photoemission spectroscopy
Bi-2212 . . . . $Bi_2Sr_2CaCu_2O_{8+x}$
CDW . . . . . Charge-density wave
c-DMFT . . . Cluster-dynamical mean-field theory
CAD . . . . . Computer-aided design
DOS . . . . . Density of states
DR . . . . . Dilution refrigerator
DLRO . . . . . Diagonal long-range order
DMFT . . . . Dynamical mean-field theory
FOV . . . . . Field of view
LHe . . . . . Liquid helium
LDOS . . . . . Local density of states
LLC . . . . . Load-lock chamber
NMR . . . . . Nuclear magnetic resonance
ODLRO . . . . Off-diagonal long-range order
PDW . . . . . Pair-density wave
PID . . . . . Proportional–integral–derivative
PG . . . . . Pseudogap
RVB . . . . . Resonating valence bound
STM . . . . . Scanning tunnelling microscopy
SJTM . . . . . Scanned Josephson tunnelling microscopy
SNR . . . . . Signal-to-noise ratio
ZRS . . . . . Zhang-Rice singlet

It was long believed that the wave function of the Schrödinger equation would never have a macroscopic representation analogous to the macroscopic representation of the amplitude for photons. On the other hand, it is now realized that the phenomenon of superconductivity presents us with just this situation.

— The Feynman lectures on physics [1]

1 The cuprate problem

Contents

In this chapter, I will introduce the theory of conventional superconductivity, followed by the modern understanding of unconventional cuprate superconductors and the remaining challenges. This chapter also laid the foundations for understanding my experimental findings of the essential ingredient behind the electron-pairing mechanism in a cuprate superconductor presented in Chapter 5 of this thesis.

In 1911, Dutch physicist Heike Kamerlingh-Onnes discovered superconductivity - a phenomenon where materials conduct electricity with zero resistance at temperatures near that of liquid helium. We now understand that the material has undergone a phase transition from a normal conductor to a new phase of matter - a superconducting phase below a critical temperature T_c. This new superconducting

phase is a direct manifestation of the macroscopic quantum phenomenon where electrons are bound to form pairs and condense into a zero momentum ground state. Forty years after its discovery, direct experimental evidence showed that T_c scales with the square root of the isotopic mass [2], directly confirming the critical role of lattice vibrations in the mechanism of electron pairing in conventional superconductors.

Since the discovery of High-temperature copper-oxide superconductors (the cuprates) in the 1980s, one of the biggest challenges in contemporary physics research is to identify the mechanism that binds the electrons so strongly that it sustains superconductivity at such high temperatures. Despite decades of research, no consensus has been made on the mechanism behind electron pairing in these superconductors.

1.1 Superconductivity: an introduction

1.1.1 Ginzburg-Landau theory

Superconductivity is a direct manifestation of quantum phenomena at a macroscopic scale. It exhibits two characteristic properties - zero resistivity and perfect diamagnetism (the Meissner effect). Normal matter has to go through a phase transition to reach the superconducting state from the normal state, a process which involves the concept of broken symmetry. Without knowing the details of the superconducting mechanism, Ginzburg and Landau were able to describe its thermodynamic and electromagnetic properties based solely on a phenomenological theory.

Ginzburg and Landau realised that a macroscopic phenomenon such as superconductivity could be described by a complex order parameter $\psi(\mathbf{r}) = |\psi(\mathbf{r})|e^{i\phi(\mathbf{r})}$, where ϕ being the phase, which is zero in the normal state above T_c and finite below T_c. They postulate that the physical properties of a superconductor can be completely described by the free energy of the form

$$\mathcal{F} = \mathcal{F}_n + \frac{1}{2m^*}\left|(-i\hbar\nabla - e^*\mathbf{A})\,\Psi\right|^2 + \alpha|\Psi|^2 + \frac{\beta}{2}|\Psi|^4 + \frac{\mathbf{H}^2}{2\mu_0} \tag{1.1}$$

where $\mathcal{F}_n$ is the free energy in the normal state, $\mathbf{A}$ is the vector potential, $\mathbf{H}$ is the external magnetic field, m^* and e^* are the effective mass and charge respectively[1] and $-i\hbar\nabla - e^*\mathbf{A}$ is the canonical momentum. Physically, $|\Psi|^2$ is proportional to the superfluid density near T_c. The free energy functional can be minimised with respect to Ψ. Assuming the presence of no magnetic field and the spatial variation of Ψ is negligible, the solution of $\delta\mathcal{F} = 0$ gives

$$|\Psi| = \begin{cases} 0, & T > T_{\mathrm{c}} \\ \left[\alpha\left(T_{\mathrm{c}} - T\right)/\beta\right]^{1/2}, & T < T_{\mathrm{c}} \end{cases} \tag{1.2}$$

where $\beta > 0$ and $\alpha = |\alpha|\left(T - T_{\mathrm{c}}\right)$. Here, the superconducting system described by the order parameter Ψ is said to have undergone *spontaneous symmetry breaking*. This is because if the order parameter is multiplied by an additional phase factor $e^{i\theta}$, though the free energy functional is invariant under this phase gauge transformation, the order parameter acquires an additional phase θ in the superconducting state, i.e. $\Psi \to \Psi\exp(i\theta) \neq \Psi$, which is still zero in the normal state. The gauge symmetry exhibited in the original functional is now spontaneously broken.

Next, if the free energy is minimised with respect to $\mathbf{A}$, we have the current density in the superconducting state

$$\mathbf{J_s} = \frac{2e^2|\psi|^2}{m}\left(\mathbf{A} - \frac{\hbar}{2e}\nabla\theta\right). \tag{1.3}$$

Taking the curl of the above equation and using Maxwell's equation, we can solve for the external field $\mathbf{H}$ that is perpendicular to the superconductor's surface (z direction). Then we have [3]

$$H(z) = H(0)\mathrm{e}^{-z/\lambda}, j_{\mathrm{s}} = \frac{\mathrm{d}H}{\mathrm{d}z} = j_{\mathrm{s}}(0)\mathrm{e}^{-z/\lambda} \tag{1.4}$$

with the penetration depth defined as

$$\lambda = \sqrt{\frac{m\beta}{2\mu_0|\alpha|e^2}}. \tag{1.5}$$

This suggests that an external magnetic field can only penetrate a superconductor by a small length λ and vanishes in the bulk. This is exactly the Meissner effect[2].

[1] It turns out that $e^* = 2e$ and $m^* = 2m_e$ due to the formation of electron pairs. This can be verified, for example, by measuring the flux quanta ($\Phi_0 = \frac{h}{2e}$) through a superconducting ring.

[2] More fundamentally, the Meissner effect is related to the Anderson-Higgs mechanism where the photon acquires mass along the longitudinal propagation direction inside a superconductor, in which the external field becomes massive and decays on the scale of λ.

1.1.2 Off-diagonal long-range order

It was suggested by Yang [4] that the appearance of a macroscopic quantum phenomenon is due to the onset of the *off-diagonal long-range order* (ODLRO). For superconductivity, it can be described by a two-particle reduced density matrix [5]

$$\rho_2(\mathbf{r},\mathbf{r}') = \left\langle \psi_\alpha^\dagger(\mathbf{r})\psi_\beta^\dagger(\mathbf{r})\psi_\alpha(\mathbf{r}')\,\psi_\beta(\mathbf{r}') \right\rangle \tag{1.6}$$

where $\psi_\alpha^\dagger(\mathbf{r})$ and $\psi_\alpha(\mathbf{r})$ are particle creation and annihilation operators with spin index α, and the expectation value is taken with respect to the superconducting ground state. Physically, this off-diagonal density matrix represents the correlation between creating and annihilating a particle pair at position $\mathbf{r}$ and $\mathbf{r}'$, respectively. If $\rho_2(\mathbf{r},\mathbf{r}')$ does not vanish even if the two-particle pairs are far apart, i.e. $|\mathbf{r}-\mathbf{r}'| \to \infty$, it is said that ODLRO has occurred. Note that ODLRO is distinct from the classical long-range order in solids where the density matrix is in diagonal form, such as the charge density.

Assuming that the two-particle pairs can be treated independently for a particle pair with opposite spins, Eqn. 1.6 can be written as

$$\rho_2(\mathbf{r},\mathbf{r}') = \left\langle \psi_\downarrow^\dagger(\mathbf{r})\psi_\uparrow^\dagger(\mathbf{r}) \right\rangle \langle \psi_\downarrow(\mathbf{r}')\,\psi_\uparrow(\mathbf{r}') \rangle \,. \tag{1.7}$$

Thus, a direct consequence of ODLRO is the non-vanishing expectation value of the particle correlator $\langle \psi_\downarrow(\mathbf{r})\psi_\uparrow(\mathbf{r}) \rangle$. This is consistent with the order parameter definition from the Ginzburg-Landau theory. We can then define a superconducting order parameter based on ODLRO as the following

$$\Psi = \langle c_{\mathbf{k}\uparrow} c_{-\mathbf{k}\downarrow} \rangle \tag{1.8}$$

where $c_\mathbf{k}$ is the Fourier transform of $\psi(\mathbf{r})$. As we will see in the next section, ODLRO is crucial in the microscopic description of superconductivity.

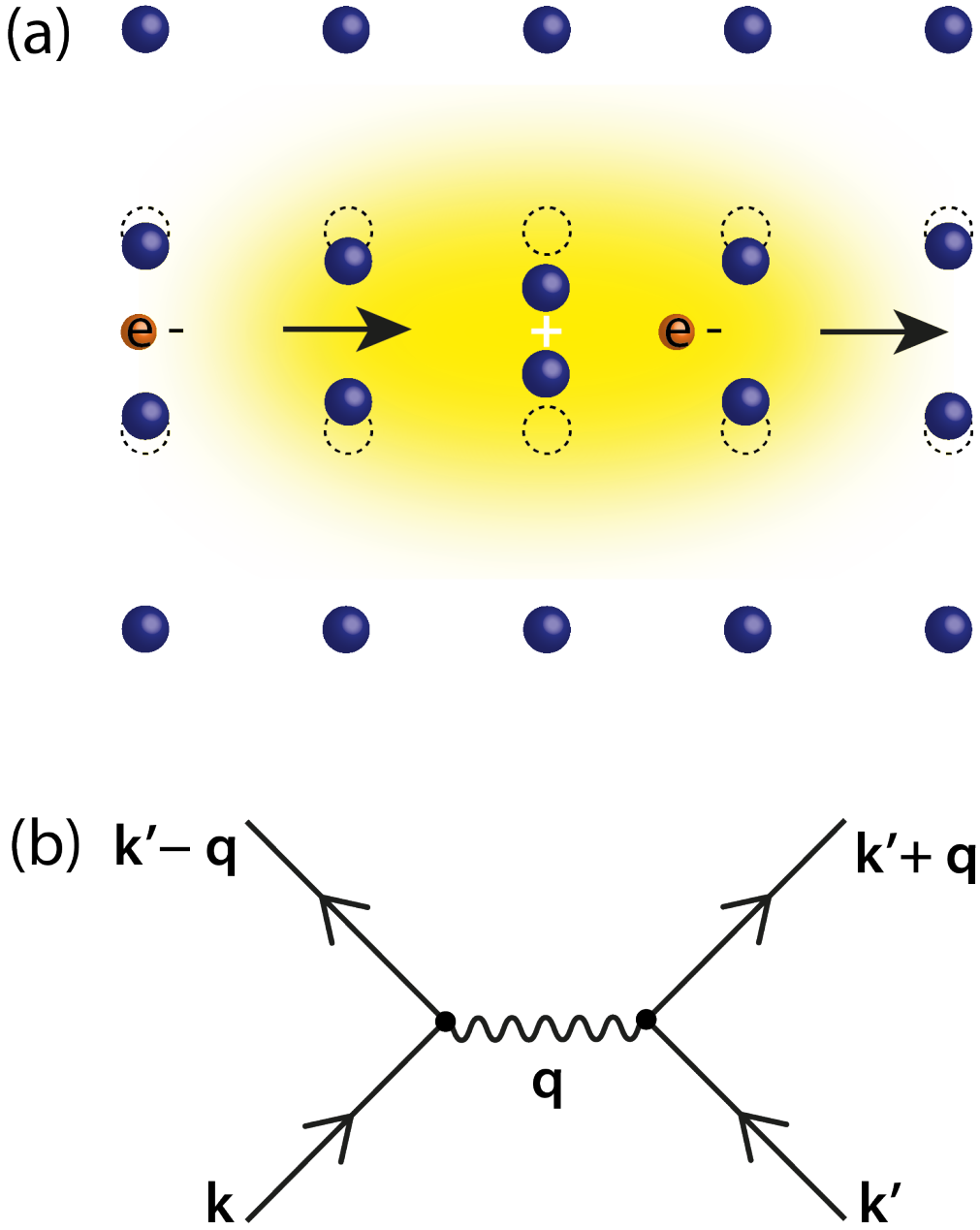

Figure 1.1: (a) Schematic of phonon-mediated electron-electron interaction. As an electron travels through the lattice, it pulls the positively charged ions away from their equilibrium positions due to attractive Coulomb interaction and thus creates a high positive charge density (yellow background), which then attracts the other electron. An effective electron-electron interaction is then established. (b) Feynman diagram of the electron-phonon interaction. An electron (solid line) with momentum $\mathbf{k}$ loses a phonon (wavy line) that is absorbed by another electron with momentum $\mathbf{k}'$.

1.1.3 BCS theory

Conventional superconductors such as simple metals Pb, Al, and Nb are well described by the BCS theory proposed by Bardeen, Cooper, and Schrieffer [6], which provides the first microscopic framework of superconductivity. An early hint of the superconducting mechanism came from the experimental discovery of the *isotope effect*. In 1950, Reynolds et al. [2] measured the superconducting transition temperature T_c of various mercury isotopes (^{199}Hg, ^{200}Hg, ^{202}Hg, ^{203}Hg). This experiment shows that T_c varies significantly with different unclear masses and provides direct evidence that lattice vibrations are a crucial ingredient in conventional superconductivity.

Later, it was physically realised that it is possible to have an effective, attractive interaction between two electrons due to lattice vibration despite the existing Coulomb repulsion. Firstly, because of the *screening effect*, a charge in a lattice system is dressed with a cloud of opposite charges, effectively reducing the long-range Coulomb potential to be short-ranged[3]. Secondly, as electrons travel through the lattice, they interact with the positive ions and thus create lattice vibrations. This phenomenon is visualised in Fig. 1.4(a). A travelling electron distorts the positive ions that create a localised positive charge density which then attracts another electron as the first electron moves away. This way, an effective attractive interaction is created between two electrons via the lattice vibration. In other words, this attractive electron interaction is mediated by the exchange of the lattice vibration quanta - the phonon, as depicted in the Feynman diagram Fig. 1.4(b). In reality, this electron-phonon interaction is not instantaneous. If the electron travelling speed is too fast so that the ions have little time to respond, the interaction would not be efficient. Thus, an upper bound is imposed on the electron energy, $\hbar\omega_D$, where ω_D is the characteristic Debye frequency of the lattice vibration.

The next hint comes from Cooper's [7] discovery in 1956. When two electrons are paired together by an attractive interaction in the presence of the electronic

[3]Typically, the magnitude of the screening length in a normal metal is on the order of the lattice constant.

Fermi sea, a bound state exists. Explicitly, by solving the Schrödinger equation of two electrons subject to an attractive interaction V ($V < 0$), the binding energy ϵ of the two electrons is given by

$$\Delta\epsilon = -2\hbar\omega_D e^{\frac{2}{N(0)V}} \tag{1.9}$$

where $N(0)$ is the density of states at the Fermi energy E_F and $\Delta\epsilon = \epsilon - E_F$. The above equation says that a bound state ($\Delta\epsilon < 0$) always exists no matter how weak the attractive interaction V is. This means that the usual ground state for a normal metal - the Ferimi sea is unstable under the presence of an attractive interaction since the formation of electron pairs lowers the energy. This pairing effect can easily extend to all other electrons until the lowest energy ground state is achieved. This is the *Cooper instability*. An important part of the BCS theory is to find out what this electron-pair ground state is.

Based on this Fermi surface instability, Bardeen, Cooper, and Schrieffer [6] proposed a variational ansatz of the ground state which is a coherent state of paired electrons formed from states $|\mathbf{k},\uparrow\rangle$ and $|-\mathbf{k},\downarrow\rangle$:

$$|\psi_{\rm BCS}\rangle = \prod_{\mathbf{k}} \left(u_{\mathbf{k}} + v_{\mathbf{k}} c^{\dagger}_{\mathbf{k}\uparrow} c^{\dagger}_{-\mathbf{k},\downarrow}\right)|0\rangle \tag{1.10}$$

where $u_{\mathbf{k}}$ and $v_{\mathbf{k}}$ are the variational parameters chosen to minimise the energy that corresponds to the system Hamiltonian and $|0\rangle$ the vacuum state. Normalisation condition requires that $|u_{\mathbf{k}}|^2 + |v_{\mathbf{k}}|^2 = 1$ for all $\mathbf{k}$. Note that the above BCS ground state is a coherent state, i.e. it does not conserve particle (Cooper pair) numbers but possesses a definite phase ϕ. As a result, the BCS wavefunction actually satisfies the ODLRO condition.

Following Cooper, the BCS Hamiltonian can be written as

$$\mathcal{H}_{BCS} = \sum_{\mathbf{k},\sigma} \xi_{\mathbf{k},\sigma} c^{\dagger}_{\mathbf{k},\sigma} c_{\mathbf{k},\sigma} + \sum_{\mathbf{k},\mathbf{k}'} V_{\mathbf{k},\mathbf{k}'} c^{\dagger}_{\mathbf{k},\uparrow} c^{\dagger}_{-\mathbf{k},\downarrow} c_{-\mathbf{k}',\downarrow} c_{\mathbf{k}',\uparrow} \tag{1.11}$$

where the bare electron energy is relative to the Fermi energy $\xi_{\mathbf{k},\sigma} = \varepsilon_{\mathbf{k},\sigma} - E_F$ and the interaction $V_{\mathbf{k},\mathbf{k}'} = \left\langle -\mathbf{k},\uparrow;\mathbf{k},\downarrow|\widehat{V}|-\mathbf{k}',\downarrow;\mathbf{k}',\uparrow\right\rangle$ is attractive. This Hamiltonian describes the exact scattering process shown in Fig. 1.1 (b). Several important assumptions have been made here:

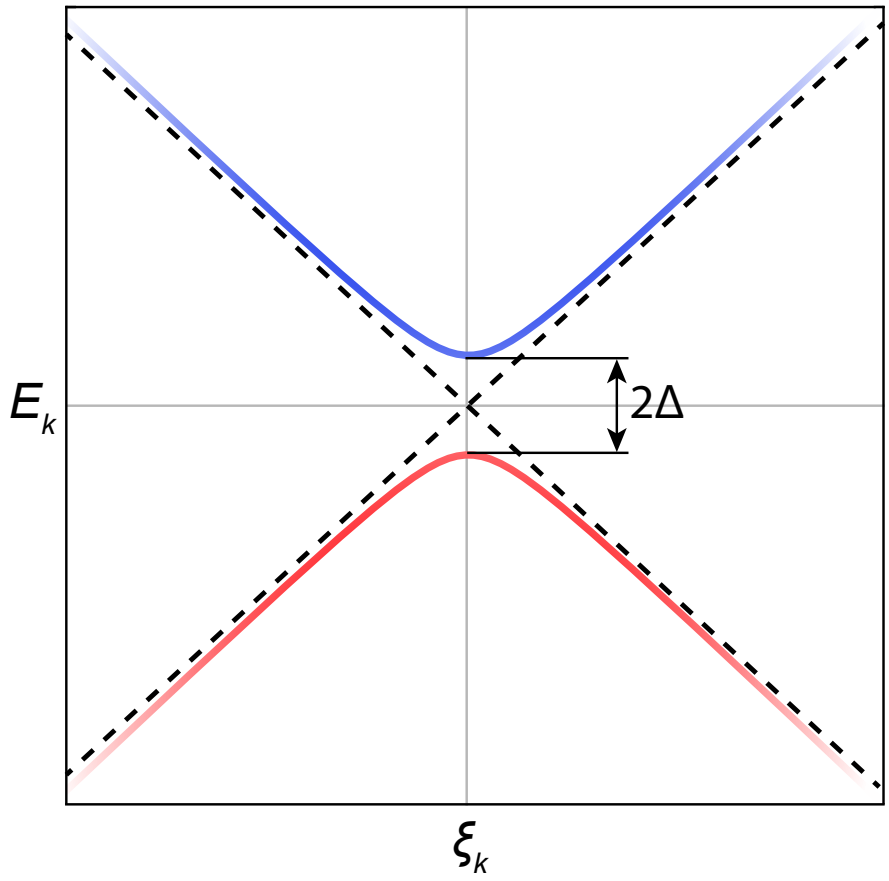

Figure 1.2: Bogoliubov quasiparticle dispersion relation $E_{\mathrm{k}} = \sqrt{\xi_{\mathrm{k}}^2 + |\Delta_{\mathrm{k}}|^2}$ as a function of ξ_{k}. In the superconducting state, a gap 2Δ opened near the Fermi wavevector $\mathbf{k}_{\mathrm{F}}$. In the normal state, Δ vanishes, and the free-quasiparticle dispersion is recovered (dashed lines).

1. The scattering process starts with electron states with opposite momenta and opposite spins, i.e. $|\mathbf{k}, \uparrow\rangle$ and $|-\mathbf{k}, \downarrow\rangle$.

2. The scattered and paired electrons are very close to the Fermi surface, i.e. $|\xi_{\mathbf{k},\sigma}| \leq \hbar\omega_D$.

3. $V_{\mathbf{k}\mathbf{k}'} = \begin{cases} -V_0 & \text{for } |\xi_{\mathbf{k}}| < \hbar\omega_D \text{ and } |\xi_{\mathbf{k}'}| < \hbar\omega_D \\ 0 & \text{otherwise} \end{cases}$ where V_0 is constant.

Upon applying the mean-field approximation, where the fluctuations of the pair field are omitted[4], the BCS Hamiltonian Eqn. 1.11 reduces to

$$\mathcal{H}_{\mathrm{BCS}} = \sum_{\mathbf{k}\sigma} \xi_{\mathbf{k}} c^{\dagger}_{\mathbf{k}\sigma} c_{\mathbf{k}\sigma} - \sum_{\mathbf{k}} \Delta^{*}_{\mathbf{k}} c_{-\mathbf{k},\downarrow} c_{\mathbf{k}\uparrow} - \sum_{\mathbf{k}} \Delta_{\mathbf{k}} c^{\dagger}_{\mathbf{k}\uparrow} c^{\dagger}_{-\mathbf{k},\downarrow} + \text{ const.} \tag{1.12}$$

[4]Operators A and B satisfy the relation: $(A - \langle A \rangle)(B - \langle B \rangle) = 0$ where $A = c^{\dagger}_{\mathbf{k}\uparrow} c^{\dagger}_{-\mathbf{k},\downarrow}, B = c_{-\mathbf{k}',\downarrow} c_{\mathbf{k}'\uparrow}$.

where

$$\Delta_{\mathbf{k}} = -\sum_{\mathbf{k}'} V_{\mathbf{k}\mathbf{k}'} \left\langle c_{-\mathbf{k}',\downarrow} c_{\mathbf{k}'\uparrow} \right\rangle . \tag{1.13}$$

To diagonalise the BCS Hamiltonian in Eqn. 1.12, we apply the Bogoliubov transformation

$$\begin{pmatrix} \gamma_{\mathbf{k}\uparrow} \\ \gamma^{\dagger}_{-\mathbf{k},\downarrow} \end{pmatrix} = \begin{pmatrix} u^{*}_{\mathbf{k}} & -v_{\mathbf{k}} \\ v^{*}_{\mathbf{k}} & u_{\mathbf{k}} \end{pmatrix} \begin{pmatrix} c_{\mathbf{k}\uparrow} \\ c^{\dagger}_{-\mathbf{k},\downarrow} \end{pmatrix} \tag{1.14}$$

where new fermionic operators $\gamma^{\dagger}_{-\mathbf{k},\downarrow}$, $\gamma_{\mathbf{k}\uparrow}$ are introduced as the superposition of particle and hole operators. The particles they create or annihilate are called the Bogoliubov quasiparticles. The BCS Hamiltonian can now be written in a diagonal form

$$\mathcal{H}_{\mathrm{BCS}} = \sum_{\mathbf{k}\sigma} E_{\mathbf{k}} \gamma^{\dagger}_{\mathbf{k}\sigma} \gamma_{\mathbf{k}\sigma} + \mathrm{const.} \tag{1.15}$$

with the dispersion relation $E_{\mathbf{k}} = \sqrt{\xi^2_{\mathbf{k}} + |\Delta_{\mathbf{k}}|^2}$. The parameters $u_{\mathbf{k}}$ and $v_{\mathbf{k}}$ now satisfy

$$|u_{\mathbf{k}}|^2 = 1 - |v_{\mathbf{k}}|^2 = \frac{1}{2}\left(1 + \frac{\xi_{\mathbf{k}}}{|E_{\mathbf{k}}|}\right). \tag{1.16}$$

According to the dispersion relation in Fig. 1.2, it is clear that there exists a gap of magnitude $|\Delta_{k_F}|$ near the Fermi surface within which there is no quasiparticle excitation at all. This indicates that, within the gap and at $T = 0$, the system is in a Cooper pair condensate - the ground state. $|\Delta_{k_F}|$ is called the *superconducting gap*. Eqn. 1.13, shows that the gap $\Delta_{\mathbf{k}}$ is related to the superconducting order parameter $\langle c_{\mathbf{k}\uparrow} c_{-\mathbf{k}\downarrow} \rangle$ defined in the last section.

Next, inserting the Bogoliubov transformation (Eqn. 1.14) into the definition of the gap Eqn. 1.13 to obtain the temperature dependence of the gap magnitude. Note that at a critical temperature T_c, the gap varnishes. Therefore, the superconducting gap can be seen as the order parameter of superconductivity in Ginzburg–Landau theory. Moreover, the ratio of $T = 0$ gap magnitude to $k_B T_c$ is a universal constant:

$$\frac{\Delta(T=0)}{k_B T_c} = 1.76. \tag{1.17}$$

Recognising the total number of states are fixed for both superconducting and normal state quasiparticles, i.e. $N_S(E)dE = N_N(\xi)d\xi \approx N(E_F)\,d\xi$, we can

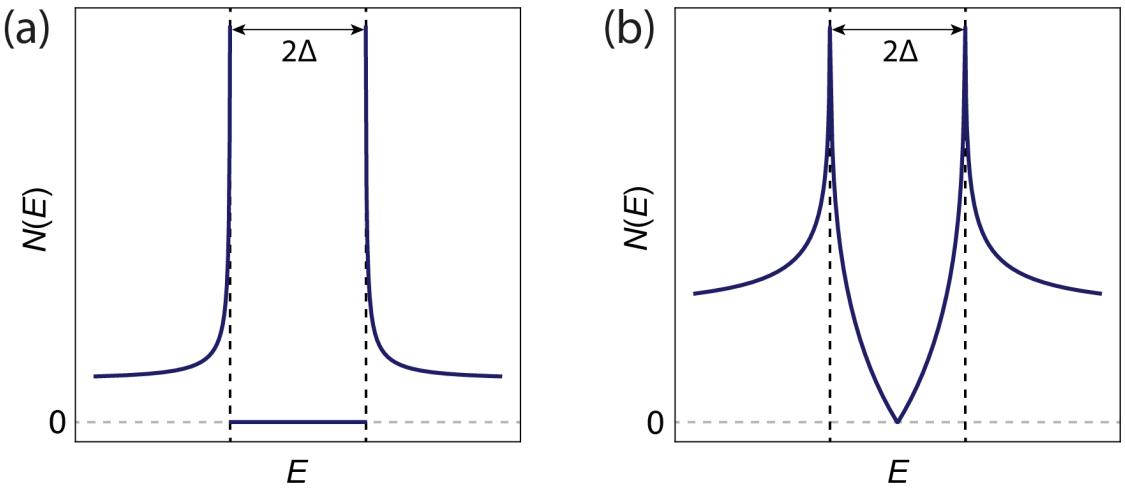

Figure 1.3: Simulated quasiparticle density of states $N(E)$ of the $s-$wave (a) and $d-$wave (b) superconductors at $T = 0$. Because of $d-$wave symmetry of the gap function, the gap is not fully opened in (b) but has a node at the Fermi energy.

directly have the density of states spectrum in the superconducting state from the superconducting dispersion relation:

$$N_S(E) = N(E_F) \frac{E}{\sqrt{E^2 - \Delta^2}} \quad E > \Delta \tag{1.18}$$

where an isotropic "*s-wave*" gap has been assumed. The spectrum is shown in Fig. 1.3(a).

1.2 Copper-oxide superconductivity

1.2.1 Crystal and electronic structure

Before the discovery of Copper-oxide superconductivity in 1986 by Bednorz and Müller [8], it was widely believed that the highest T_c at ambient pressure could not exceed 40 K based on the predictions of phonon-mediated electron pairing [9]. The surprisingly high T_c observed in cuprate superconductors[5] then suggests a distinct superconducting mechanism. Now, almost half a century has lapsed, and much physics has been uncovered in the cuprates, but much is still unknown in the mechanism behind both the superconducting and the normal states.

[5]The highest T_c at ambient pressure was observed in Hg-based cuprate materials with T_c up to 133 K [10].

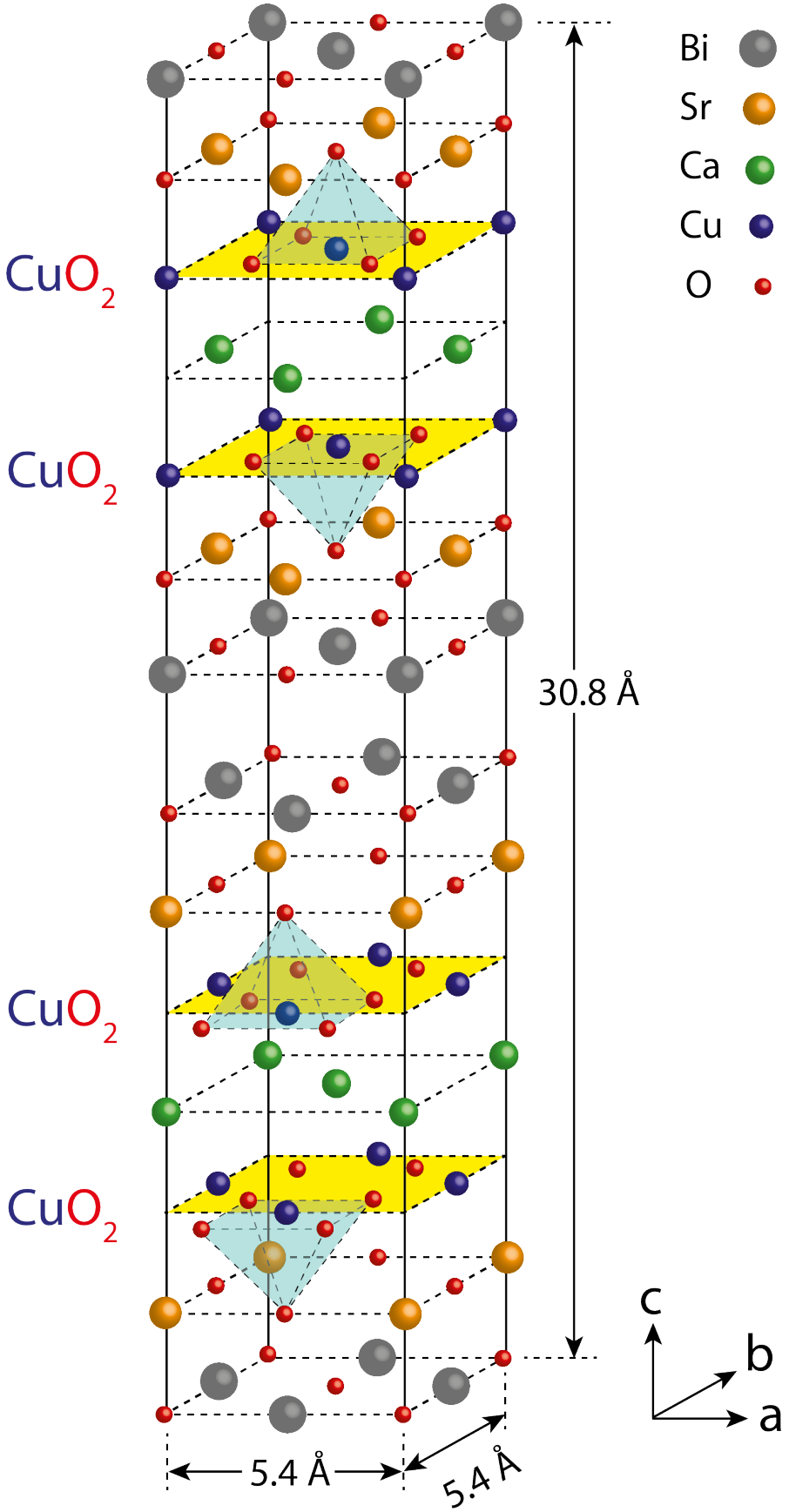

Figure 1.4: Bi-2212 unit cell with its tetragonal structure. The CuO_2 planes responsible for superconductivity are shaded with yellow, separated by the charge reservoir layers (Sr/Ca). The CuO_5 pyramids with apical Oxygen atoms are indicated with shaded areas.

A common feature of different families of cuprate superconductors is that they all share at least one layer of CuO_2 square lattice plane that is believed to be responsible for high T_c superconductivity. The CuO_2 planes are separated by layers consisting of other atoms called the charge reservoir layers. The reason is that superconductivity appears upon doping the cuprate parent compound, in which the dopants usually go to charge reservoir layers. This process provides extra holes or electrons to the CuO_2 plane. A schematic of $Bi_2Sr_2CaCu_2O_{8+x}$ crystal unit cell is shown in Fig. 1.4.

The cuprate electronic structure is shown in Fig. 1.5. In its parent compound, the Cu^{2+} ions are in the $3d^9$ state where one electron is in its valence shell. The intervening O^{2-} ions are in the $2p^6$ state where the valence shell is filled. Because of the Jahn–Teller effect, the five degenerate Cu d orbitals are split, and the $3d_{x^2-y^2}$ orbital occupies the highest energy state and contains one valence electron. The Cu^{2+} ion is in $S = 1/2$ spin state. The lobes of the O $2p_\sigma$ and the Cu $3d_{x^2-y^2}$ orbitals then have the largest overlap, causing strong hybridisation between the O and Cu bands. According to band theory, the cuprate parent compound should have been a conductor since its valence band is half-filled, but in reality, it is an antiferromagnetic insulator. The failing of band theory here is due to the strong electron-electron correlation caused by the Coulomb interaction. As an electron at one Cu site hops to another Cu site, the strong Coulomb repulsive energy U ($\sim$ 3 eV) resists any double occupancy, thus resulting in localised single Cu electrons. Unlike a Mott insulator where the O band energy level is below that of all the Cu bands, the O band here is placed between the upper and lower Hubbard bands split by U where an electron at the O band has to overcome an energy gap (the charge-transfer gap) to reach the Upper Hubbard band. The cuprate parent compound is called the *charge-transfer insulator*.

1.2.2 Phase diagram

Antiferromagnetism

The region in the leftmost (purple) of the cuprate phase diagram in Fig. 1.6 is the antiferromagnetic (AF) state. The undoped cuprate compound is called the

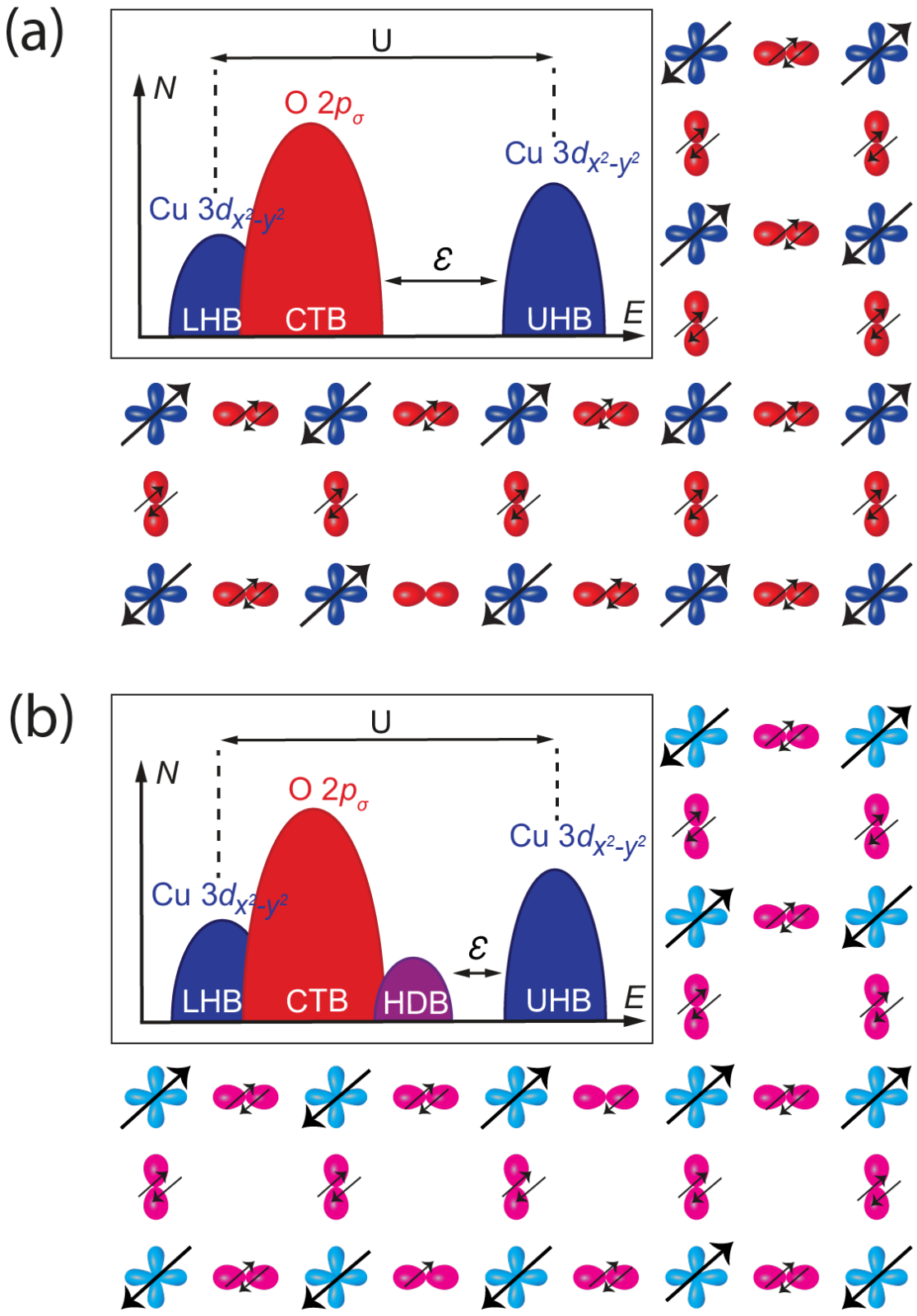

Figure 1.5: (a) Schematic of the antiferromagnetic charge-transfer insulator state in an undoped CuO_2. Inset: schematic of the density of states N vs energy E in this state. LHB, lower Hubbard band. UHB, upper Hubbard band. CTB, charge-transfer band. (b) Schematic of hole-doped CuO_2. Long-range antiferromagnetic order is destroyed. HDB, hole-doped band.

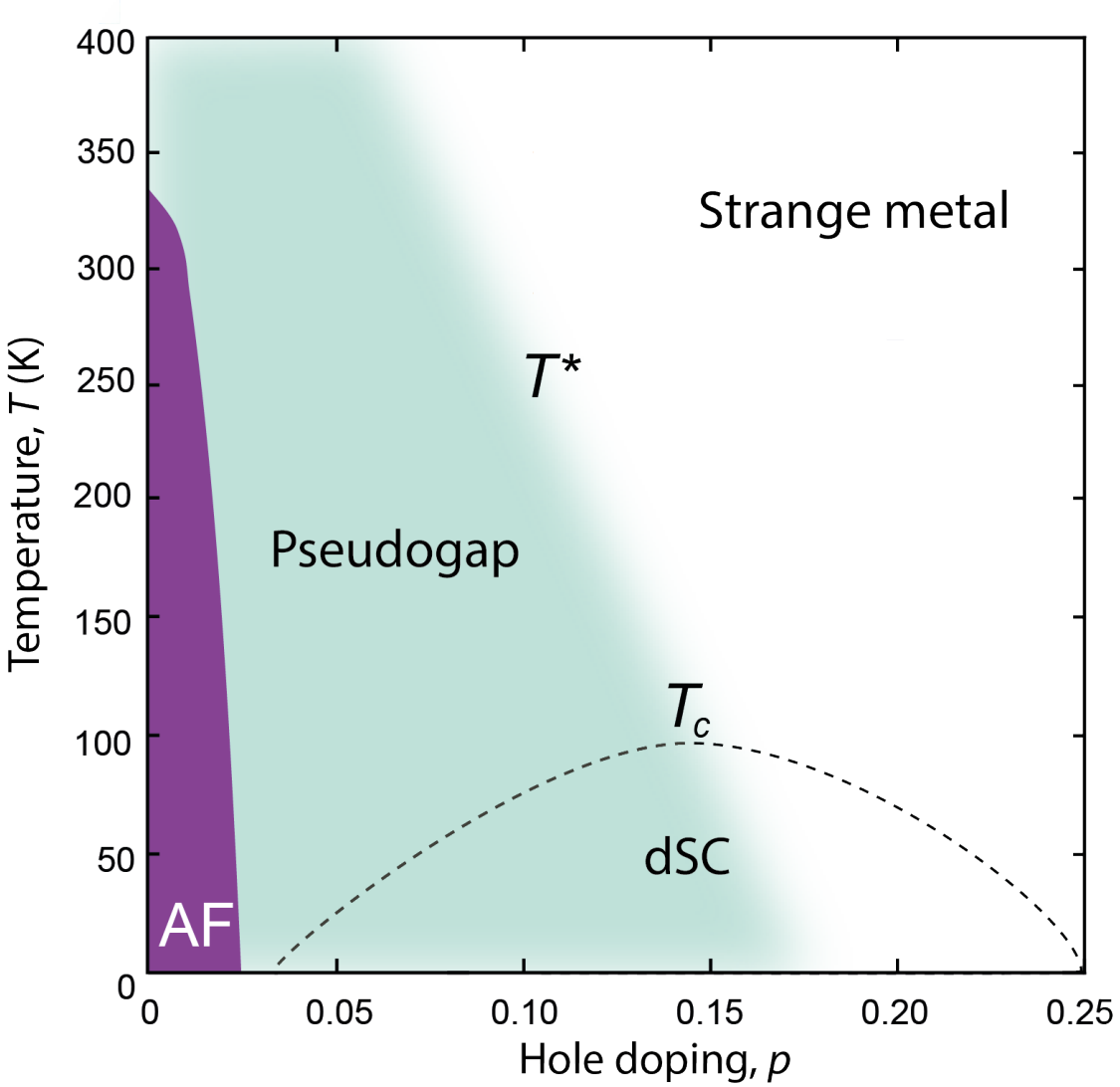

Figure 1.6: Phase diagram for hole-doped cuprate superconductors. AF, antiferromagnetism. dSC, *d*-wave superconductivity.

parent compound. Strong Coulomb interaction renders this state an insulating state, and effective spin-spin exchange interaction between electrons on the Cu orbitals gives antiferromagnetism. This antiferromagnetism is a result of the *superexchange* interaction between spin-1/2 Cu orbitals mediated by the intervening O orbitals, which can be described by the Heisenberg model

$$\mathcal{H} = J \sum_{\langle i,j \rangle} \mathbf{S}_i \cdot \mathbf{S}_j \tag{1.19}$$

where $\mathbf{S}_i$ is the Cu-site spin operator, i, j sum over the Cu sites and J is the exchange coupling constant. In the high-energy limit where $U \to \infty$, J is found to be positive and thus favours antiferromagnetism. Detailed discussion is presented in Chapter 5.

d-wave superconductivity

The insulating antiferromagnetism gradually disappears after doping holes or electrons into the cuprate parent compound, and superconductivity sets in. Superconductivity survives a much wider range on the hole-doped side than on the electron-doped side. This thesis will mainly focus on the hole-doped side. In the hole-doped side, superconductivity appears around 5% doping. T_c then scales up with increasing doping level until it reaches the maximum value at around 19% doping before going down. The doping level at which T_c maximum occurs is called optimal doped, below which is called underdoped and above which is called overdoped. An interesting phenomenon occurs at around 1/8 doping where T_c is suppressed, resulting in a dip in the superconducting dome of the phase diagram. This is now considered to result from the observed stripe order and contains the rich physics of intertwined order [11].

The cuprate superconductivity has *d-wave* symmetry. To understand this concept, let us start with two pairing electrons that are in states $|\mathbf{k}_1 s_1\rangle$ and $|\mathbf{k}_2 s_2\rangle$ respectively. Assuming zero centre-of-mass momentum, the electron pair wavefunction can be decoupled into the product of the spin part χ and the spatial part ψ:

$$\Psi\left(\sigma_1, \mathbf{r}_1; \sigma_2, \mathbf{r}_2\right) = \chi\left(\sigma_1, \sigma_2\right) \psi(\mathbf{r}) \tag{1.20}$$

where $\mathbf{r} = \mathbf{r}_1 - \mathbf{r}_2$ is the relative coordinate between the two electrons. ψ can also be called the gap function since it is related to the superconducting gap via Eqn. 1.13. Because electrons are fermions, Ψ must be antisymmetric under the exchange of the two-electron coordinates, i.e. $\Psi(-\mathbf{r}) = -\Psi(\mathbf{r})$. This results in two cases. The first is that the spin wavefunction is antisymmetric, and the gap function is symmetric or has even parity. For example, two electrons have opposite

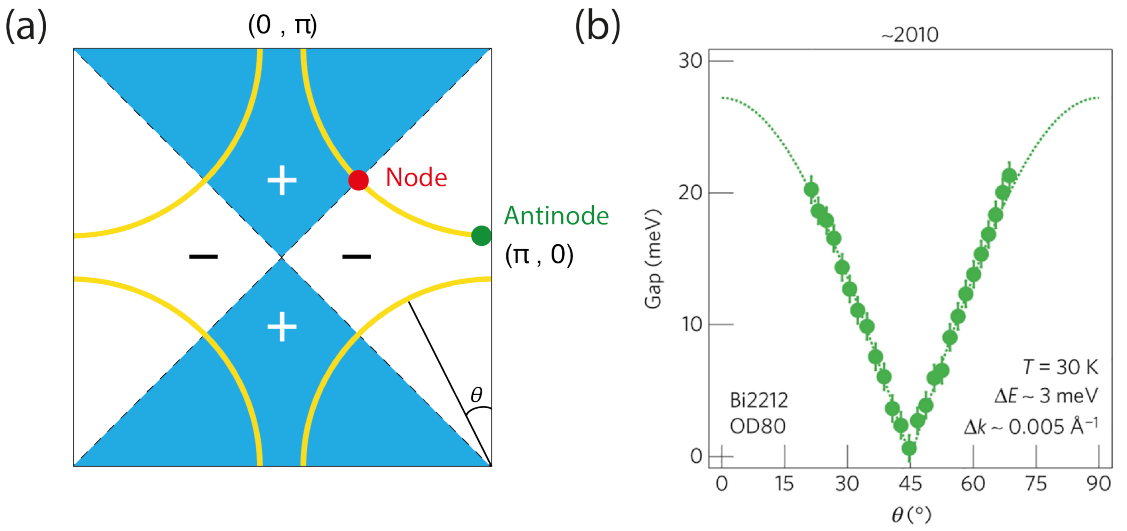

Figure 1.7: (a) Fermi surface of the CuO_2 plane. Nodal (red) and antinodal (green) regions are indicated. (b) Near-nodal gaps measured by ARPES in the cuprate superconducting state reveal the $d-$wave symmetry. The gap is minimum at the nodes and maximum at the antinodes. Photo reproduced from Hashimoto et al. [13].

spins, forming a spin singlet ($S = 0$). The second is that the two pairing electrons have the same spins ($S = 1$) and are thus symmetric, but the gap function is antisymmetric or has odd parity. In cuprate superconductors, the electron pairs form spin singlets as suggested by the Knight shift suppression at low temperatures observed in the nuclear magnetic resonance (NMR) measurements [12]. We can then describe the cuprates as being spin singlet, even parity.

If the system has rotational symmetry, $\psi(\mathbf{r})$ is then an eigenfunction of the orbital angular momentum $\mathbf{L}$ that satisfies the condition:

$$\mathbf{L}^2\psi(\mathbf{r}) = l(l+1)\hbar^2\psi(\mathbf{r}) \tag{1.21}$$

where l is an integer. The angular quantum number l here determines the symmetry of ψ. If l is even (odd), ψ is symmetric (antisymmetric). This is analogous to the electron-proton bound state in the Hydrogen atom except that here, it is the electron pairs that carry the angular quantum number l in a superconductor. Using the same convention, $l = 0, 1, 2, 3$ corresponds to *s-wave, p-wave, d-wave, f-wave* respectively. Unlike conventional BCS superconductors whose gap function is *s-wave* and isotropic, cuprate superconductors have *d-wave* gap symmetry and exhibit gapless nodes. It

is reported by angle-resolved photoemission spectroscopy (ARPES) that $d_{x^2-y^2}$ is the dominant symmetry of the gap function [14]. Since the gap is suppressed in the nodal regions, quasiparticles can be excited without energy cost. This is shown in the scanning tunnelling spectroscopy spectrum, where the gap is not completely open but has a V shape. The gap function does not have the C_4 rotational symmetry of the CuO_2 lattice plane, but rather changes sign after 90° rotation.

Besides the distinct d-wave pairing symmetry, the unconventional nature of the cuprate superconductivity can be seen from the relationships between the three quantities that characterise superconductivity, namely, the superconducting energy gap Δ, superfluid density n_s and the critical temperature T_c. The superconducting energy gap is the energy needed to break Cooper pairs. In BCS theory, the gap is related to T_c via Eqn. 1.17. Above T_c, Cooper pairs are destroyed, and superconductivity vanishes. But in the cuprates, the superconducting gap and T_c are not simply related; for example, superconductivity could also depend on the long-range phase coherence of the pair condensate's wavefunction.

In Ginzburg-Landau theory, the superfluid density is defined as $n_s \equiv |\psi|^2$, which measures the fraction of electron pairs that carry current without dissipation (supercurrent). The superfluid density is a measure of phase fluctuation of the superconducting order parameter. This can be seen from Eqn. 1.1 where the phase gradient term reads [15]

$$f = \frac{\hbar^2}{2m^*} n_s |(\nabla\theta)|^2 \tag{1.22}$$

where m^* is the effective mass. This is the energy needed for phase fluctuations to take place. The pre-factor n_s thus determines the rigidity of the superconducting phase or the "phase stiffness". One can then define a temperature scale $T_\theta \approx n_s/m^*$ above which fluctuations destroy long-range phase coherence. If $k_B T_\theta \gg \Delta$, the system becomes phase coherent instantly after $T < T_c$. It is the pair-breaking energy Δ here that determines T_c as in BCS-type superconductors. On the other hand, if $k_B T_\theta \leq \Delta$, phase coherence is more the thing that determines T_c than Δ as in materials that have very small n_s [16]. Indeed, it was discovered by muon

spin relaxation measurements that T_c is proportional to n_s in underdoped cuprates (the "Uemura plot") [17], which suggests the critical role of phase fluctuations in determining superconductivity.

To uncover the electron pairing mechanism in cuprates, it is therefore necessary to search for the element that controls the pairing amplitude $|\langle c_{\mathbf{k}\uparrow} c_{-\mathbf{k}\downarrow}\rangle|$, which is related to the Cooper pair binding energy via Eqn. 1.13. Therefore, it is not conclusive to use T_c as a proxy to $|\langle c_{\mathbf{k}\uparrow} c_{-\mathbf{k}\downarrow}\rangle|$ as it can also be influenced by the superfluid phase stiffness.

Pseudogap

At temperatures below T^* in the cuprate phase diagram (Fig. 1.6), there exists an enigmatic unidentified region called the Pseudogap (PG) that cannot be simply associated with any broken symmetry. This region is characterised by the suppression of the quasiparticle excitation spectrum near the Fermi energy even though it is in the normal state. This phenomenon is clearly shown in ARPES measurements where a gap exists at $T^* > T > T_c$ in the antinodal region. More strangely, near the nodal region, ARPES detects an ungapped 'Fermi arc' that suggests an unclosed Fermi surface. Scanning tunnelling spectroscopy (STS) also reveals much information about the pseudogap. Differential conductance measurements across T_c directly show an energy gap that appears continuously from the superconducting dome to above T_c. The PG state is also believed not to be associated with a single broken symmetry but with many broken symmetries, such as broken translational symmetry [18]. As to which ordered state simultaneously satisfies all the observed broken symmetries, it is still under debate. A possible candidate is the pair density wave (PDW) state [19].

Strange metal

Another mysterious region in the hole-doped cuprate phase diagram is the strange metal regime in the normal state. Unlike simple metals, in this region, the electrical resistivity is measured to be linear with temperature from T_c up to more than 700 K [20] and below T_c when strong magnetic fields suppress superconductivity. These transport phenomena suggest that conventional Fermi liquid theory cannot

simply describe the strange metal regime and indicate the lack of quasiparticles [18]. Together with the PG regime, they represent the forefront of contemporary cuprate research and remain one of the unsolved problems in modern physics.

1.2.3 Theoretical proposals

Hubbard model

The single-band Hubbard model is one of the simplest models that captures the strong correlations in the high-T_c CuO_2 plane. Its Hamiltonian is written as

$$\mathcal{H} = -t \sum_{\langle ij \rangle} \left(c_i^\dagger c_j + c_j^\dagger c_i \right) + U \sum_i c_{i\uparrow}^\dagger c_{i\uparrow} c_{i\downarrow}^\dagger c_{i\downarrow} \tag{1.23}$$

where $c^\dagger$ (c) is the electron creation (annihilation) operator, t is the hopping amplitude and U denotes the on-site Coulomb repulsion. In the cuprates, $U > t$ due to strong correlations. In the limit of $U \gg t$, the hopping amplitude t can be seen as a perturbation, and the Hamiltonian can be simplified by projecting out all the doubly occupied states. Virtual hopping between two singly occupied electrons induces an antiferromagnetic exchange interaction with coupling constant $J = 4t^2/U$. The Hubbard model can then be reduced to the $t - J$ model

$$\mathcal{H} = -t \sum_{\langle ij \rangle} \left(c_i^\dagger c_j + c_j^\dagger c_i \right) + J \sum_{\langle ij \rangle} \mathbf{S}_i \cdot \mathbf{S}_j \tag{1.24}$$

where $\mathbf{S}$ is the spin operator.

RVB state

One of the most influential theories for high-T_c cuprates based on the one-band Hubbard model is the resonating valence bond theory proposed by Anderson [21] in 1987. In this theory, two electrons form a singlet pair due to the superexchange J. A ground state is then formed by a superposition of all possible singlet pairs, making it a singlet spin liquid. In a 1D chain, an antiferromagnetic Néel state has site energy $-J/4$ but a RVB spin singlet ($S = 0$) has site energy $-3/8J$, which is energetically more favourable. However, this is not the case in higher dimensions where the Néel state has lower energy and is thus favoured. Anderson argued that

a resonating singlet liquid further lowers the energy and competes with the Néel state in 2D, which could be the ground state [22].

According to the theory, the singlet pairs are localised in the undoped state due to large Coulomb repulsion U. The singlet pairs are now mobile and charged upon doping and can condense into a superconducting ground state. Although the undoped cuprate is in the antiferromagnetic state rather than the RVB state, the idea could be correct in the doped superconducting case [23].

To implement the RVB concept, Anderson proposed a variational ground state as the RVB state for the $t-J$ model based on the projected BCS ground state wavefunction [22]:

$$|\Psi_{\mathrm{RVB}}\rangle = P_N P_G |\mathrm{BCS}\rangle \tag{1.25}$$

where $|\mathrm{BCS}\rangle$ is given in Eqn. 1.10, P_G is the Gutzwiller projection operator that projects out all the doubly occupied states, and P_N is the operator that fixes the particle number to N. Physical observables can then be calculated based on this variational ground state. .

Three-band model

Around the same time Anderson proposed the RVB theory, Emery proposed a model that includes the additional Oxygen sites [24] and thus "three-band". The single-band Hubbard model seems inadequate since the doped holes primarily go into the Oxygen sites. In this model, the Oxygen sites play an essential role as they host the holes that pair up to form supercurrent. Details of the three-band model are discussed in section 5.2.1.

Zhang-Rice singlet

It was shown by Zhang and Rice [25] that the three-band model could be reduced to an effective one-band model by hybridising the holes in the four O $2p$ orbitals with the central Cu $3d_{x^2-y^2}$ orbital. This leads to a singlet formation that eliminates the spin-1/2 of the Cu site. This singlet can then hop to other Cu sites that is responsible for hole-doped superconducting Cu oxides.

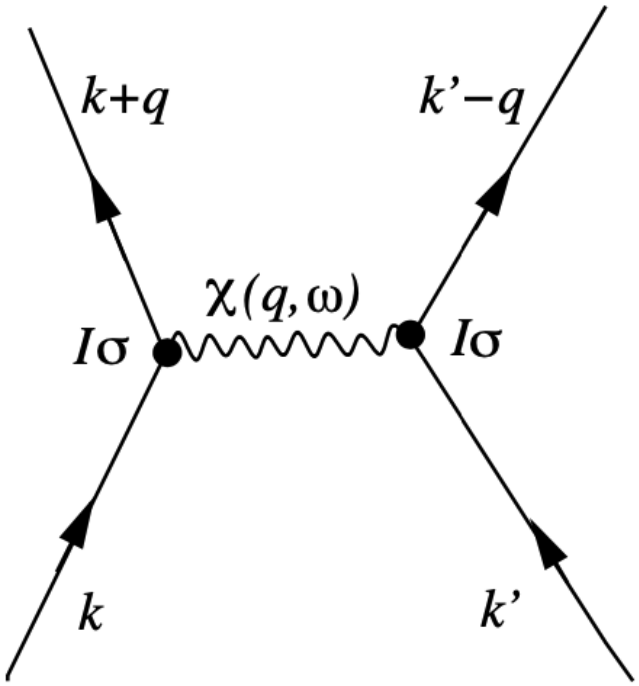

Figure 1.8: Schematic of spin fluctuation induced electron pairing by exchanging a magnon. Photo reproduced from [26].

Spin fluctuations

Starting from the undoped insulating phase, a pairing mechanism based on antiferromagnetic spin fluctuations is proposed. The effective Hamiltonian can be written as [26]:

$$H = \sum_{\mathbf{k},s} \xi_{\mathbf{k}} c^{\dagger}_{\mathbf{k}s} c_{\mathbf{k}s} - \frac{1}{2N^2} \sum_{\mathbf{k},\mathbf{k'},\mathbf{q}} \sum_{s_1,s_2,s_3,s_4} v(\mathbf{q}) \vec{\sigma}_{s_1 s_2} \cdot \vec{\sigma}_{s_3 s_4} c^{\dagger}_{\mathbf{k}+\mathbf{q},s_1} c_{\mathbf{k}s_2} c^{\dagger}_{\mathbf{k'}-\mathbf{q},s_3} c_{\mathbf{k'},s_4} \quad (1.26)$$

where $\chi(\mathbf{q})$ and $\chi_0(\mathbf{q})$ are the static spin susceptibility and the free electron spin susceptibility respectively. The pairing interaction has the form

$$v(\mathbf{q}) = U + U^2 \chi(\mathbf{q}) \quad \text{with} \quad \chi(\mathbf{q}) = \frac{\chi_0(\mathbf{q})}{1 - U\chi_0(\mathbf{q})} \quad (1.27)$$

where U is the Coulomb repulsion. Here, $\chi(\mathbf{q})$ describes the antiferromagnetic spin fluctuations if its maximum value occurs at $\mathbf{Q} = (\pi/a, \pi/a)$. The electron pairing mechanism can then be understood as two electrons scattered by exchanging a magnon, as shown in Fig. 1.8.

One never notices what has been done; one can only see what remains to be done.

— Marie Curie

2

Techniques of scanning tunnelling microscopy

Contents

In this chapter, I will introduce two powerful techniques that are based on STM: spectroscopic imaging scanning tunnelling microscopy (SI-STM) and scanned Josephson tunnelling microscopy (SJTM). Together, they laid the foundation for the scientific discoveries presented later in this thesis.

In 1982, G. Binnig and H. Rohrer pioneered a groundbreaking tool: the scanning tunnelling microscope (STM). Their seminal work transformed the landscape of microscopy and earned them the Nobel Prize in Physics in 1986 [27]. Distinct from other microscopes, STM employs the quantum tunnelling effect to capture

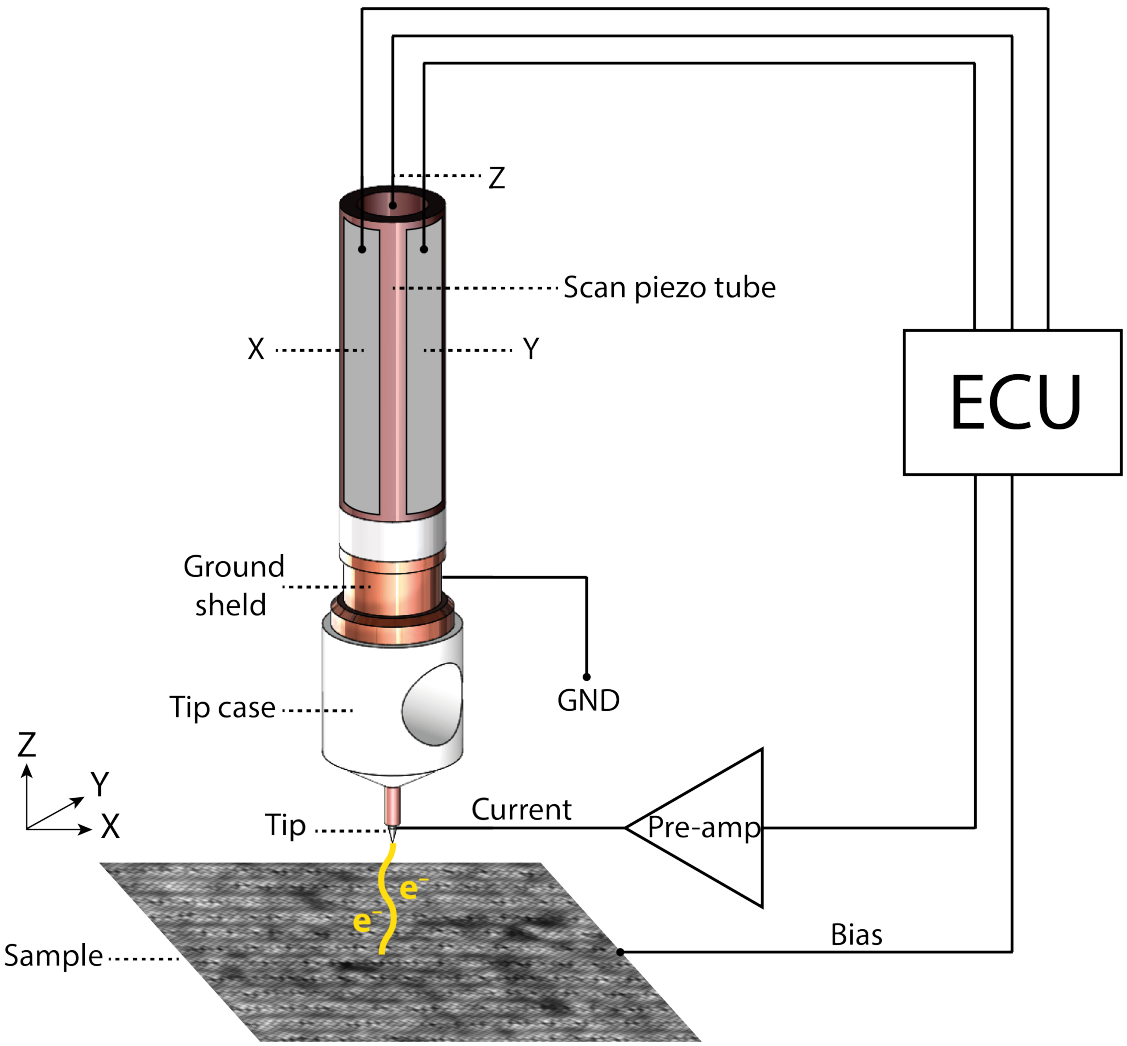

Figure 2.1: Schematic of the working princeple of STM. The tip is controlled by a piezoelectric tube that moves in the X, Y and Z directions to produce scanning motions. ECU, electronic control unit.

images through a scanning approach.

2.1 SI-STM: visualising quantum states via single-particle tunnelling

2.1.1 Quantum tunnelling theory

The quantum tunnelling effect happens when two conductors are brought close together and separated by a layer of insulating material, forming a conductor-insulator-conductor junction. Because the electron wavefunctions of the conductors overlap in the insulating region, electrons are allowed to travel through the classically

forbidden potential barrier, i.e. the insulating region, from one conducting side to the other. When a bias voltage is applied to the junction, a tunnelling current flows. In this section, I will follow the theoretical approach given by Fischer et al. [28] to derive the tunnelling current.

The total Hamiltonian of the system can be written as

$$\mathcal{H} = \mathcal{H}_{\mathcal{L}} + \mathcal{H}_{\mathcal{R}} + \mathcal{H}_{\mathcal{T}} \equiv \mathcal{H}_0 + \mathcal{H}_{\mathcal{T}} \tag{2.1}$$

where $\mathcal{H}_{\mathcal{T}}$ is the tunnelling Hamiltonian. $\mathcal{H}_{\mathcal{L}}$ and $\mathcal{H}_{\mathcal{R}}$ are the single-electron bare Hamiltonian of the left and right conductors respectively, which have the form $-\frac{\hbar^2}{2m}\nabla^2 + V(\mathbf{r})$. The two conductors are assumed to be independent of each other so that the commutation relationship satisfies $[\mathcal{H}_{\mathcal{L}}, \mathcal{H}_{\mathcal{R}}] = 0$. In the real space representation, we have

$$\mathcal{H}_T = \int d\mathbf{l}d\mathbf{r}T(\mathbf{l},\mathbf{r})\psi^\dagger(\mathbf{r})\psi(\mathbf{l}) + \int d\boldsymbol{l}d\mathbf{r}T^*(\mathbf{l},\mathbf{r})\psi(\mathbf{r})\psi^\dagger(\mathbf{l}) \tag{2.2}$$

where $\psi^\dagger(\mathbf{r})(\psi(\mathbf{r}))$ creates (destroys) an electron at position $\mathbf{r}$ at the right conductor, $\psi^\dagger(\mathbf{l})(\psi(\mathbf{l}))$ creates (destroys) an electron at position $\mathbf{l}$ at the left conductor. $T(\mathbf{l},\mathbf{r})$ contains the tunnelling matrix element $T_{\mu\nu}$ in the single-particle states $\varphi_{\mu\nu}$ through $T(\mathbf{l},\mathbf{r}) = \sum_{\mu\nu}\varphi^*_\mu(\mathbf{l})T_{\mu\nu}\varphi_\nu(\mathbf{r})$.

Define $A = \int d\mathbf{l}d\mathbf{r}T(\mathbf{l},\mathbf{r})\psi^\dagger(\mathbf{r})\psi(\boldsymbol{l})$, so that $\mathcal{H}_{\mathcal{T}} = \mathcal{A} + \mathcal{A}^\dagger$. Ehrenfest theorem gives the time evolution of the particle number n_R

$$i\dot{n}_R = [n_R, \mathcal{H}] = [n_R, \mathcal{H}_{\mathcal{T}}] = \mathcal{A} - \mathcal{A}^\dagger \tag{2.3}$$

where we use the fact that $[\mathcal{H}_0, n_R] = 0$ and set $\hbar = 1$. The tunnelling current is then defined as the rate of change of charged particles

$$I = e\left\langle \dot{n}_R \right\rangle. \tag{2.4}$$

Treating $\mathcal{H}_{\mathcal{T}}$ as a perturbation, to the first order, we then have the linear response of the tunnelling current from the Kubo formula

$$\left\langle \dot{n}_R \right\rangle_t = -i\int_{-\infty}^{+\infty} dt'\theta\left(t-t'\right)\left\langle [\dot{n}_R(t), \mathcal{H}_{\mathcal{T}}\left(t'\right)]\right\rangle_{\mathcal{H}_0}. \tag{2.5}$$

Since the time evolution of operator $\mathcal{A}$ is also described by the bare Hamiltonian $\mathcal{H}_0$, we have

$$e^{i\mathcal{H}_0 t}\mathcal{A}e^{-i\mathcal{H}_0 t} = e^{-i(\mu_L-\mu_R)t}e^{i\mathcal{K}t}\mathcal{A}e^{-i\mathcal{K}t} \equiv e^{-ieVt}\mathcal{A}(t) \tag{2.6}$$

where μ is the chemical potential and V is the applied bias voltage and $\mathcal{K} = \mathcal{H}_0 - \mu_L n_L - \mu_R n_R$. Now $\mathcal{A}$ and $\mathcal{A}^\dagger$ evolve according to $\mathcal{K}$ and we have

$$\begin{aligned} i\dot{n}_R(t) &= e^{-ieVt}\mathcal{A}(t) - e^{ieVt}\mathcal{A}^\dagger(t), \\ \mathcal{H}_T(t') &= e^{-ieVt'}\mathcal{A}(t') + e^{ieVt'}\mathcal{A}^\dagger(t'). \end{aligned} \tag{2.7}$$

Inserting Eqn. 2.7 into Eqn. 2.5, we arrive at the expression for the tunnelling current

$$\begin{aligned} I =& 2e\,\mathrm{Im}\int_{-\infty}^{+\infty} dt' \Big\{ e^{-ieV(t-t')}(-i)\theta(t-t')\left\langle\left[\mathcal{A}(t), \mathcal{A}^\dagger(t')\right]\right\rangle \\ &+ e^{-ieV(t+t')}(-i)\theta(t-t')\left\langle[\mathcal{A}(t), \mathcal{A}(t')]\right\rangle\Big\} \equiv I_e + I_J \end{aligned} \tag{2.8}$$

where the first term is the single-particle tunnelling current I_s and the second term is the pair-tunnelling current I_J related to the Josephson effect. The first term can be written as the Fourier transform of a time-ordered correlator

$$\begin{aligned} I_e &= 2e\,\mathrm{Im}\int d\mathbf{l}_1 d\mathbf{r}_1 d\mathbf{l}_2 d\mathbf{r}_2 T(\mathbf{l}_1, \mathbf{r}_1) T^*(\mathbf{l}_2, \mathbf{r}_2) \\ &\times \mathcal{G}(\mathbf{l}_1, \mathbf{l}_2, \tau)\mathcal{G}(\mathbf{l}_1, \mathbf{l}_2, -\tau) \end{aligned} \tag{2.9}$$

in which $\mathcal{G}(\mathbf{l}_1, \mathbf{l}_2, \tau) = -\left\langle \mathcal{T}_\tau \psi(\mathbf{l}_1, \tau)\psi^\dagger(\mathbf{l}_2, 0)\right\rangle$ is the time-ordered Green's function. In the spectral representation, we have

$$\mathcal{G}(x_1, x_2, i\omega_n) = \int_{-\infty}^{+\infty} d\omega \frac{A(x_1, x_2, \omega)}{i\omega_n - \omega} \tag{2.10}$$

where $\omega_n = (2n+1)\pi/\beta$ is the odd Matsubara frequencies and A the spectral function. Substituting Eqn. 2.10 into Eqn. 2.9 and inserting back the dimensional quantity $\hbar^{-1}$, the single-particle tunnelling current has the final expression

$$I_e = \frac{2\pi e}{\hbar}\int d\omega [f(\omega - eV) - f(\omega)] \sum_{\mu\nu} |T_{\mu\nu}|^2 A_\mu(\omega - eV) A_v(\omega) \tag{2.11}$$

where f is the Fermi-Dirac distribution.

Based on Bardeen's matrix element calculation [30], Tersoff and Hamann [29] obtained the tunnelling matrix element $T_{\mu\nu}$ specifically for STM by assuming a

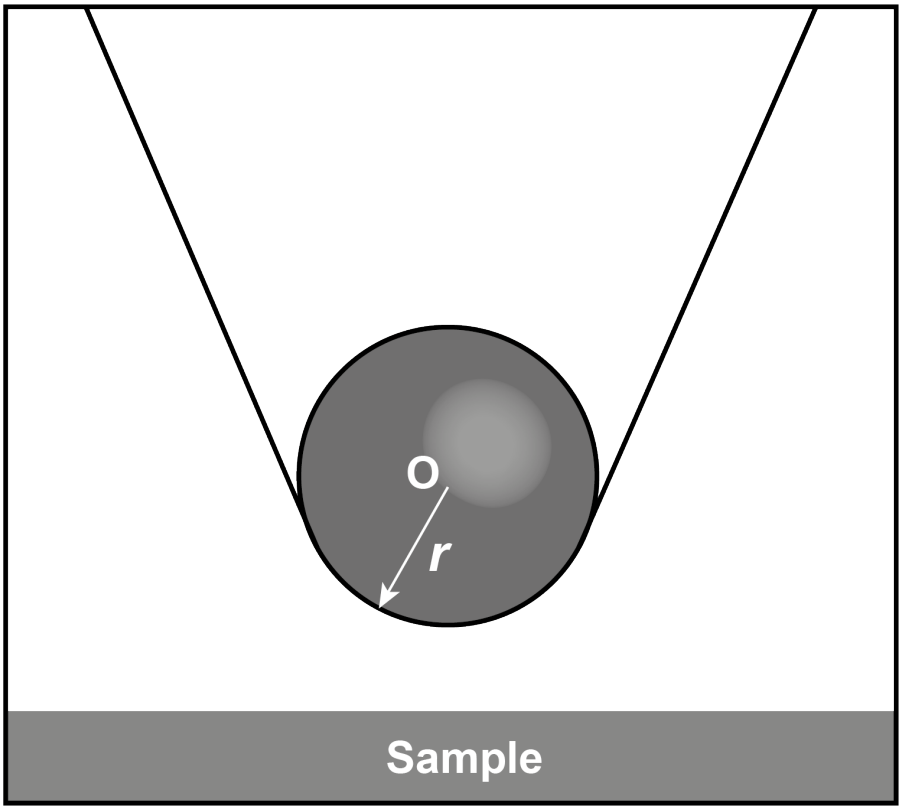

Figure 2.2: Schematic of the Tersoff-Hamann STM model. The tip apex is assumed spherical with radius $\boldsymbol{r}$ and is centred at **O**. When the tip is approached, the tip-sample distance is d. Photo adapted from Tersoff and Hamann [29].

spherical geometry at the apex of the tip. They found that $T_{\mu\nu}$ is proportional to the wavefunction of the sample at the centre of the tip apex $\varphi_\nu(\mathbf{r}_0)$,

$$T_{\mu\nu} = \frac{\hbar^2}{2m} 4\pi \Omega_t^{-1/2} R e^{\kappa R} \varphi_\nu(\mathbf{r}_0), \tag{2.12}$$

where $\kappa = \sqrt{2m\phi/\hbar^2}$ is the minimum inverse decay length for the wave functions in vacuum, ϕ the effective work function, $\boldsymbol{r}$ the curvature radius of the tip apex, Ω_t the tip volume and $\mathbf{r}_0$ the centre of the tip apex. Recognizing the relationship between the real space spectral function and the local density of states (LDOS) $N(\mathbf{r},\omega) = A(\mathbf{r},\mathbf{r},\omega)$ and inserting Eqn. 2.12 back into Eqn. 2.11 we have

$$I_e(V) \propto R^2 e^{2\kappa R} \int \frac{d\omega}{\hbar} [f(\omega - eV) - f(\omega)] g_{\text{tip}}(\omega - eV) N_{\text{sample}}(\boldsymbol{r}_0, \omega) \tag{2.13}$$

where g_{tip} is the tip density of states (DOS) per unit volume, and the real space spectral function is given by

$$\int d\mathbf{r_1} d\mathbf{r_2} \varphi_v^*(\mathbf{r_1}) A(\mathbf{r_1}, \mathbf{r_2}, \omega) \varphi_v(\mathbf{r_2}) = A(\omega). \tag{2.14}$$

Eqn. 2.13 indicates that the tunnelling current depends on two factors: 1) the density of states at a given energy and 2) the difference of the electron occupation numbers. This means that information on the density of states can be obtained by measuring the tunnelling current as a function of the voltage difference. Taking the derivative with respect to the applied bias voltage gives

$$\frac{dI_e}{dV}(V) \propto \int d\omega \left[f'(\omega - eV)\right] N_{\text{sample}}\ (\mathbf{r}_0, \omega)\,. \tag{2.15}$$

Thus, the differential conductance measured by STM gives a direct probe of the LDOS of the sample. Note that at finite temperature, the derivative of the Fermi function also leads to a thermal broadening of approximately $3.5k_BT$ since it's no longer a delta function but has a finite width. This is one of the reasons why a dilution-fridge-based mK STM is necessary as it offers energy resolution down to tens of μeV, making it possible to study many exotic phases of matter that have very low transition temperatures.

For a tip-sample distance z, we have $|\varphi_\nu(\mathbf{r}_0)|^2 \propto e^{-\kappa(R+z)}$. Assuming constant tip DOS and since the Fermi function is step-like at low temperatures, the above current expression can be simplified as

$$I_e(V) \propto \mathrm{e}^{-\kappa z} g_{\text{tip}} \int_0^{eV} d\omega N_{\text{sample}}(\omega). \tag{2.16}$$

Thus, the tunnelling current decays exponentially as the tip moves away from the sample. Typically, the work function has the value $\phi \sim 5$ eV in a simple metal. So even if the tip retracts by an angstrom from the sample, it would result in an order of magnitude drop in the tunnelling current. The differential conductance at a specific voltage then has the following compact form:

$$\frac{dI_e}{dV}(V) \propto \mathrm{e}^{-\kappa z} N_{\text{sample}}\ (\omega = eV). \tag{2.17}$$

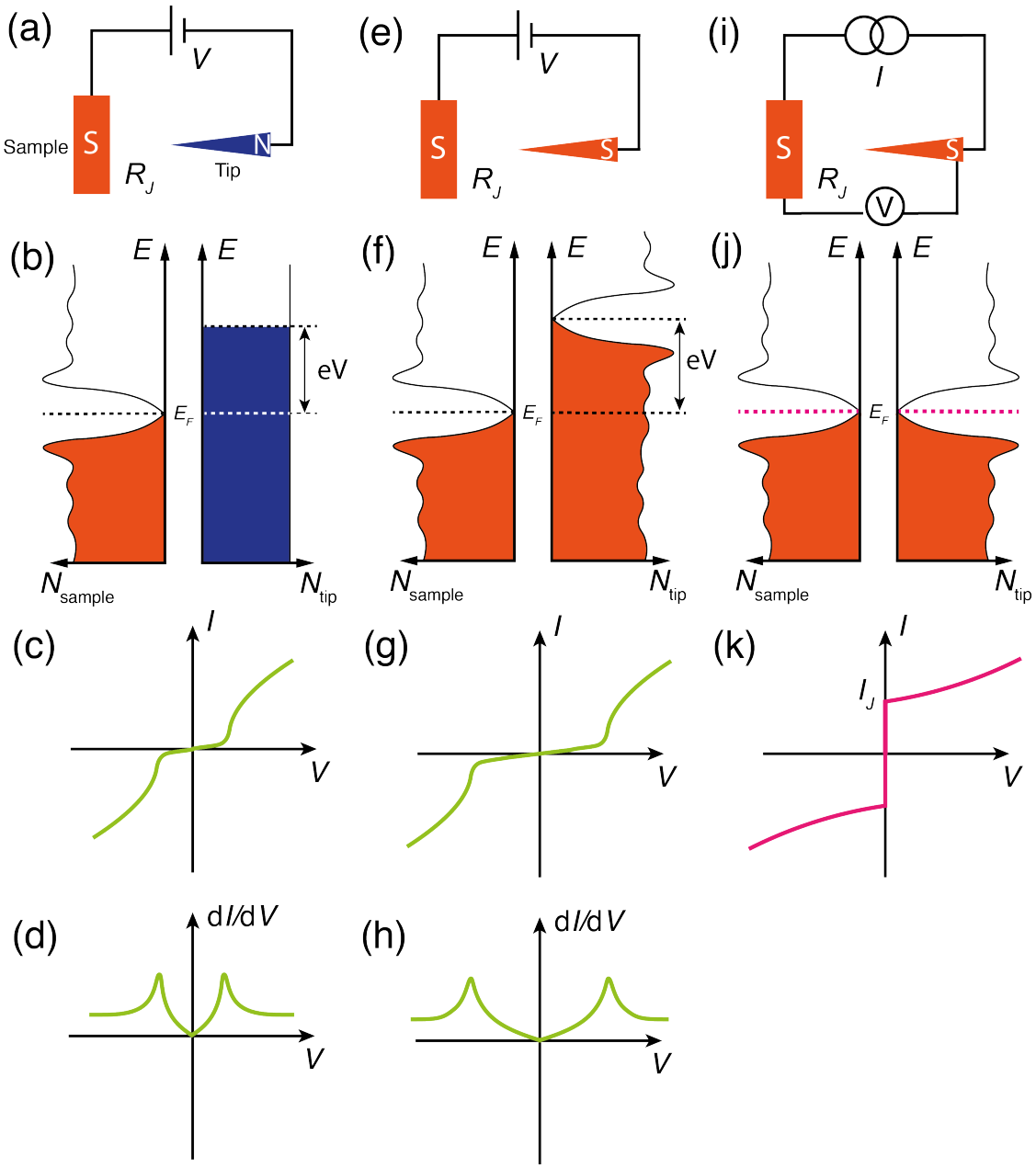

Figure 2.3: Illustration of different STM tunnelling modes. (a)-(d) Single-particle tunnelling in a normal-insulating-superconducting (N-I-S) junction. (a) Schematic of the tunnelling junction circuit diagram. (b) Schematic of the density of states (N) with sample modelled as a d-wave superconductor. (c) Measured $I-V$ characteristics. (d) Measured differential conductance $dI/dV-V$ characteristics. (e)-(h) Single particle tunnelling in superconducting-insulating-superconducting (S-I-S) junction. The measured dI/dV spectrum results from the convolution between the sample and tip density of states and thus shows a doubled energy gap. (i)-(k) Josephson (Cooper pair) tunnelling where supercurrent flows at zero bias.

2.1.2 SI-STM measurement types

The contemporary operating principles of an STM involve the use of a sharp metallic tip, which is precisely controlled by a piezoelectric tube to adjust its horizontal and vertical movements with picometer-scale accuracy. This enables the tip to scan the surface in parallel lines. By applying a bias voltage between the tip and the sample and positioning the tip mere angstroms away from the surface, the quantum tunnelling phenomenon occurs, allowing for the measurement of the tunnelling current. An electronic PID-controlled feedback loop is then implemented to maintain a constant current, as well as a constant tip-sample distance, using the preselected setup current I_s and voltage V_s.

Topography

During experiments, the distance between the tip and the sample is determined by the set-up current and voltage, I_s and V_s, which are chosen arbitrarily. Eqn. 2.16 can then be re-written as

$$\begin{aligned} I_s &= Ce^{-\frac{T(\mathbf{r})}{T_0}} \int_0^{eV_s} N_{sample}(\mathbf{r},\varepsilon)d\varepsilon \\ \Rightarrow Ce^{-\frac{T(\mathbf{r})}{T_0}} &= \frac{I_s}{\int_0^{eV_s} N_{sample}(\mathbf{r},\varepsilon)d\varepsilon} \end{aligned} \tag{2.18}$$

where T is the tip-sample distance or the topography. Extracting $T(\mathbf{r})$ gives $T(\mathbf{r},V_s) = T_0 \ln\left[\int_0^{eV_s} N_{sample}(\mathbf{r},\varepsilon)d\varepsilon\right] + C$, which is the topographic image that a typical STM measures. Notice that from the above equation, the measured quantity $T(\mathbf{r})$ not only depends on the topographic structure of the sample surface but also the logarithm of the integrated sample LDOS.

The topographic image is often measured in the constant-current mode, where the tunnelling current and, thus, the tip-sample distance are kept constant by a PID feedback loop. As the tip scans across the sample surface, if the tunnelling current exceeds its set-up value, the feedback system activates the high voltage for the Z electrode on the scan tube. This action retracts the tip, effectively reducing the current. Conversely, if the current falls below its set-up value, the feedback system compensates by extending the tip to increase the current. Thus, the Z

variation in space generated by the scan tube movement in the Z direction produces the topographic image $T(\mathbf{r})$. Inside the PID control unit, the error function $e(t)$ that measures the difference between the measured tunnelling current and the set-up current is amplified and converted to the output voltage signal $Z(t)$ via the proportional (P), integral (I) and the differential (D) gain. Usually, only P and I terms are used for topographic imaging. This is described by the equation:

$$Z(t) = P \cdot e(t) + I \int_0^t e\left(t'\right) dt' \tag{2.19}$$

where the P, I are the gain parameters set by the user. This output signal $Z(t)$ can then be calibrated to its corresponding Z variations.

Spectroscopy

Inserting Eqn. 2.18 into Eqn. 2.16 we have

$$\frac{I(\mathbf{r}, V)}{I_s} = \frac{\int_0^{eV} N_{sample}(\mathbf{r}, \varepsilon) d\varepsilon}{\int_0^{eV_s} N_{sample}(\mathbf{r}, \varepsilon) d\varepsilon} \tag{2.20}$$

where $f(\omega, T) \approx 1$. In practice, $|V| \ll |V_s|$, so the tunnelling current is directly proportional to the integrated density of states provided that $\int_0^{eV_s} N_{sample}(\mathbf{r}, \varepsilon) d\varepsilon$ is almost featureless. Taking the voltage derivative of the above equation, we obtain the essential measurement quantity of an SI-STM:

$$g(\mathbf{r}, eV) = \frac{dI}{dV}(\mathbf{r}, E = eV) = \frac{eI_s N_{sample}(\mathbf{r}, eV)}{\int_0^{eV_s} N_{sample}(\mathbf{r}, eV) d\varepsilon}, \tag{2.21}$$

which is the differential conductance. If V_s is chosen so that $T\left(\mathbf{r}, V_s\right)$ is essentially homogeneous, the measured differential conductance is then linearly proportional to the LDOS and Eqn. 2.21 gives a direct measurement of the sample electronic structure.

There are usually two ways to measure the differential conductance spectrum $\frac{dI}{dV}(V)$. The first is to measure the $I(V)$ spectrum first by sweeping the bias voltage and then take the numerical derivative with respect to V. The other is to use a lock-in amplifier to measure the AC component of the response current subject to an input AC reference signal. In general, the flicker $(1/f)$ noise easily dominates the near DC region (< 10 Hz) of the current noise power spectrum but remains

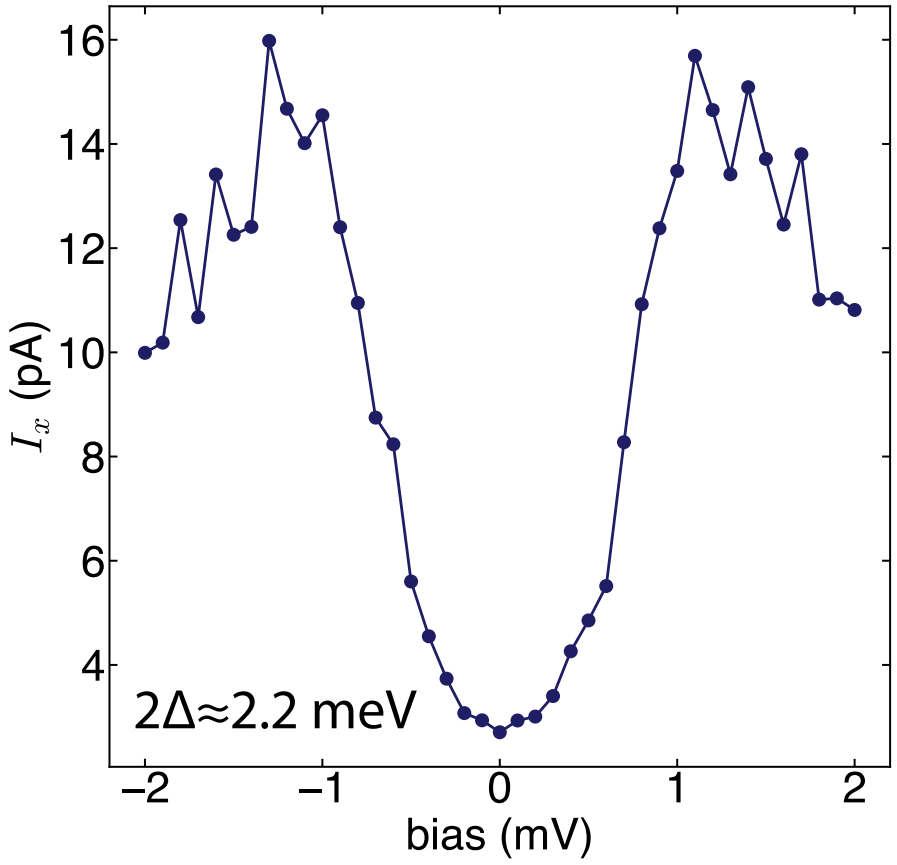

Figure 2.4: Spectrum showing the superconducting gap of $NbSe_2$ measured at 1.4 K at GEMINI. I_x: X channel of the lock-in amplifier.

relatively constant in the thermal noise region (> 10 Hz). It is thus advantageous to employ the lock-in amplifier with a reference modulation in the thermal noise region to enhance the signal-to-noise ratio (SNR) [31].

Suppose a reference voltage modulation $V_m(t) = V_m \cos(\omega t)$ is added to the DC bias voltage V_0, the response tunnelling current can then be expanded using the Taylor series:

$$I\left[V_0 + V_m(t)\right] = I\left(V_0\right) + \left.\frac{dI}{dV}\right|_{V_0} V_m \cos(\omega t + \phi) + \frac{1}{2}\left.\frac{d^2 I}{dV^2}\right|_{V_0} V_m^2 \cos^2(\omega t + \phi) + \cdots \quad (2.22)$$

where ϕ is the additional phase shift induced by the circuit such as band-pass filters. In a lock-in amplifier, a high-pass filter ($f_{\text{cutoff}} < 1$ Hz) removes the DC

component before multiplying the modulation $\cos(\omega t)$. This yields

$$\begin{aligned} I_x &= I\left[V_0 + V_m(t)\right] - I\left(V_0\right) = \underbrace{\left.\frac{dI}{dV}\right|_{V_0}}_{I_{ac}} V_m \cos(\omega t + \phi)\cos(\omega t) + \cdots \\ &= \frac{I_{ac}}{2}[\cos(\phi) - \cos(2\omega t + \phi)] + \cdots \end{aligned} \tag{2.23}$$

where I_x stands for the X channel[1] of the lock-in amplifier. Then the current signal goes through a low-pass filter (typically $\omega_{\text{cutoff}} \approx \omega/3$) which removes the AC components of the current. This gives

$$I_x = \left.\frac{dI}{dV}\right|_{V_0} V_m \cos(\phi). \tag{2.24}$$

Typically, the phase shift ϕ is calibrated so that the resistive channel of the current I_x is zero while the tip is withdrawn (off tunnelling). Thus, Eqn. 2.24 indicates that the X channel of the lock-in amplifier is a direct measure of the differential conductance at bias voltage V_0. In practice, before acquiring any I_x measurements, an additional settling time τ is added after having reached the next bias level. This time scale needs to be larger than the rise time of the lock-in low-pass filter to prevent any signal loss. Then, $I_x(t)$ is averaged over a time scale called the integration time. This gives one data point for a certain bias level before moving to the next one. This procedure is then repeated for a range of biases to generate spectrum measurements.

Spectroscopic mapping

The above point spectrum measurement naturally extends to spatial mapping. During a point spectrum measurement at a specific location, the z-piezo feedback circuit is turned off. The feedback loop is turned on when the STM begins moving to the next location and then turned off again for the next point spectrum measurement. After scanning completes, the data file is thus 3-dimensional which constitutes a 2-dimensional spatial conductance layer at each bias level. Therefore, SI-STM has the capability to access position-dependent LDOS measurements at different energy levels.

[1]Typically, a lock-in amplifier has two output channels, X and Y, which represent the signal as a vector relative to the reference signal. Here, we use the X channel to measure the tunnelling signal.

Despite the enhanced SNR using the lock-in amplifier, the extra voltage modulation $V_m(t)$ centred at bias V further reduces the energy resolution. This is because the measured $\frac{dI}{dV}$ is an average over the amplitude of $V_m(t)$. Together with the thermal broadening effect, the finial energy resolution of an SI-STM is given by [32]:

$$\Delta E \simeq \sqrt{(3.3k_BT)^2 + (2.5V_m)^2}. \tag{2.25}$$

2.2 SJTM: visualising superconducting condensate via pair tunnelling

Conventional STM measures the single-particle tunnelling current to access the topographic and spectroscopic properties of the sample. While the measured single-particle excitation gap is defined as the superconducting gap in conventional BCS superconductors, it fails to represent the true superconducting gap in strongly correlated cuprate high T_c superconductors as, for example, the gap defined as the distance between two coherence peaks in the DOS spectrum can be influenced by the issue of the pseudogap. It is therefore necessary to develop a new technique that directly probes the electron-pair (Cooper pair) condensate that is the definite signature of superconductivity. In 2016, scanned Josephson tunnelling microscopy (SJTM) [33] was developed in our group. This technique utilizes a superconducting tip to scan the superconducting sample and measure the Josephson tunnelling current that is related to the amplitude of the superconducting condensate. Since then, a variety of exotic phases and mechanisms have been discovered using this powerful technique [33–36]. In this chapter, I will present the operating principle of SJTM and then in Chapter 4, its application to discovering a new state of matter in the hole-doped cuprate superconductor $Bi_2Sr_2CaCu_2O_{8+x}$ (Bi-2212).

Brian D. Josephson predicted a fascinating quantum tunnelling effect that allows a non-dissipative supercurrent (electron-pair current) to flow between two superconductors that are separated by a thin insulating layer. The superconductor-insulator-superconductor (SIS) junction is called the Josephson junction. The

macroscopic wavefunctions for each side of the superconductor can be written as:

$$\psi_1 = |\psi_1(\mathbf{r},t)|\, e^{i\theta_1(\mathbf{r},t)}, \psi_2 = |\psi_2(\mathbf{r},t)|\, e^{i\theta_2(\mathbf{r},t)} \tag{2.26}$$

respectively, where $|\psi|^2$ is proportional to the density of electron pairs n and θ is the quantum phase. In the 1960s, Josephson [37] worked out the expression for the tunnelling supercurrent which has the following form:

$$I_s = I_J \sin\varphi \tag{2.27}$$

where I_J is the maximum pair tunnelling current that the junction can sustain (also called the Josephson critical current) and $\varphi = \theta_1 - \theta_2$ the phase difference between the left and right superconductors. The above equation suggests that there exists tunnelling current even though no bias voltage is present. Indeed, this effect was experimentally verified by Anderson and Rowell [38] and is called the *d.c. Josephson effect*. But what happens if a bias voltage ($V \neq 0$) is applied across the junction? It turns out the applied voltage V drives the evolution of the phase difference φ. The corresponding equation reads

$$\frac{d\varphi}{dt} = \frac{2\pi}{\Phi_0} V \tag{2.28}$$

where $\Phi_0 = \frac{h}{2e}$ the elementary magnetic flux quantum. This equation thus results in the appearance of an alternating current

$$I_s(t) = I_J \sin(\varphi_0 + \omega t) \tag{2.29}$$

where the oscillation frequency $\omega_J = \frac{2\pi}{\Phi_0} V$. This is the *a.c. Josephson effect*. Note that since the frequency-to-voltage ratio $\frac{f_J}{V} \sim {\Phi_0}^{-1} \sim 483$ MHz/μV [39], the typical oscillation frequency is about several hundred GHz at mV range. In addition, the coupling strength between the two superconductors is measured by the Josephson energy $E_J = \frac{I_J \Phi_0}{2\pi}$ which is the characteristic energy scale of the junction at zero bias voltage.

To derive the Josephson relations (Eqn. 2.27, Eqn. 2.28), I will follow Feynman's approach given in the famous Feynman lectures [1]. Assuming the

two superconductors in the Josephson junction are weakly coupled, the Schrödinger equation of the coupled system can be written as:

$$i\hbar\frac{\partial\psi_1}{\partial t} = E_1\psi_1 + K\psi_2 \tag{2.30a}$$

$$i\hbar\frac{\partial\psi_2}{\partial t} = E_2\psi_2 + K\psi_1 \tag{2.30b}$$

where K is the coupling constant between the superconductors, E the energy of an isolated superconductor and $E_2 - E_1 = (2e)V$. Inserting Eqn. 2.28 into the above equation and equating the real and imaginary parts of both sides of the equations we have

$$\dot{n}_1 = +\frac{2}{\hbar}K\sqrt{n_2 n_1}\sin\varphi \tag{2.31a}$$

$$\dot{n}_2 = -\frac{2}{\hbar}K\sqrt{n_2 n_1}\sin\varphi \tag{2.31b}$$

$$\dot{\theta}_1 = -\frac{K}{\hbar}\sqrt{\frac{n_2}{n_1}}\cos\varphi - \frac{(2e)V}{2\hbar} \tag{2.31c}$$

$$\dot{\theta}_2 = -\frac{K}{\hbar}\sqrt{\frac{n_1}{n_2}}\cos\varphi + \frac{(2e)V}{2\hbar} \tag{2.31d}$$

If pair current is defined as $I_s \equiv \dot{n}_1 = -\dot{n}_2$, the d.c. Josephson relation (Eqn. 2.27) is thus recovered where $I_J = \frac{2}{\hbar}K\sqrt{n_2 n_1}$. Subtracting Eqn. 2.31(c) from Eqn. 2.31(d) gives

$$\frac{d\varphi}{dt} = \frac{2e}{\hbar}V - \frac{K}{\hbar}\left(\sqrt{\frac{n_1}{n_2}} - \sqrt{\frac{n_2}{n_1}}\right)\cos\varphi \tag{2.32}$$

which differs from Josephson's original relation (Eqn. 2.28) by an additional cosine term. Ohta later realised that, in Feynman's approach, the contribution from the external circuit $W = \int IV dt$ is not considered, which represents the external energy transferred into the junction. By using a rigorous semi-classical analysis, Ohta recovered the strict a.c. Josephson relation [40].

Ambegaokar and Baratoff [41] calculated the d.c. Josephson tunnelling current in the framework of BCS theory for finite temperature. For identical superconductors the following relation is obtained:

$$I_J R_N = \frac{\pi\Delta(T)}{2e}\tanh\left[\frac{\Delta(T)}{2k_B T}\right] \tag{2.33}$$

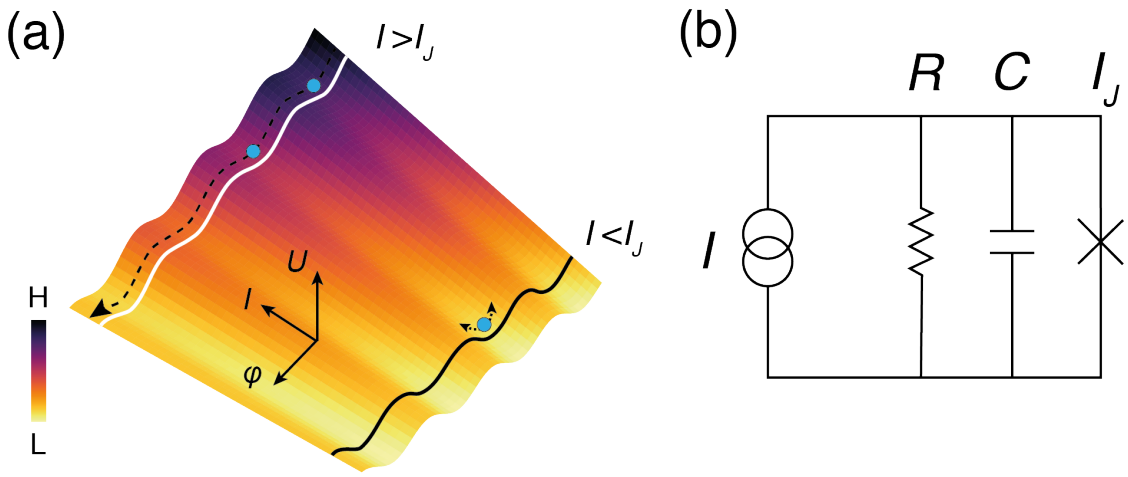

Figure 2.5: (a) The washboard potential as a function of the bias current I and the junction phase difference φ. When $I < I_J$, the ball is trapped inside one of the potential minima resulting in zero-voltage current flow. When $I > I_J$, the ball rolls down the washboard potential where the changing phase difference induces a finite voltage. (b) Circuit diagram of the RSCJ model.

where R_N is the normal state junction resistance and Δ the superconducting gap. At the case when $T = 0$, the previous equation is reduced to

$$I_J R_N = \frac{\pi \Delta(0)}{2e} \tag{2.34}$$

which indicates that the Josephson critical current I_J is a direct measure of the superconducting gap and, at least near T_c, the superconducting order parameter.

2.2.1 RCSJ model

The effective circuit of the Josephson junction can be seen as a parallel circuit consisting of a resistive element R_N, a capacitive element C, and the Josephson element with I_J as shown in Fig. 2.5(b). In the absence of fluctuations, an $I - V$ relation can be derived from the resistively- and capacitively shunted junction (RCSJ) model based on the analysis of Fig. 2.5(b)[42].

The total current injected into the junction can be written as (current conservation):

$$\begin{aligned} I &= I_C + I_R + I_S \\ &= C\frac{dV}{dt} + \frac{V}{R_N} + I_J \sin\varphi \end{aligned} \tag{2.35}$$

where the second step uses Eqn. 2.27. A changing phase difference induces a finite voltage, we can thus replace V with the a.c. Josephson relation. The above equation then becomes:

$$I = \frac{\Phi_0 C}{2\pi}\frac{d^2\varphi}{dt^2} + \frac{\Phi_0}{2\pi R_N}\frac{d\varphi}{dt} + I_J \sin\varphi \tag{2.36}$$

Rearranging terms we have

$$\left(\frac{\Phi_0}{2\pi}\right)^2 C\frac{\partial^2\varphi}{\partial t^2} + \left(\frac{\Phi_0}{2\pi}\right)^2 \frac{1}{R_N}\frac{\partial\varphi}{\partial t} + \frac{\partial}{\partial\varphi}U = 0 \tag{2.37}$$

where $U = -E_J\left[I_J\cos(\varphi) + I\varphi\right]$ is called the tilted washboard potential. The amplitude of the potential is the Josephson coupling energy E_J introduced earlier. The physical description of Eqn. 2.37 is analogous to the classical motion of a point-like particle rolling down the titled washboard potential U (Fig. 2.5(a), which is governed by the following equation [39]:

$$m\ddot{x} + \xi\dot{x} = -\frac{\partial w(x)}{\partial x} + F_{\text{ext}} = -\frac{\partial\left[w(x) - F_{\text{ext}}\,x\right]}{\partial x} \tag{2.38}$$

with the correspondence $m \leftrightarrow C, \frac{1}{R_N} \leftrightarrow \xi, I \leftrightarrow F_{\text{ext}}, \varphi \leftrightarrow x$, where ξ the friction coefficient, F_{ext} the external driving force that tilts the potential w.

In the RCSJ model, the d.c. Josephson effect corresponds to situation $I < I_J$, where the point-like particle is trapped in one of the potential wells of U and oscillates back and forth with the plasma frequency

$$\omega_{p,i} = \omega_p\left[1 - \left(\frac{I}{I_J}\right)^2\right]^{1/4} \quad \text{with} \quad \omega_p = \left(\frac{2\pi}{\Phi_0}\frac{I_J}{C}\right)^{1/2}. \tag{2.39}$$

Since in this state $\langle\dot{\varphi}\rangle = 0$, the average voltage V is also zero. For $I > I_J$, the washboard potential is tilted enough so that there are no local potential minima, and the point-like particle just keeps rolling. This dynamic case involves an evolving phase difference corresponding to a finite d.c. voltage across the junction.

Another important parameter of the model is the McCumber-Stewart parameter

$$\beta_c \equiv \frac{2\pi}{\Phi_0} I_J R_N^2 C$$

that describes the damping of the RCSJ circuit. Two limiting cases arise from the consideration of: 1) The strongly overdamped case ($\beta_c \ll 1$) and 2) The strongly

underdamped case ($\beta_c \gg 1$). When the circuit is strongly overdamped, the junction capacitance is negligible ($C \to 0$). A notable difference appears in the current-voltage relations of the two limiting cases while decreasing the bias current from above I_J. Because of the small inertia in the overdamped case, the particle will be instantly trapped into a local potential minimum and no current flows in the resistive channel but the non-dissipative Josephson channel. Solving Eqn. 2.37 in the limit $\beta_c \to 0$ we have

$$V = 0 \text{ for } I < I_J$$

$V(t) = R_N \frac{I^2 - I_J}{I + I_J \cos \omega t}$ for $I > I_J$ with $\omega = \frac{2\pi I_J R_N}{\Phi_0} \sqrt{\left(\frac{I}{I_J}\right)^2 - 1}$. The voltage is thus oscillating with time with a frequency determined by the current amplitude (Fig. 2.6(c) for $I > I_J$. The time-averaged voltage $\langle V \rangle = 0$ when $I < I_J$ and increases with bias current as I exceeds I_J :

$$V = R_N \sqrt{I^2 - 1} \text{ for } I > I_J \tag{2.40}$$

The overdamped current-voltage relation is plotted in Fig. 2.6(a).

For the strongly underdamped limit where the capacitance has a sizable value, the particle has a large enough inertia that it cannot be immediately trapped into the potential minimum but keeps rolling to the next minimum as the bias current decreases from I_J. This results in a finite voltage at $I < I_J$ (Fig. 2.6(b)). In this case, the current-voltage relation exhibits strong hysteresis.

2.2.2 Thermal fluctuations in the Josephson junction

In practice, thermal fluctuations will often render d.c. Josephson current measurements impractical. This is because for a typical SJTM junction where $R_N = 1$ GΩ and $\Delta = 1$ meV, I_J is about 1.5 pA according to Eqn. 2.34. The Josephson energy is then about 5 neV which corresponds to 30 μK. This is generally not accessible even with a dilution-fridge-based STM. However, it is still possible to have pair-tunnelling current at finite voltages while $I < I_J$. This is because in the overdamped regime of the RCSJ model, while the particle is locked in a local

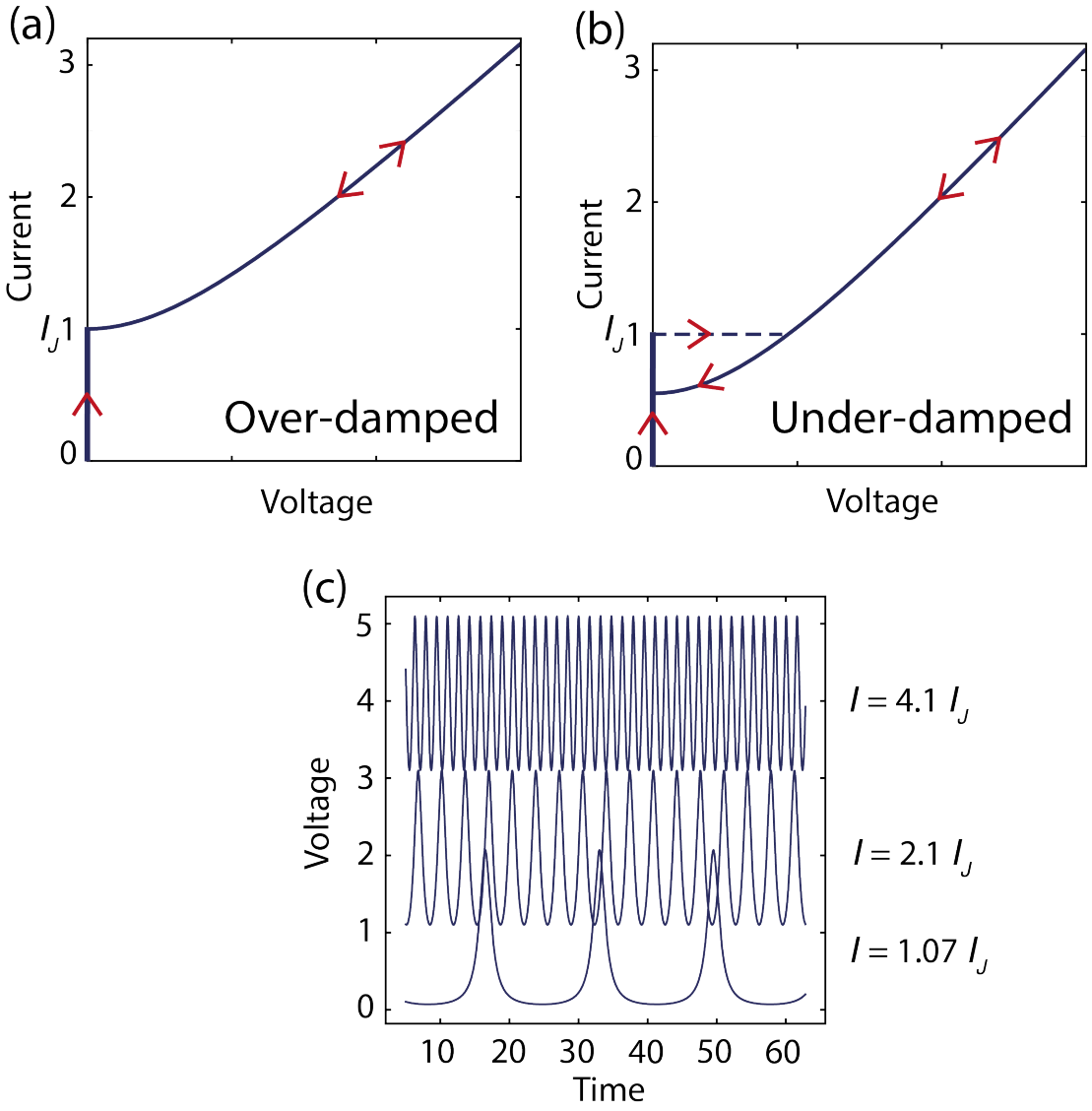

Figure 2.6: Schematics of the Josephson junction current and voltage dynamics. (a) $I-V$ characteristics in the over-damped regime. (b) $I-V$ characteristics in the under-damped regime where a significant hysteresis is present. Sweeping directions are indicated with red arrowheads. I_J is set to 1. (c) $V(t)$ characteristics while $I > I_J$ for different values of I. Figure adapted from [39].

minimum in the tilted washboard potential, thermal fluctuation can still knock it out of the potential well which induces a changing phase difference. Typically, this situation happens when the thermal fluctuation energy k_BT is much greater than the potential barrier E_J so that

$$\frac{E_J}{k_BT} \ll 1. \tag{2.41}$$

Indeed, Ivanchenko and Zil'berman [43] derived the $I-V$ relation for the electron-pair tunnelling in the presence of thermal fluctuations and found that the maximum pair tunnelling current at a finite voltage is proportional to the Josephson current, which corresponds to the superconducting order parameter. This is the I-Z model that establishes the foundation of the SJTM principle.

In the I-Z model, the thermal fluctuation is introduced as an additional Johnson noise term $V_N(t)$ to the applied emf E. In the limit of $R_N \to \infty, C \to 0$, Eqn. 2.37 becomes

$$\frac{1}{Z}\frac{d\varphi}{dt} = -\frac{2e}{\hbar} I_J \sin\varphi + \frac{2e}{\hbar}\frac{E+V_N(t)}{Z} \tag{2.42}$$

where Z is the external impedance of the environment that is assumed to be constant, namely, $Z_{\text{ext}}(\omega) = Z$. According to the classical Nyquist-Johnson formula, $V_N(t)$ satisfies $\langle V_N(t)V_N(0)\rangle = 2k_BT^*Z_{\text{ext}}\,\delta(t)$ with T^* being the effective noise temperature of the external circuit. It is evident that the thermal noise is white noise so that $\langle V_N(t)\rangle = 0$. Eqn. 2.42 can now be seen as the Langevin equation [39] of the phase difference. The corresponding Fokker-Planck equation then describes a particle that undergoes Brownian motion and diffuses down the washboard potential (Fig: 2.5(a)) that is activated by thermal fluctuations:

$$\frac{\partial W}{\partial t} = D\frac{\partial^2 W}{\partial \varphi^2} + \Omega\cos\varphi W + (\Omega\sin\varphi - \Omega_0)\frac{\partial W}{\partial \varphi} \tag{2.43}$$

where $W = W(\varphi, t \mid \varphi_0, t_0)$ is the probability density of finding the phase difference in the interval $\varphi_0 + d\varphi$ at time t given that $\varphi = \varphi_0$ at time t_0 and $\Omega = \frac{2eZI_J}{\hbar}, \Omega_0 = \frac{2eE}{\hbar}$ and $D = T^*Z\left(\frac{2e}{\hbar}\right)^2$. Thus, the I-Z model is said to be in the *phase-diffusive regime*. The d.c. Josephson current can then be calculated via

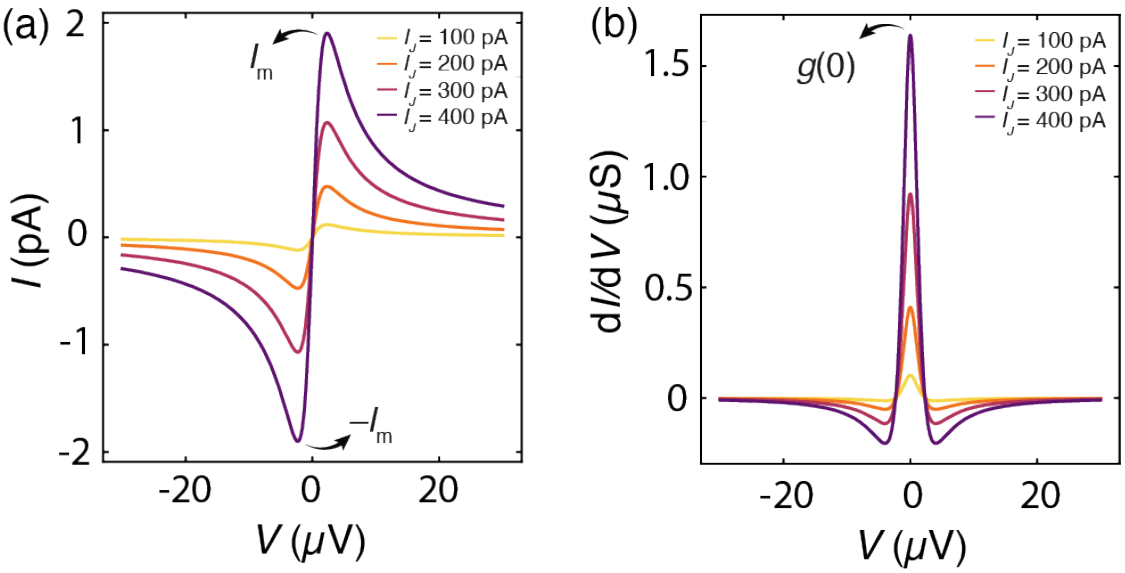

Figure 2.7: Numerical plots of $I-V$ (a) and dI/dV (b) characteristics in the phase-diffusive Josephson tunnelling regime. Parameters used: $T^* = 0.5$ K, $Z = 110\ \Omega$.

$$I = I_J\langle \sin\varphi\rangle = I_J \lim_{t\to\infty}\int_{-\infty}^{\infty} d\varphi \sin\varphi W\left(\varphi, t \mid \varphi_0, t_0\right) \tag{2.44}$$

where $t\to\infty$ ensures the system is at equilibrium where $\lim_{t\to\infty}\frac{\partial W}{\partial t} = 0$. Solving for W in Eqn. 2.43 and inserting back into the Eqn. 2.44, we have the explicit pair-tunnelling $I-V$ relation in the limit $\frac{E_J}{k_BT} \ll 1$:

$$I(V) = \frac{I_J^2 Z}{2}\frac{V}{V^2+V_c^2} \tag{2.45}$$

where $V_c = \frac{2eZkT^*}{\hbar}$. Numerical plots of this $I-V$ relation with different junction resistance is plotted in Fig. 2.7(a). By taking the derivative, a zero-bias conductance peak that is characteristic of the phase-diffusive pair tunnelling is shown in 2.7(b). Most importantly, the maximum current is directly related to the Josephson critical current through

$$I_m = \frac{\hbar}{8ekT^*}I_J^2. \tag{2.46}$$

Therefore, one can directly access the superconducting order parameter (electron-pair density) by measuring the $\sqrt{I_m}R_N$ product in the phase diffusive channel as demonstrated by the following relation

$$\sqrt{I_m}R_N \propto I_J R_N \propto \langle c_\uparrow c_\downarrow\rangle_1 \langle c_\uparrow c_\downarrow\rangle_2 . \tag{2.47}$$

By the help of microscopes, there is nothing so small, as to escape our inquiry; hence there is a new visible world discovered to the understanding.

— Robert Hooke

3

Gemini: a next generation STM

Contents

In this chapter, I will introduce the development of a fourth-generation home-built scanning tunnelling microscope (STM) called Gemini, housed at the ultra-low vibration laboratory about 20 metres underground in the basement of the new Beecroft building in Oxford.

The microscope is designed to be operated at extreme conditions - millikelvin temperature, ultra-high vacuum, and high magnetic field (14 T). The mK-STM is designed to have dual functionality: SI-STM, which features single electron tunnelling and SJTM, which features cooper pair tunnelling using a superconducting

tip. A photograph of the Gemini STM is shown in Fig. 3.1. During my DPhil, I built the instrument from an empty laboratory and played a key role in the microscope's assembly, testing, upgrading, and operation. Examples include but are not limited to assembling the entire instrument, the design and construction of the $^3\mathrm{He} - {}^4\mathrm{He}$ mixture and vacuum pumping system, testing and upgrading the system's cryogenic performance, testing and upgrading the cryogenic sample transferring and cleaving system, optimising the system's noise performance and making topographic and spectroscopic imaging measurements. Detailed design and testing results are presented below.

3.1 Vibration isolation

Since the tunnelling current exponentially depends on the Z distance to the sample, suppressing the vibration noise is critical in building a successful STM. In the Gemini system, vibration isolation is achieved through multiple stages. A schematic is shown in Fig. 3.2. First, the entire experimental apparatus sits on top of a 30-ton concrete plinth or the 'Keel Slab' that is floating on six air isolators ($f_0 < 1$ Hz). On top of this, the entire UHV chamber and the cryostat are mounted on a 2-ton rectangular table filled with lead shots (#8 2.2 mm diameter), which is floating on a second stage of 4 air isolators ($f_0 \approx 1.2$ Hz) sitting on two table supporting legs filled with sands and lead bricks. The vacuum gas tubes from the vacuum chamber and the cryostat are first anchored at the table legs and then go through a floor manifold firmly cemented into the B2 floor. Then, on the lower floor, level B3, the tubes go through a second cemented manifold before reaching the pump room separated from the STM by an acoustic wall. To minimise acoustic noise, the experimental room is covered with acoustic-absorbing foam and the entire experimental floor is covered with carpet. To model the entire vibration-damping system, let us start with a damped forced harmonic oscillator model for the STM tip with external acceleration $a(t)$. The equation of motion reads

$$\ddot{x} + \beta\dot{x} + \omega_0^2 x = a(t) \tag{3.1}$$

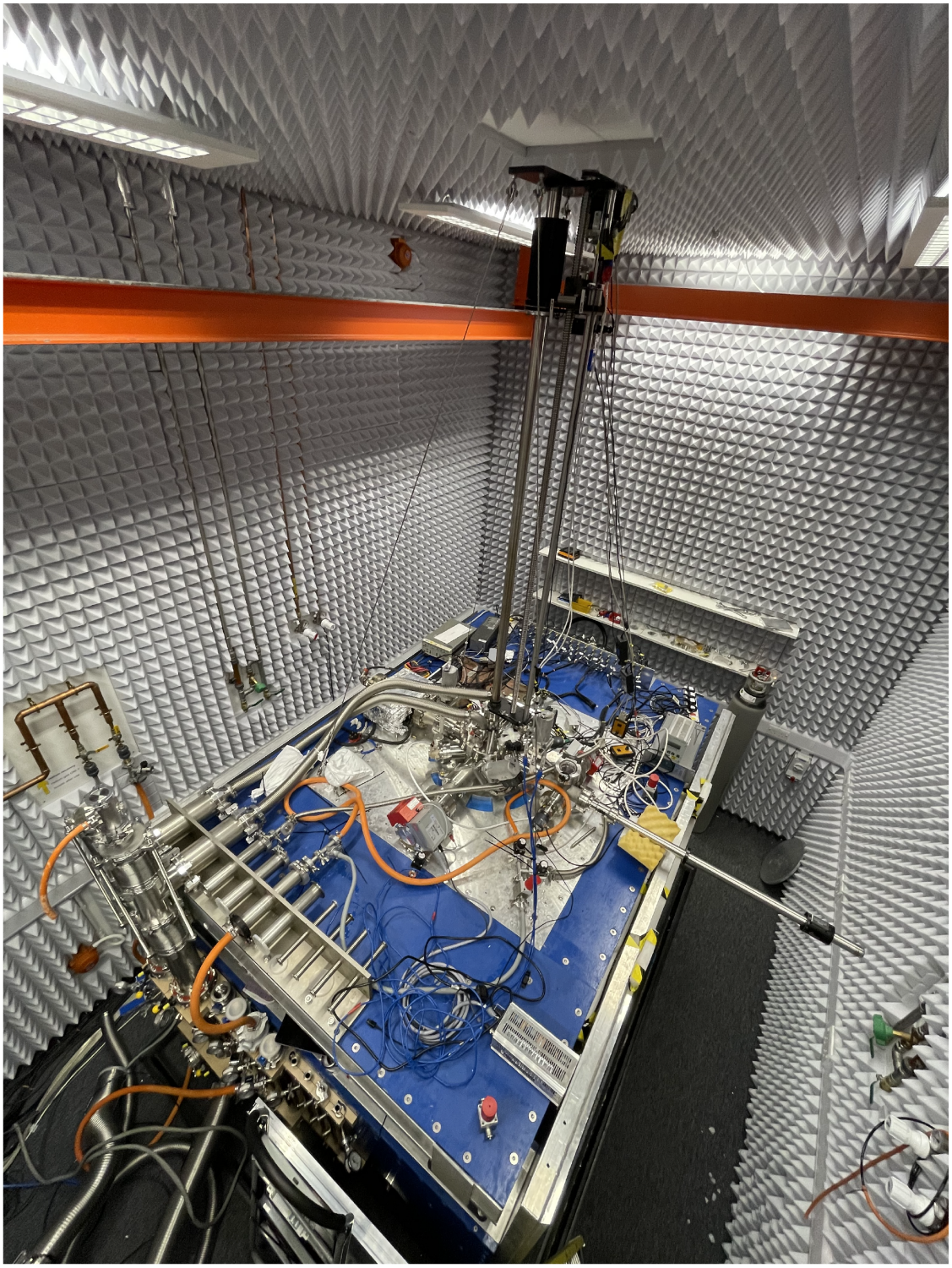

Figure 3.1: Photograph of the Gemini STM (October 2023).

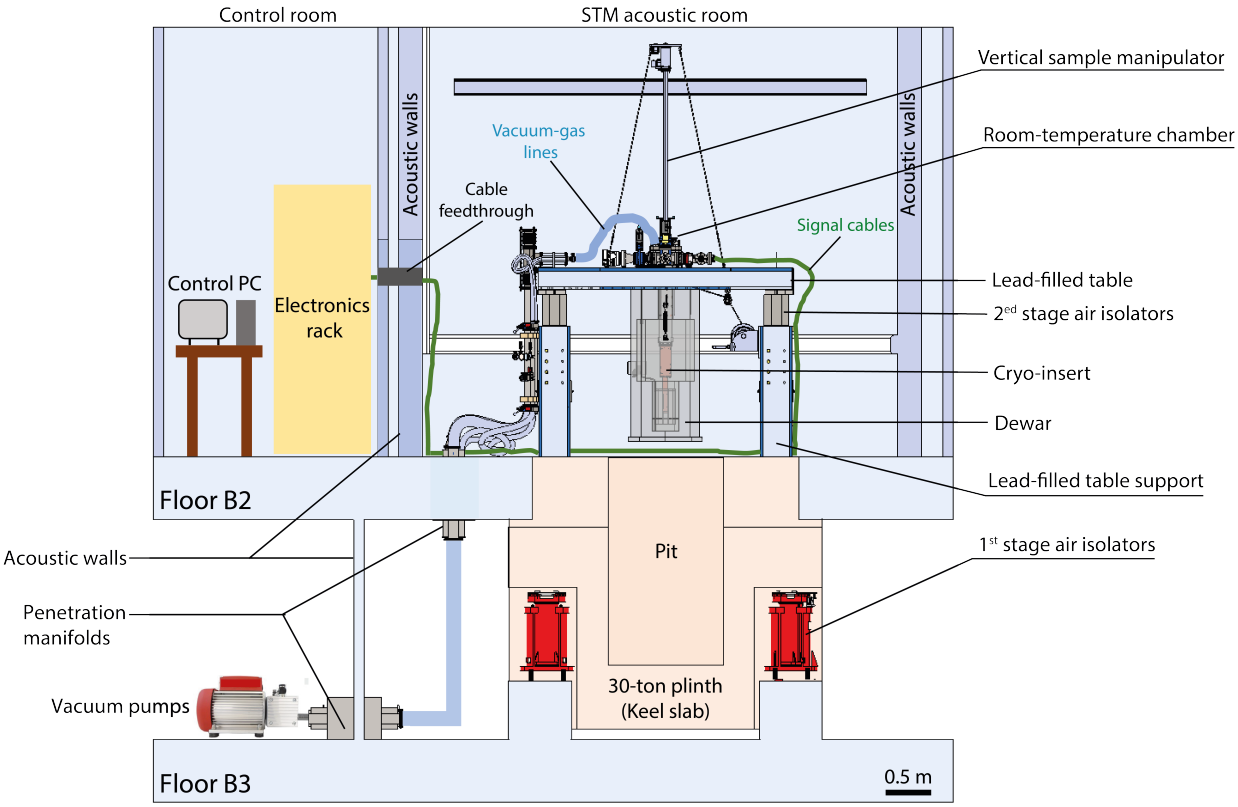

Figure 3.2: Section view of the ultra-low vibration (ULV) laboratory that houses the Gemini STM at the basement of the Beecroft building about 20 m below the ground. The entire apparatus rests on a 30-ton concrete "keel slab" that is floated on six air isolators. All the vacuum and gas pumps are placed in a separate acoustic room (B3) below the experimental floor (B2).

where $\omega_0 = \frac{k}{m}$, β consists of the damping constant and x is the Z displacement of the STM tip. Solving this differential equation yields

$$x(\omega) = \frac{a(\omega)}{\sqrt{(\omega_0^2 - \omega^2)^2 + (\beta\omega)^2}}. \tag{3.2}$$

With a typical $\omega_0 \approx 3000$ rad/s at the STM tip, achieving atomic resolution with a noise displacement amplitude of $\delta x < 10^{-14}$ m/$\sqrt{\text{Hz}}$ then requires the corresponding acceleration noise to be $\delta a < 10^{-7}\frac{\text{m}}{\text{s}^2}/\sqrt{\text{Hz}}(\omega \to 0)$. The measured noise spectra for the Gemini STM are shown in Fig. 3.3. With all these noise isolation methods in place, the tip vibration amplitude can be in the order of 1 fm (Fig. 3.3(a)). The current background noise is suppressed to below 10 fA (Fig. 3.3(b)). And the vibration velocity measured on the STM table is below $10^{-7}\frac{\text{m}}{\text{s}}/\sqrt{\text{Hz}}$ (Fig. 3.3(c)).

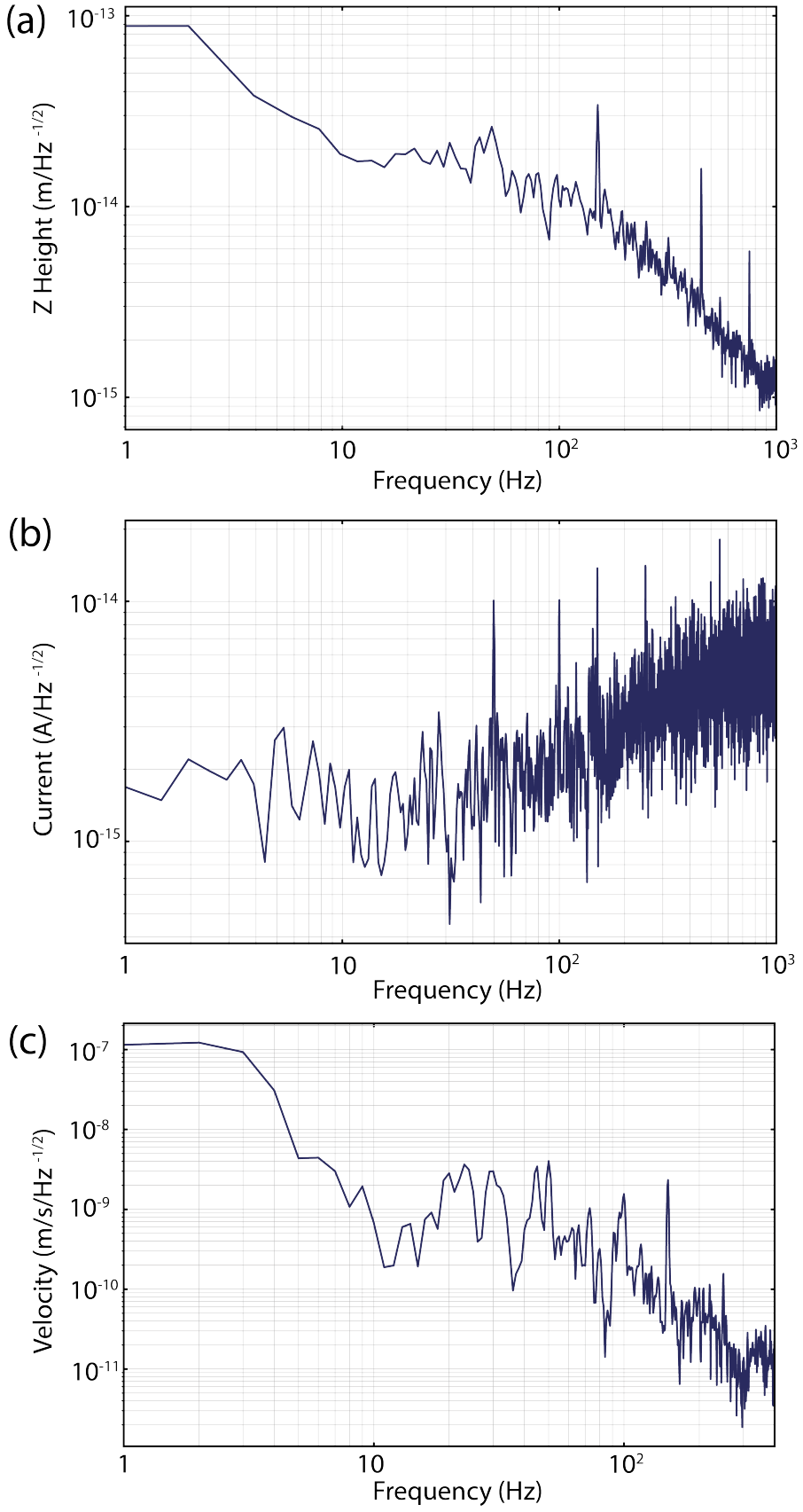

Figure 3.3: Vibration isolation characteristics. Measurements were taken while all stages of air isolators were turned on. (a) Power spectral density (PSD) measurements of the scan piezo Z height. The 1 K pot pump was turned on. (b) The background current PSD vs frequency plot while the tip was withdrawn and the 1 K pot pump was turned off. (c) PSD measurements of velocity vs frequency taken on the STM table.

3.2 STM head

The STM head is the microscope's core component, where the phenomena of 'scanning' and 'tunnelling' occur. The head is firmly attached to the cryostat base (the pedestal), where it has the lowest temperature. Its design follows from an earlier version [44] that utilizes a sliding motion produced by stacked shear piezo motors for tip approaching. Views of the STM head are shown in Fig. 3.4. The core structure of the head is crafted from a single block of machinable ceramic (Macor), characterized by its relatively high thermal and low electrical conductivity. Within this structure, a coarse-approach mechanism is housed. This mechanism encompasses a piezo-tube scanner (to which the STM tip is connected) and a polished sapphire triangular prism. This prism is securely fastened by six-shear piezo motors attached to the head body. On top of the piezo tube is a brass-made sample receptacle ensuring sturdy thermal and electrical connections with the sample. At the prism's base, two cylindrical capacitors are arranged concentrically as a position sensor to gauge the motor's location.

The shear piezo motors employ a distinct 'walking' mechanism for movement. To initiate this, each component of the motor, referred to as a 'walker', advances individually by applying a high voltage, approximately 300 V, at liquid Helium temperature. During this process, the sapphire prism is held fixed due to friction. Following this individual advancement, all walkers collectively move together to have the sapphire prism move into its new positions. Next, each walker moves back individually before starting a new movement cycle. The walker movements are recorded by recording the capacitance change of a co-axial capacitor (the position sensor as shown in Fig. 3.4(a)). Records of walker movement cycles at room and liquid He temperatures are shown in Fig. 3.5.

The scan tube is made of a material that exhibits the piezoelectric effect. By applying external stress, an electric field is induced inside the material. The inverse process also holds, i.e. the applied electric field generates internal mechanical strain. The piezo scan tube is cut into a cylindrical shape where its inside is coated with a

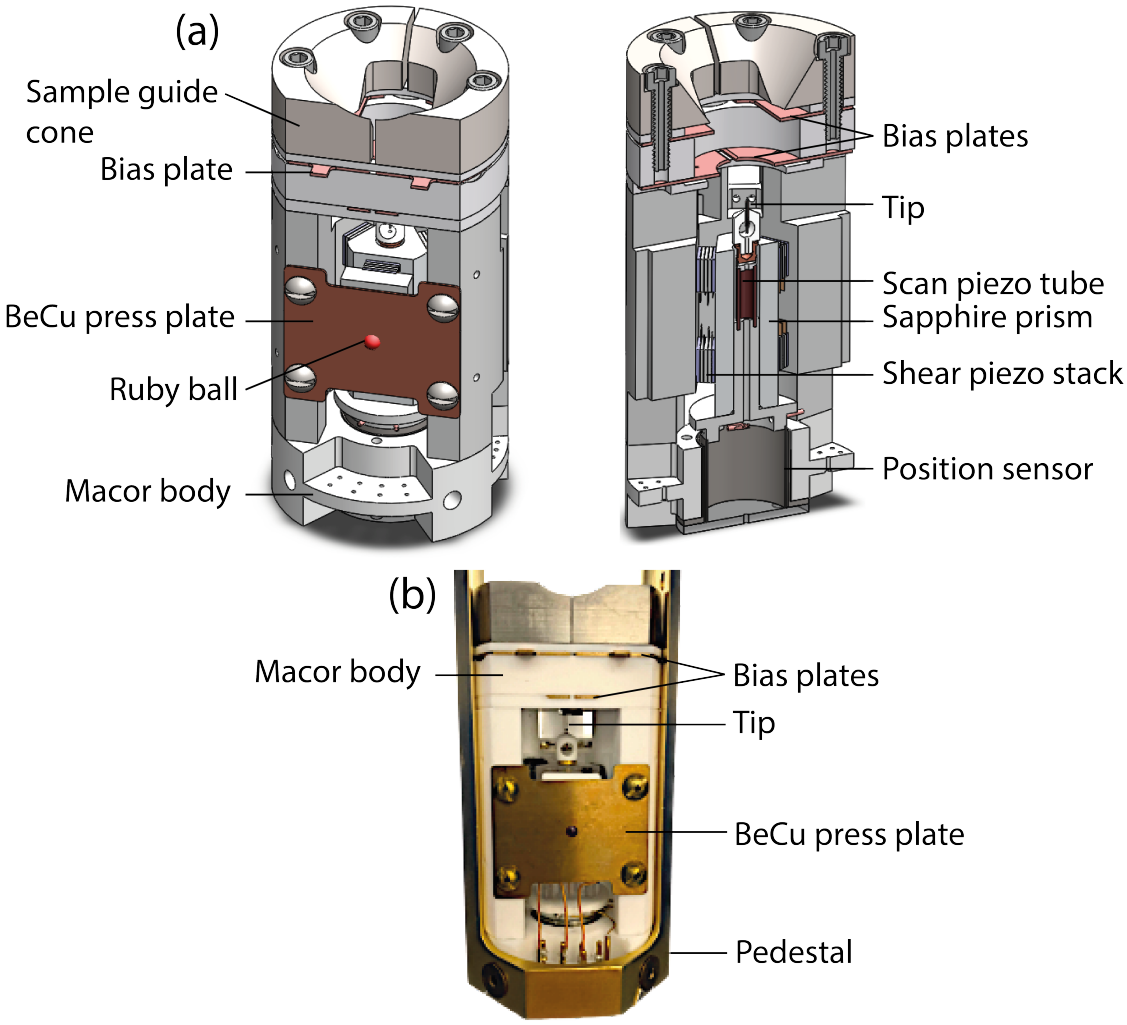

Figure 3.4: (a) CAD trimetric and section view of the Gemini STM head. The sample is placed between the upper and lower bias plates. (b) Photograph of the STM head on board the cryo-insert pedestal.

metal electrode for Z (vertical) motion and its outside is coated with four equally divided electrodes for ±X and ±Y (horizontal) motions.

A tip-approaching procedure can be established with the shear walkers and the scan tube: 1) Z electrode voltage is ramped from -400 V to 400 V (piezo tube extends to its maximum length). 2) Z electrode voltage returns to -400 V (piezo tube retracted). 3) Shear piezo walkers walk one step further. 4) Repeat the process until the tip reaches the tunnelling regime of the sample surface. Once the tip has approached the sample surface, scanning can start. Topographic scanning images of various samples taken by the Gemini STM are shown in Fig. 3.6.

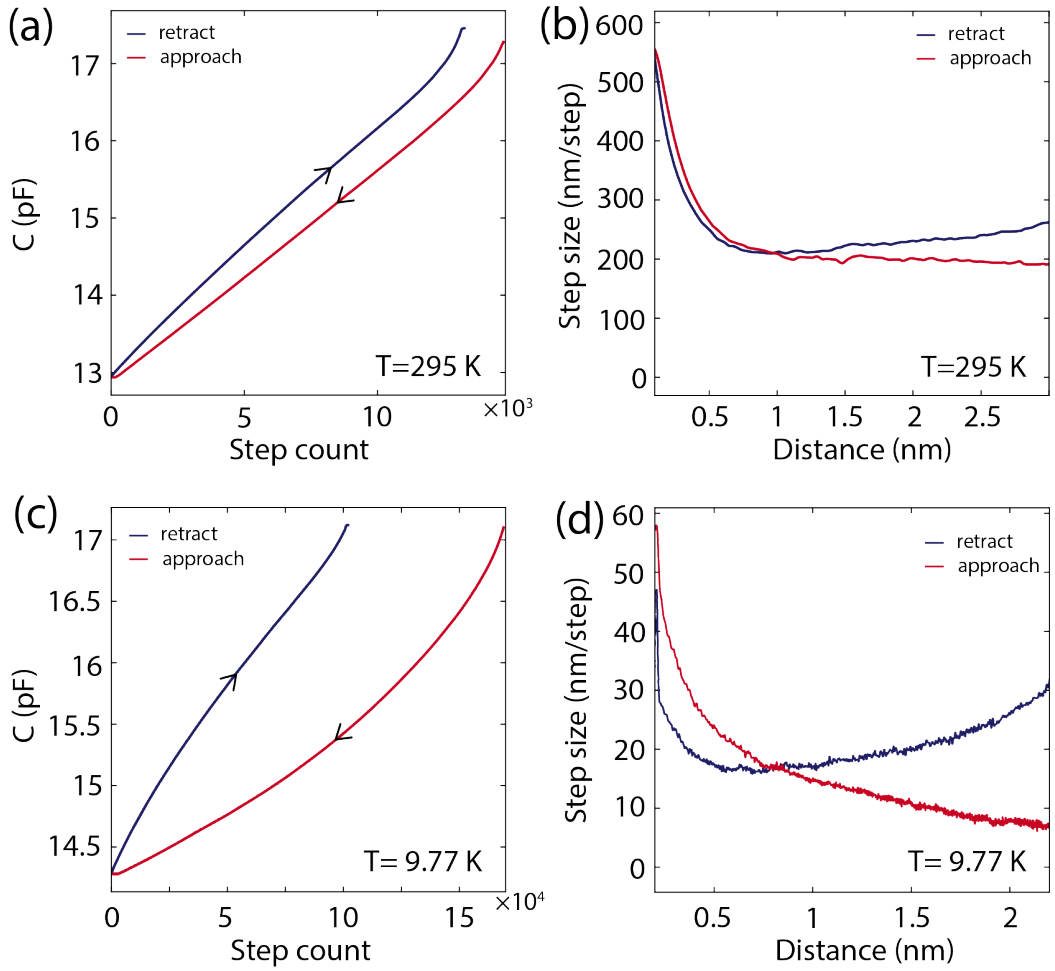

Figure 3.5: (a),(c) Tip position sensor capacitance as a function of shear piezo walker step count at different temperatures. Black arrows indicate walker walking directions. (b), (d) STM shear piezo walker step size at different temperatures.

3.3 Electronics

3.3.1 Current amplifier

The first electronic device that the tunnelling current passes through is the preamplifier (or transimpedance amplifier), which consists of an effective operational amplifier and a feedback resistor. A circuit diagram is shown in Fig. 3.7. Its essential function is to convert the current signal to a voltage signal. In practice,

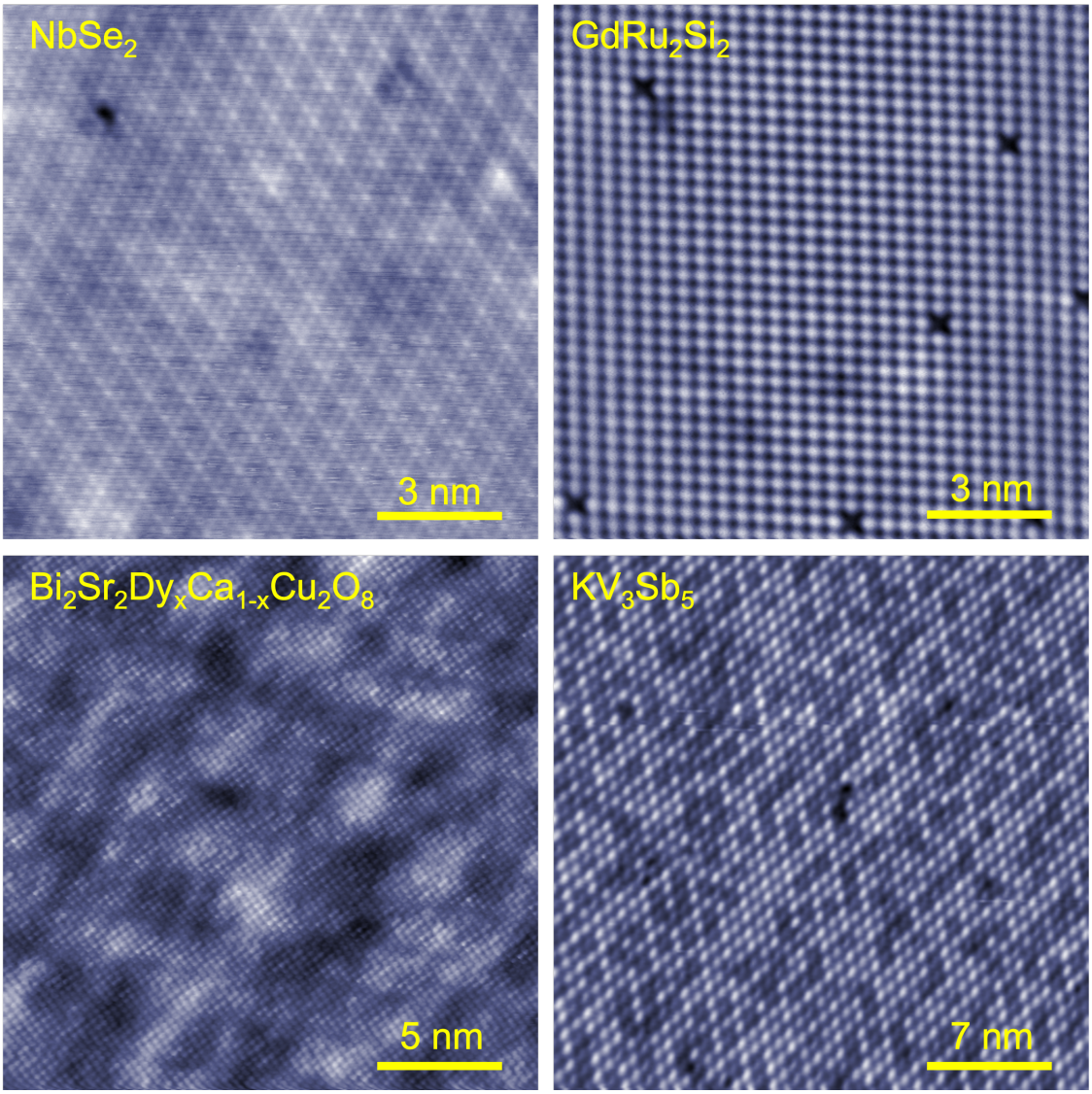

Figure 3.6: Sample topographies that I have taken using the Gemini STM throughout my DPhil.

the tunnelling current is in the range of tens of pA, and this results in an output voltage of several hundred mV (In my case, gain=100 pA/V). The noise level of the current pre-amplifier is crucial, as it determines the noise level of the experimental data. The chosen pre-amplifier (NF SA-607F2) has extremely low noise, achieving as low as 2.5 fA/$\sqrt{\text{Hz}}$. In addition, the pre-amplifier has adjustable bandwidth up to 10^4 Hz. This gives advantages such as enabling high-frequency selection of the lock-in modulation voltage, which reduces the required settling time in bias spectroscopy and in turn, decreases the time required to perform spectroscopic

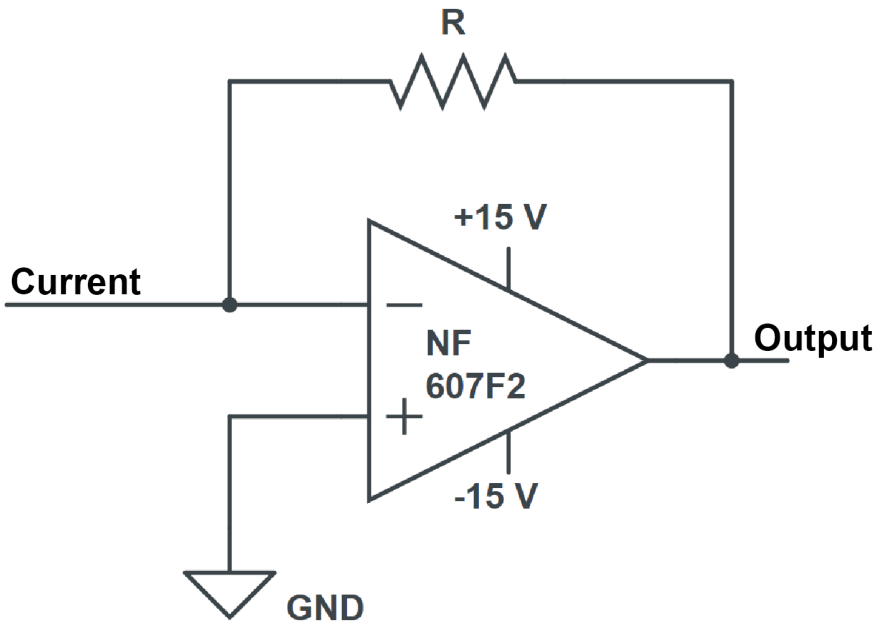

Figure 3.7: Current pre-amplifier circuit diagram.

mapping. During field emission on Au for tip preparation, the bias voltage can be as high as 200 V, corresponding to the current of several μA. This easily exceeds the maximum input ($\pm$1 nA) of the pre-amplifier and can cause irreversible damage. I thus use a separate amplifier with a small gain (Gain=1 μA/V) for field emission.

3.3.2 Control electronics

The electronic control unit (ECU) for the Gemini STM is provided by a commercial system (Nanonis), which consists of four instruments: a Real-time Controller (RC5), a Signal Conversion Interface (SC5), a High Voltage Amplifier (HVA4) and a High Voltage Supply (HVS4). Fig. 3.8 shows a detailed electronics wiring diagram. The RC5 has a built-in central processing unit (CPU) and a field-programmable gate array (FPGA), which is the central data processing device or the 'brain' of the entire ECU. It also provides digital communication to other Nanonis instruments and the host computer that runs the Nanonis software. The SC5 has a digital-analogue conversion interface connected to RC5 for computer control. Inside SC5, the digital signal from the computer is converted to its analogue form, such as the bias voltage and the analogue input signal is digitalised such as the tunnelling current. The HVA4 provides a high voltage gain of up to 400 V for applications such as the scanning

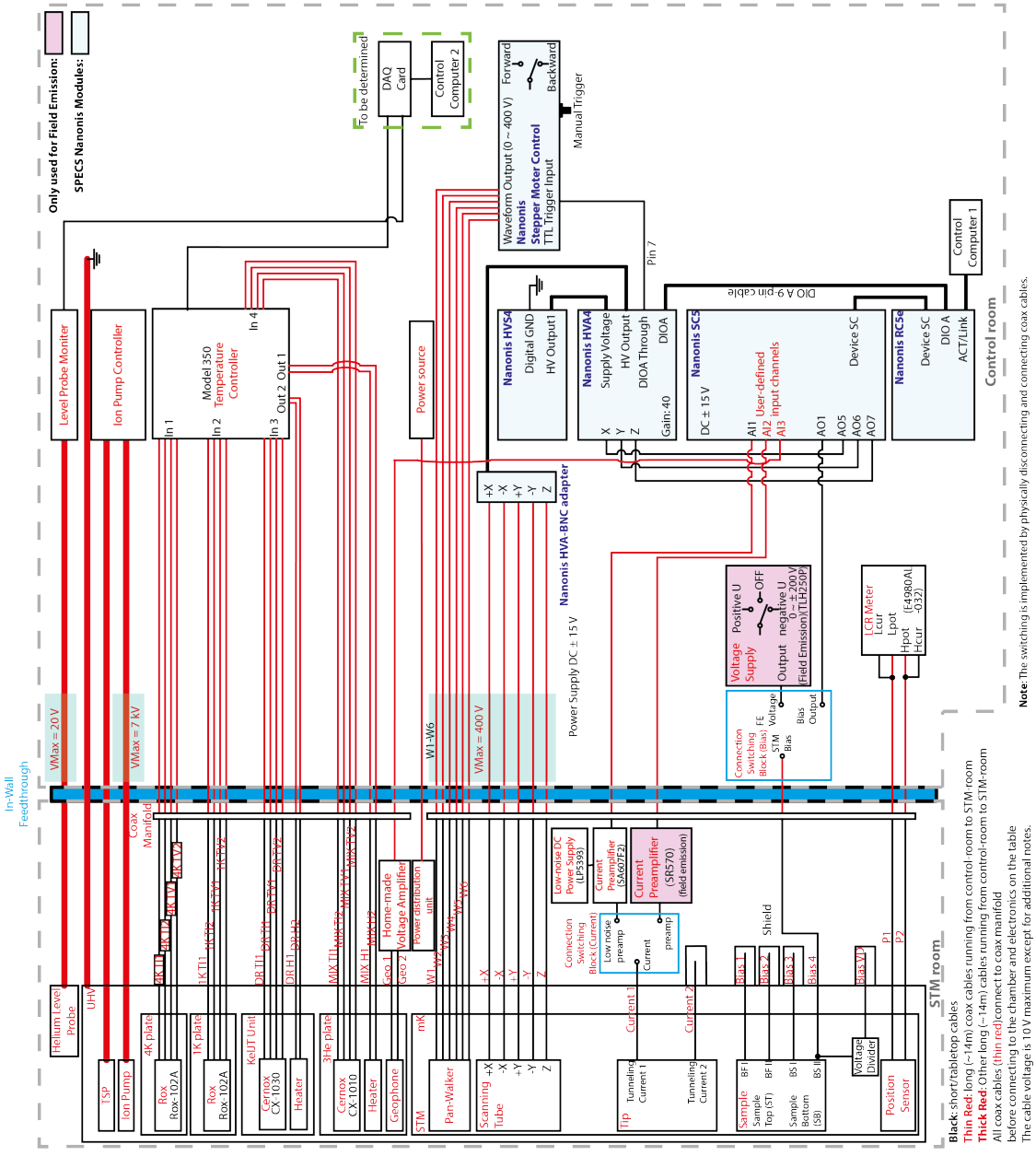

Figure 3.8: Gemini electronics block diagrams. The thick blue line represents the acoustic isolation wall that separates the control room from the experimental STM room on floor B2.

of the piezo scan tube. Together, the Nanonis system offers a range of essential functions that include various adjustable parameters for STM. Examples include PID control for scan tube Z movement, lateral scan control, lock-in amplifier, etc.

3.3.3 Temperature monitoring and control

Reliable temperature monitoring is important in cryostat design. For the Gemini STM, I use LakeShore ruthenium-oxide (RTD) thermal sensors and LakeShore Model 350 for temperature monitoring and control. On the 4KP and 1KP are the ROX type (RX-103A) RTS sensors, which are useful in measuring temperatures from 1.4 K to 40 K. The ROX sensors are not individually calibrated but are provided with a universal resistance-temperature calibration curve. On the Still and Mix plates are the Cernox-type RTD sensors (CX-1010) that can measure from 100 mK to 420 K. These Cernox sensors are individually calibrated and provide very high-resolution temperature measurements. Each of the sensors introduced above has 4 electrodes attached, i.e. +I, -I, +V, -V, which are fed into the Model 350 control for resistance measurements using the four-point probe method. For temperature control, a 100 Ohms resistor is installed on the Mix plate that is connected to the 1 W output of the Model 350 controller, and another 100 Ohms resistor is installed on the Still plate that is connected to the 75 W output of the Model 350 controller. A closed-loop PID is used to maintain the temperature to a specific setpoint. The heater output is given by

$$\text{Heater Output } = P\left[e + I\int(e)dt + D\frac{de}{dt}\right] \tag{3.3}$$

where e = setpoint - temperature reading. With appropriately chosen P, I and D parameters, the temperature fluctuation amplitude of the Gemini STM can be suppressed within 1 mK.

3.4 UHV and sample transfer

The vacuum system consists of the main chamber, cryogenic vacuum cans and a load-lock chamber (LLC). A gate valve separates the main chamber from the LLC.

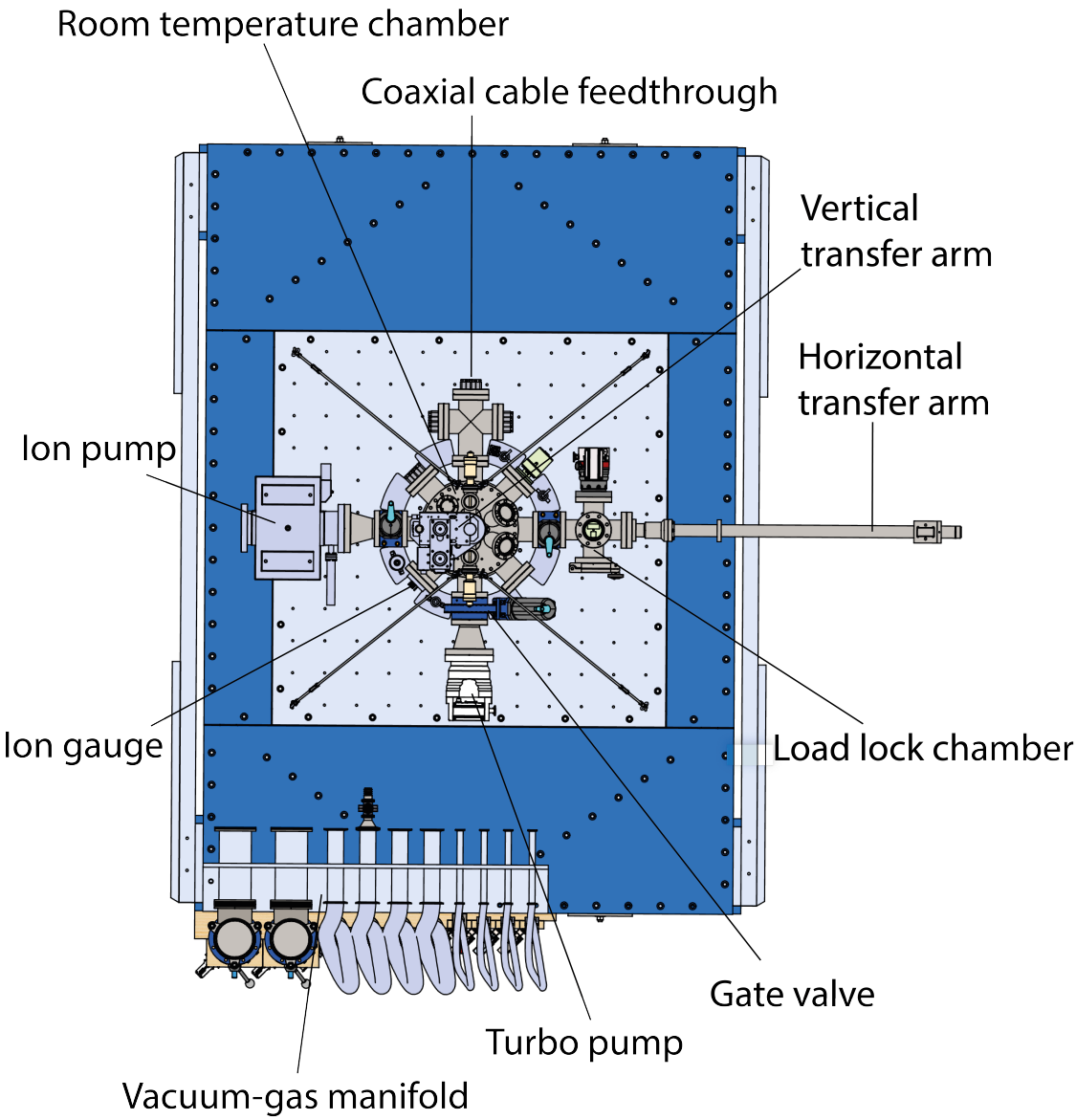

Figure 3.9: Top view of the UHV system. It consists of three main parts: load lock chamber, room-temperature (RT) chamber and sample transfer manipulators.

A turbomolecular pump is connected to the main chamber for the initial pumping down. During stable operation at liquid Helium temperature, only the ion pump is turned on continuously, and the system is under ultra-high vacuum (UHV) with main chamber pressure around 10^{-10} Torr at room temperature without baking. The LLC itself also has its turbomolecular pump. Top and cross-sectional views of the UHV system are shown in Fig. 3.9 and Fig. 3.10, respectively.

The sample transfer process is designed to occur inside UHV and consists of horizontal and vertical transfer arms. The transfer arms are magnetically coupled

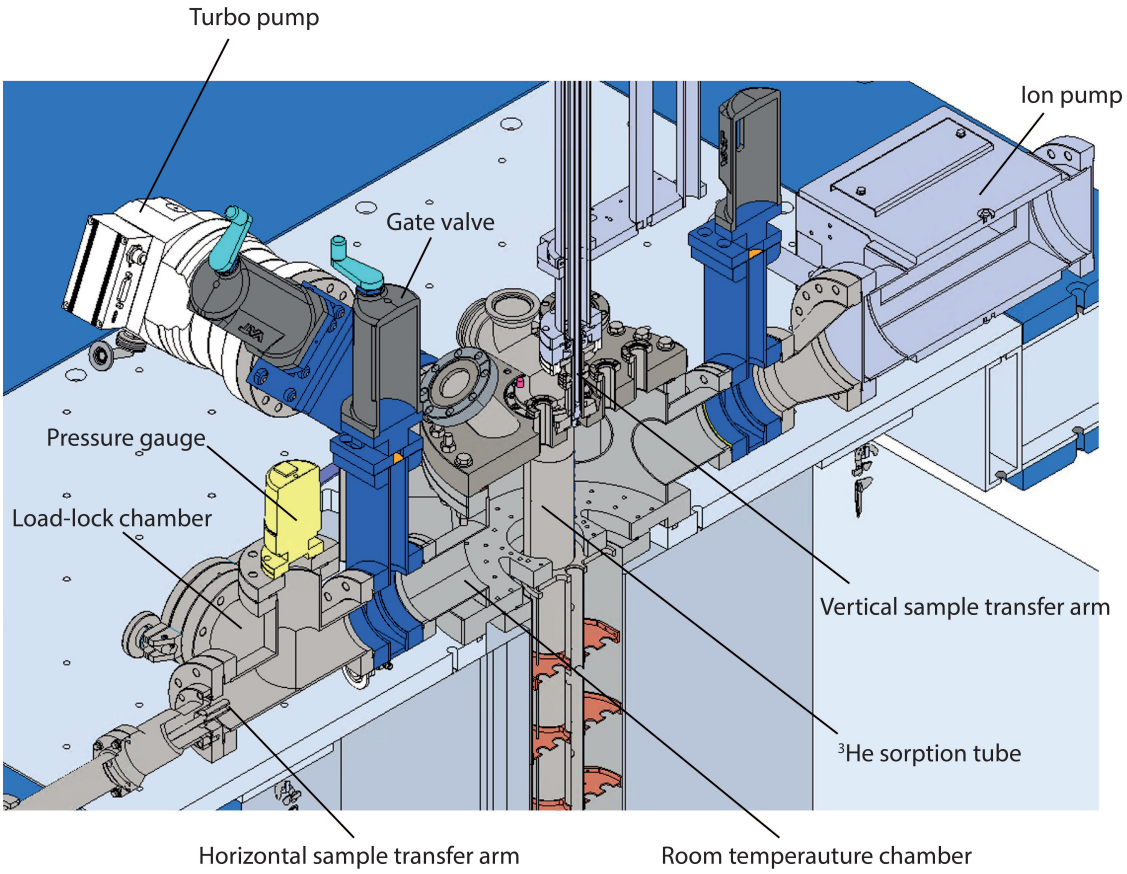

Figure 3.10: CAD section drawing of room-temperature UHV chambers. The sample is inserted into the load lock chamber and then to the vertical transfer arm via the horizontal transfer arm before moving downwards to the STM head.

to the magnets outside the vacuum system and can thus be moved from outside. The sample transferring procedure is as follows. The horizontal transfer arm sends the sample from the LLC to the centre of the main chamber. The vertical arm then grabs the sample from the horizontal arm. After the horizontal arm is retracted to the LLC, the vertical arm sends the sample down to the 4 K plate for *in situ* cleavage. Then, the cryogenically cleaved sample is inserted into the STM head. Finally, the vertical arm is retracted to the home position in the main chamber.

3.5 Refrigeration

The refrigerator is a wet dilution system designed to operate at tens of mK. It comprises several components that are discussed in detail in the following sections. A comprehensive vacuum-gas diagram for the refrigerator is shown in Fig. 3.11.

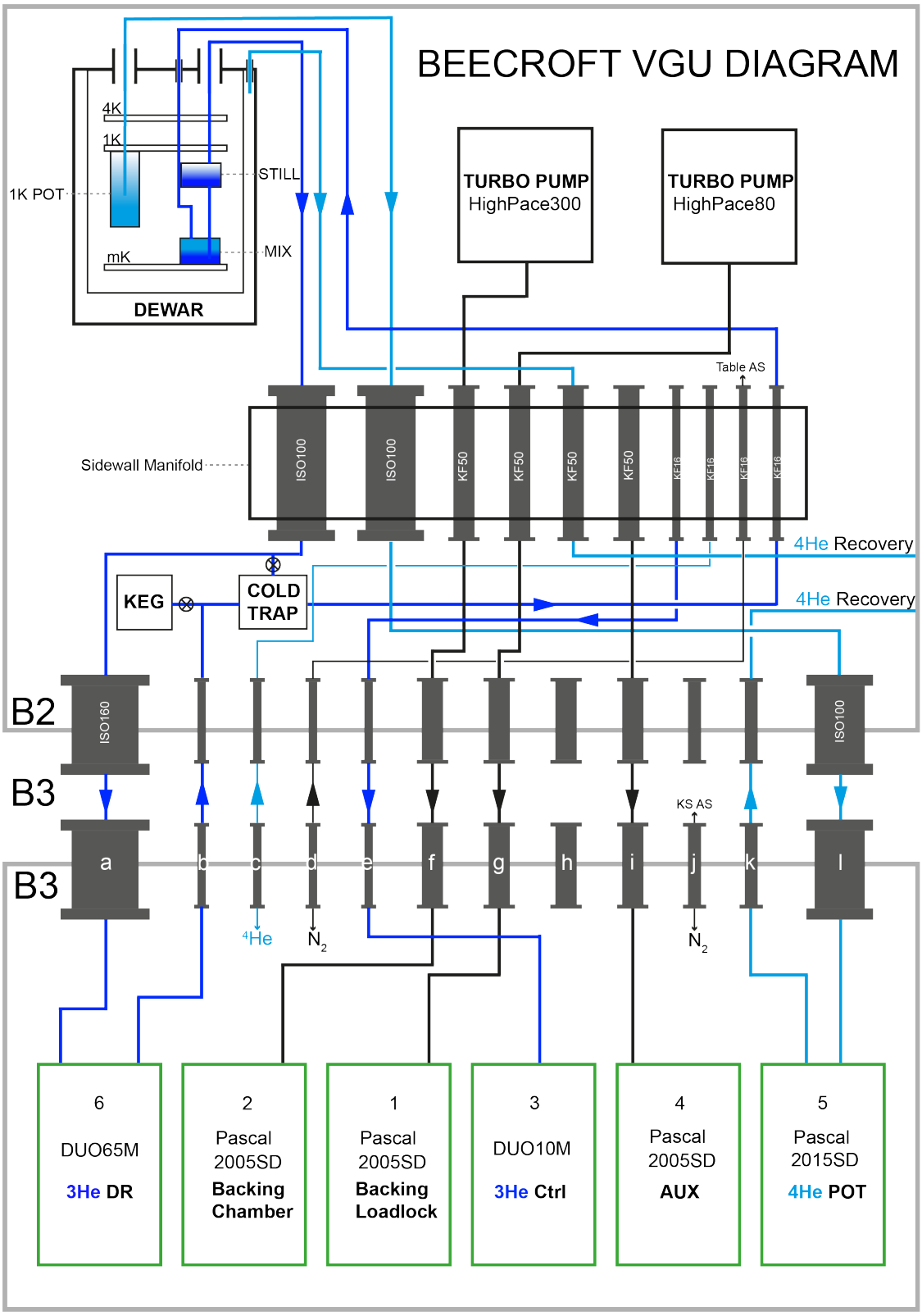

Figure 3.11: Gemini vacuum-gas block diagrams. Green boxes: vacuum pumps. "I" shapes: vacuum tubes with flanges. Blue lines: ^{3}He gas lines. Sky blue lines: ^{4}He gas lines.

3.5.1 Dewar

The Dewar is a double-walled liquid Helium (LHe)[1] container that houses the cryogenic insert. It has a vacuum jacket that separates the inner cryogenic environment from the hot outside world. The boil rate is an essential parameter of a research Dewar. It determines the experimental hold time and the noise level, which are crucial to SI-STM studies. Thus, minimising heat transfer to the LHe reservoir is crucial in the Dewar design. To reduce the heat conduction via residual gas molecules in the vacuum jacket, the vacuum level should be low enough so that the effective jacket size L is less than the collisional mean free path l of the gas molecules, i.e. $L \ll l$. Under such a regime, the gas thermal conductivity is linearly dependent on pressure [45]. In practice, layers of superinsulation materials, usually aluminized mylar, are placed into the vacuum jacket to reduce L. Moreover, an activated charcoal getter is also placed inside the vacuum jacket to absorb residual gas at low temperatures. For practical use, the vacuum jacket of the Gemini Dewar is evacuated to $\sim 10^{-6}$ mbar and the Helium leak rate tested by a leak detector is $\sim 10^{-10}\text{mbar} \cdot \text{L/s}$. The superinsulation layers also attenuate the radiation from the ~ 300 K outer wall to the ~ 4 K inner wall. It can be shown that the final heat transfer to the inner wall is reduced by a factor of $n + 1$ where n is the number of radiation shields used. To reduce heat leak through the Dewar neck, the neck of our Dewar is made of G-10 fibreglass that has lower thermal conductivity than Al or stainless steel at low temperatures as well as provides good structural support. The Dewar boil rate also strongly depends on the Helium gas venting configurations. Allowing neck venting only, where the helium gas exits the Dewar through the Dewar's neck, significantly decreases LHe boil-off rate since the residual heat leak through the neck is absorbed by the enthalpy of the cold Helium gas. The minimum boil rate achieved at Oxford is $\sim$10 L/day, as shown in Fig. 3.12 for a 120 L 14 T magnet Dewar, which gives us an operation time of around a week.

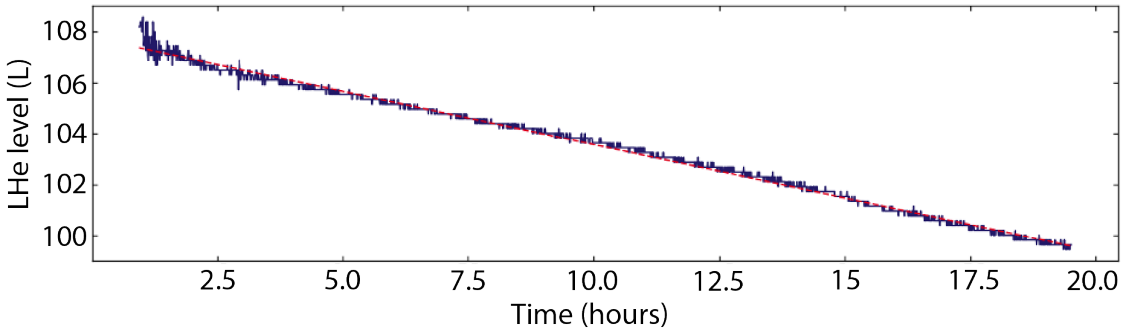

Figure 3.12: The Dewar liquid helium level over about 20 hours. The red dashed line shows a linear fit whose slope indicates a boil rate of 10.02 L/day.

3.5.2 Superconducting magnet

A 14 Tesla superconducting magnet, manufactured by American Magnetics, Inc. (AMI), sits at the bottom of the Dewar's belly. It has a 5.3 cm concentric bore to fit the STM head and the sample with a homogenous magnetic field (+/-0.1% over 1 cm DSV). The superconducting magnet coil is in a completely closed circuit in the persistent mode. To energize the magnet, a persistent switch needs to be turned on. The switch consists of a short superconducting wire thermally coupled to a resistive heater. When the heater is on, it turns the superconducting wire into its normal state so that the closed superconducting magnet circuit is open and the persistent mode is exited. An external power supply can then be connected to the magnet via two removable current leads to ramp up or down the current. After the target field is reached, the heater is then turned off and the magnet goes back to persistent mode again, where the magnetic field persists. During persistent mode, the two current leads are removed to reduce heat leak to the LHe reservoir and thus the LHe boil rate.

3.5.3 Cooling to 4 Kelvin

The cooling process of the refrigerator involves multiple stages and is designed to reach temperatures as low as tens of millikelvin (mK). The initial stage operates at the temperature of LHe, i.e. 4.2 K. This temperature is achieved by creating a

[1]Unless otherwise specified, all Helium mentioned in the text refers to ^{4}He.

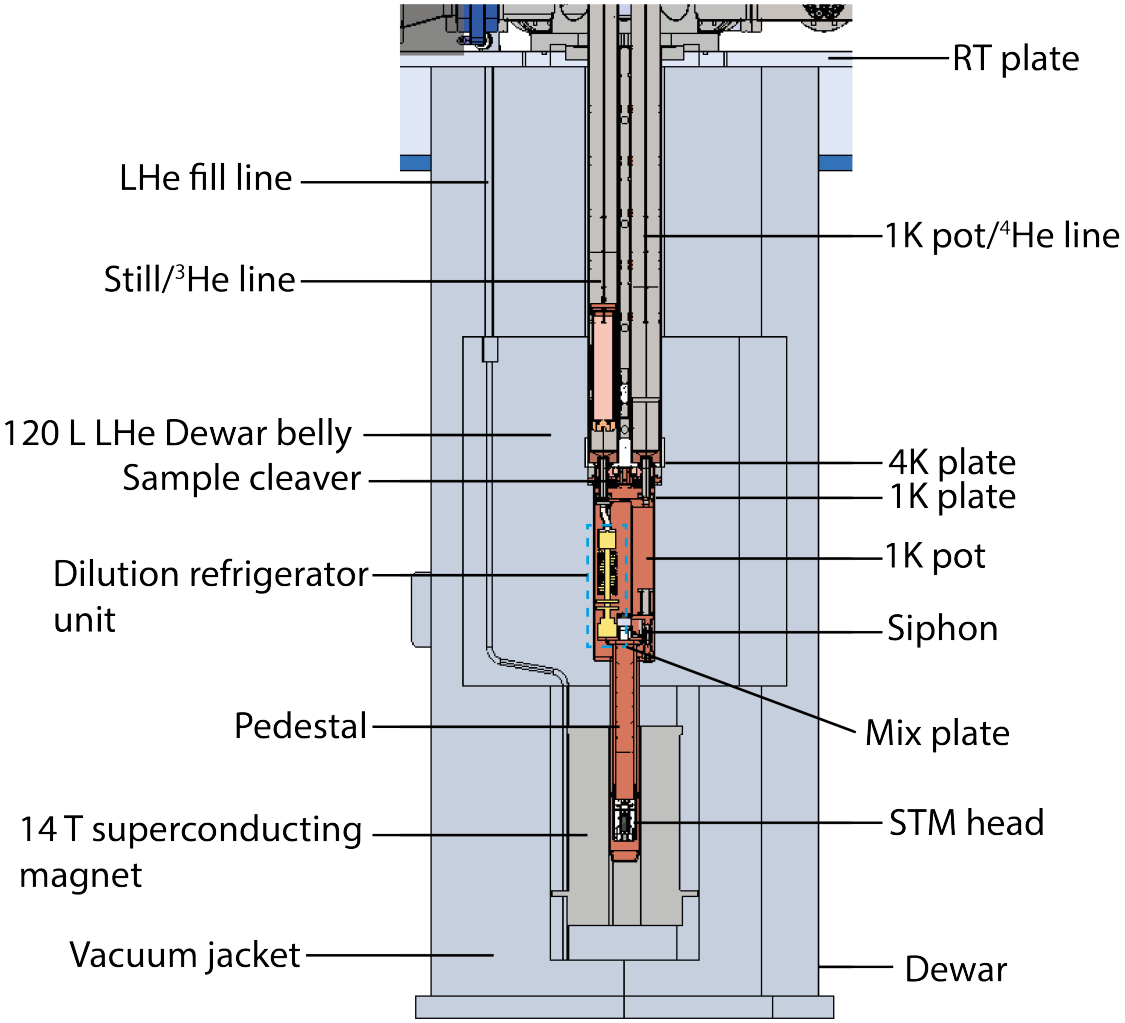

Figure 3.13: CAD section view of Gemini cryogenic system.

direct thermal connection between the cryostat inside the vacuum and the Dewar LHe bath through a vacuum flange connected to the 4-kelvin plate (4KP) (Fig. 3.14). It is important to have 4KP reach 4 K as it not only condenses the ^{3}He gas in the ^{3}He/dilution fridge but also pre-cools components such as coaxial cables and pumping tubes before the heat reaches the lower temperature region below. The strategy is to maximise the thermal conductivity to the LHe bath from the 4KP and simultaneously minimise the heat leak of the parts coming from above. To achieve the first condition, the thermal link is a vacuum flange made of high-purity copper so that its thermal conductivity is extremely high ($> 10^4$ W/(m $\cdot$ K) at 4 K). Various methods are employed to achieve the second condition. The room-temperature

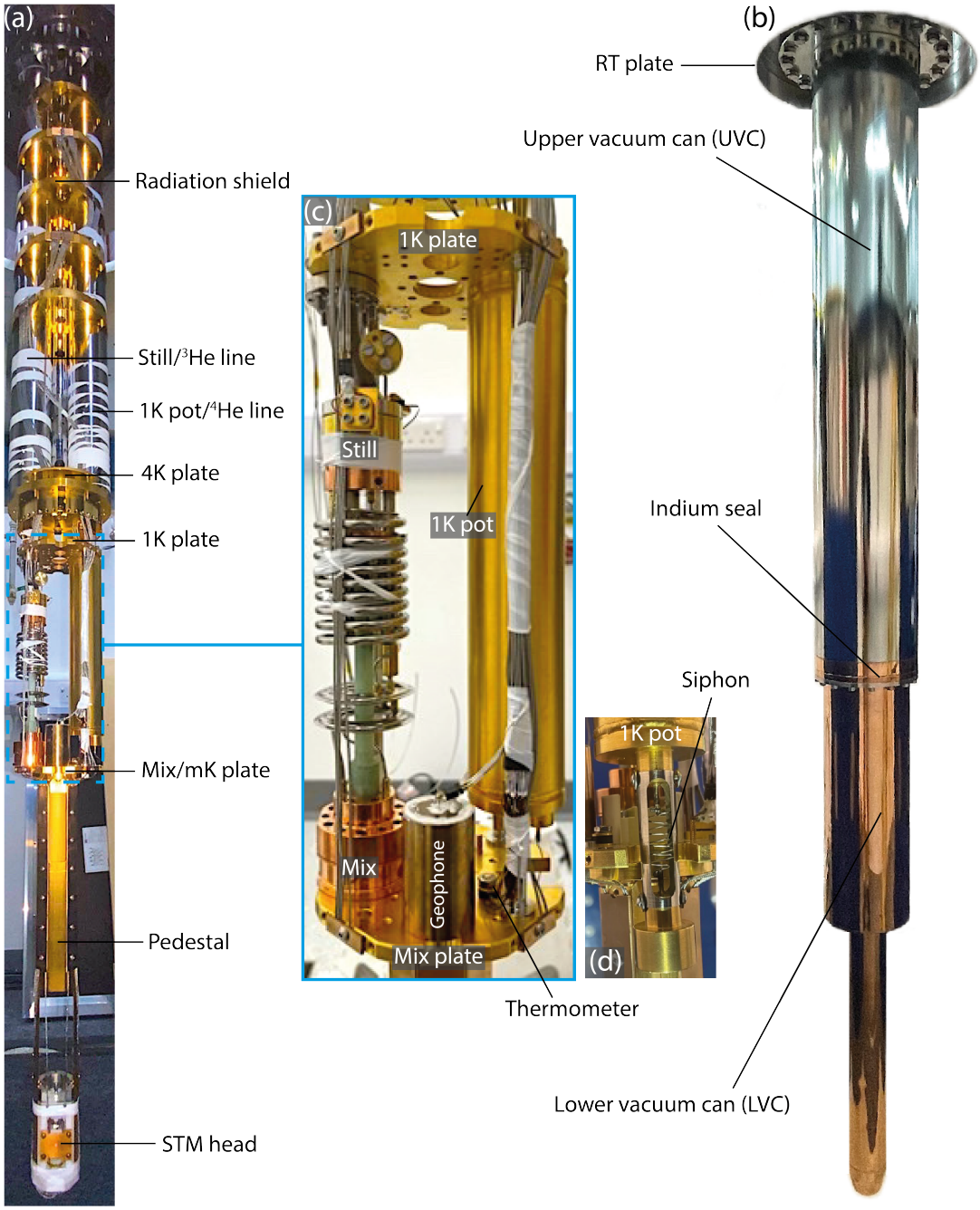

Figure 3.14: (a) Photograph of the cryogenic insert from the room-temperature (RT) plate to the STM head. (b) Photograph of the cryogenic insert sealed with the vacuum cans. The indicated Indium seal is at the position of the 4K plate in (a). (c) Zoomed-in view for the dilution unit and the 1K pot. (d) Zoomed-in view for the 1K pot NbTi siphon that provides LHe flow impedance. The siphon bottom is soldered to a Cu stud that is indium-sealed to the lower vacuum can.

(RT) thermal radiation is attenuated through 5 copper shields above the 4KP. All rigid components from the room temperature linked to 4KP are made of stainless steel, a material known for its low thermal conductivity at low temperatures ($<$ 1 W/m $\cdot$ K below 10 K). For example, the heat conduction through the helium gas pumping tubes is sunk into the Dewar LHe bath through the copper radiation shields. Eventually, the estimated heat leak from the cryostat into the LHe bath should be kept under 250 mW, corresponding to a boil-off rate of less than 10 L/day.

3.5.4 Cooling to 1 Kelvin

The physical principle to achieving near 1 Kelvin temperature is evaporation, wherein a vacuum pump evacuates the space above LHe. Rather than pumping the entire Dewar helium bath, which significantly accelerates LHe boil-off, a more economically efficient method involves using a separate, small container with a volume of several cm^3. This container, known as a '1K pot', is placed inside the vacuum system, and when it is pumped, it cools the experiment to a lower temperature. The 1K pot is connected to the main LHe bath through a thin capillary siphon with a fraction of a millimetre diameter. The liquid in the main bath is at atmospheric pressure and can then flow into the evaporation pot due to the pressure difference. The liquid level h inside the pot is determined by the balance between the heat transferred from the main bath liquid, the heat load from the experiment, and the pot evaporation cooling power. This condition reads [46]:

$$\dot{Q}_{\text{evaporation}} = \dot{Q}_{\text{siphon}}\,(h) + \dot{Q}_{\text{ext}}\,. \tag{3.4}$$

$\dot{Q}_{\text{siphon}}$ is determined by the siphon impedance which controls the LHe volumetric flow. If the impedance is too high, the pot risks running dry and escalating in temperature because of external heat leaks. Conversely, if the impedance falls too low, the liquid level within the pot could become excessively high, overwhelming the cooling power from evaporation. $\dot{Q}_{\text{evaporation}}$ is controlled by the pumping speed of the vacuum pump. The pressure-temperature ($P-T$) relation satisfies

the Clausius-Clapeyron formula:

$$\begin{aligned} \frac{dP}{dt} &= \frac{L}{R}\frac{P}{T^2} \\ \Rightarrow P &\propto e^{-\frac{L}{RT}} \end{aligned} \tag{3.5}$$

where L is the helium latent heat of vaporisation and R is the specific gas constant. This relation suggests that to achieve a lower temperature, it is necessary to minimise the vapour pressure as much as possible. Usually, this is achieved by using a pump with a large pumping speed. Under continuous operation, the 1K pot temperature normally remains around 1.3 K. Eventually, the temperature cannot be lowered further because the vapour pressure is too small. Common problems for 1 K pot operation include siphon blockage and vibrational noise. The fine capillary siphon is easily blocked by impurities in the LHe bath, such as N_2 ice, but can be prevented by installing a filter at its front to keep flowing LHe clean. The vibration noise can come from the ultra-sonic 'jet' when the normal LHe is injected into the superfluid He. This can be solved by thermalising the capillary siphon or adjusting its impedance.

3.5.5 Cooling to milli-Kelvin

A dilution refrigerator must be employed to access the tens of milli-Kelvin range. The dilution refrigerator utilizes the mixing of two helium isotopes, ^{3}He and ^{4}He, to achieve ultra-low temperatures. Its operating principle is as follows. A ^{3}He-^{4}He mixture is pre-cooled to 4.2 K at the 4KP and then down to around 1.3 K by the 1K pot. The mixture then continues to be condensed and cooled through a series of small-volume heat exchangers anchored to the still pot (Fig. 3.15). Finally, the condensed mixture arrives at the mixing chamber, where the temperature reaches the phase separation boundary. At this point, the helium mixture separates into two phases, one ^{4}He-rich (^{3}He-dilute) phase and the other ^{3}He-rich phase. The ^{3}He-rich part floats on top because of its lower density. The surprising feature of the phase-separated mixture is that the concentration of the ^{3}He inside the ^{4}He-rich liquid is still finite (about 6.6%) as the temperature approaches zero. This may seem a violation of the third law of thermodynamics in the classical regime. But despite non-zero mixing, the mixture has zero entropy at $T = 0$ K because of the

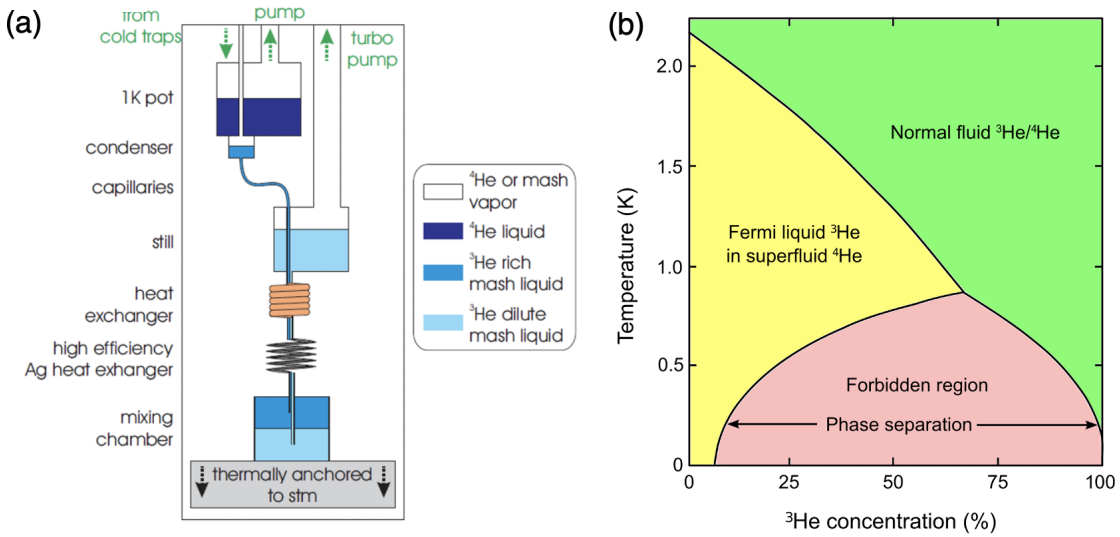

Figure 3.15: (a) Schematic of the working principle of the dilution fridge. (b) ^{3}He – ^{4}He mixture phase diagram. Photo reproduced from [47].

quantum nature of the liquid, i.e. superfluid. As the ^{3}He vapour pressure is lowered in the Still chamber, an osmatic pressure is established across the two phases in the mixing chamber that drives the ^{3}He atoms to the ^{4}He - rich liquid. This is the process that generates cooling in the dilution refrigerator.

To calculate the cooling power in the mixing chamber, consider ^{3}He atoms in the ^{3}He-rich and dilute phases separately. Since ^{3}He atoms are fermions, the Fermi temperatures for ^{3}He atoms in both phases are given by

$$^3\text{He rich phase: } k_B T_F^R = \frac{\hbar^2}{2m_3}\left(3\pi^2 \frac{N_R}{V}\right)^{\frac{2}{3}} \tag{2.2.5.3a}$$

$$^3\text{He dilute phase: } k_B T_F^D = \frac{\hbar^2}{2m_3}\left(3\pi^2 \frac{N_D}{V}\right)^{\frac{2}{3}} \tag{2.2.5.3b}$$

where the particle number density has the relation $\frac{N_D}{V} \propto (0.06)\frac{N_R}{V}$. As a result, the entropy in the ^{3}He dilute phase is larger than that in the ^{3}He rich phase

$$S_R = \frac{\pi^2}{2} N k_B \frac{T}{T_F^R} < S_D = \frac{\pi^2}{2} N k_B \frac{T}{T_F^D} \tag{3.6}$$

which results in the 'evaporation' of ^{3}He atoms from its rich phase to the dilute phase that gives the cooling. Given a ^{3}He evaporation rate of n_3 moles/s, the specific entropy for both phases is $s_R = \frac{\pi^2}{2} N_A n_3 k_B \frac{T}{T_F^R}, s_D = \frac{\pi^2}{2} N_A n_3 k_B \frac{T}{T_F^D}$. The

cooling power of the ^{3}He dilution process is given by

$$\begin{aligned} \dot{Q} &= T_M^2 \dot{n}_3 \frac{\pi^2}{2} k_B N_A \left(\frac{1}{T_F^D} - \frac{1}{T_F^R} \right) \\ \Rightarrow \dot{Q} &\approx (95) \dot{n}_3 T_M^2 \quad [\mathrm{W}] \end{aligned} \tag{3.7}$$

where T_M is the mixing chamber temperature and N_A the Avogadro number. Given the base temperature of around 15 mK and pumping speed of 4.45×10^{-5}moles/s in the Still chamber, the estimated cooling power is about 1 μW.

Part of this chapter appears as:

Proc. Nat'l Acad. Sci. ***119****, 2206481119 (2022)*

— Wangping Ren *at al.*

4

Discovery of a nematic pair density wave state in $Bi_2Sr_2CaCu_2O_{8+x}$

Contents

In this chapter, I will present the discovery of a nematic PDW state in $Bi_2Sr_2CaCu_2O_{8+x}$ by extensive analysis of the scanned Josephson tunnelling data collected by SJTM[1]. The spatial configurations of the discovered PDW state have domains of opposite nematicity, each of which is primarily unidirectional and lattice commensurate. Simultaneous visualisation of the amplitudes reveals that the intertwined PDW and $d-wave$ superconductivity (dSC) are mutually attractive states. Furthermore, imaging the scattering resonances identifies the Zn impurity atoms at the boundaries between the domains, indicating that the Zn

[1]The data analysis presented in this chapter was performed using MATLAB. M. H. Hamidian at Cornell University carried out the SJTM measurements.

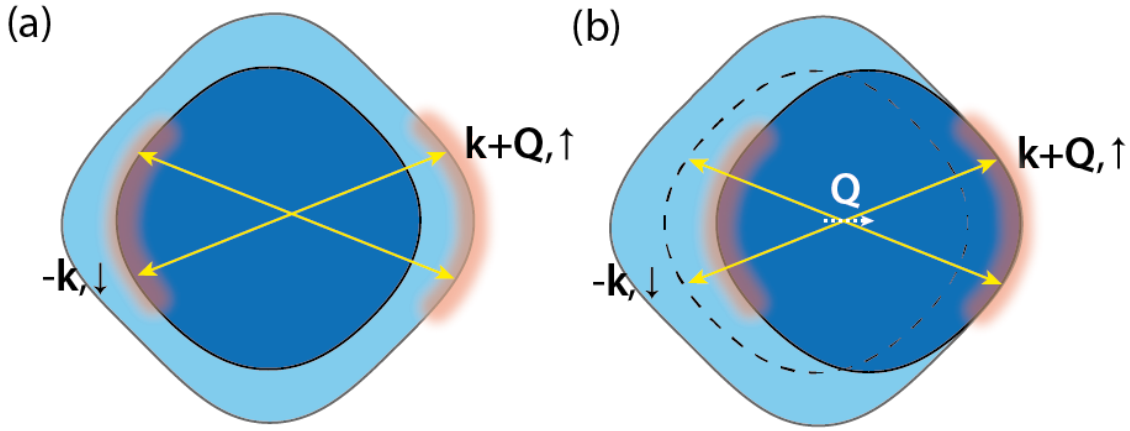

Figure 4.1: Schematic of finite momentum pairing at wavevector **Q**. (a) The original Fermi surface is split into up and down spin Fermi surfaces due to the Zeeman effect. Pairing only occurs in the red shaded regions (gapped out) between electrons in state $|-\mathbf{k},\downarrow\rangle$ and state $|\mathbf{k}+\mathbf{Q},\uparrow\rangle$. This leaves a large unpaired region (gapless) on the Fermi surface, which gives finite spin susceptibility. (b) Pairing can be perceived as shifting the down spin Fermi surface with wavevector **Q**. The nested regions indicate pairing with centre-of-mass momentum **Q**. The origin is at the centre of the spin-up Fermi surface.

atoms pin this nematic PDW state.

Exotic superconducting states such as the pair-density wave (PDW) state with finite momentum pairing have been shown to exist in the cuprates [33], but their mechanism remains unknown. The interplay between the homogeneous *d*-wave superconductivity (dSC) and PDW is hypothesized to generate a variety of global electron-pair orders, but it is not clear which one is present [11, 48, 49]. SJTM is an ideal technique for studying the intertwined orders between dSC and PDW in cuprates since it gives direct access to the superconducting order parameter.

4.1 FFLO state

In 1964, Flulde, Ferrell, Larkin, and Ovchinnikov (FFLO) proposed a novel state where superconductivity persists beyond the upper critical field H_{c2} but with a finite centre-of-mass momentum **Q** in the Cooper pair condensate. This is because of the electron pairing between two split Fermi surfaces due to the Zeeman effect (Pauli paramagnetism) as shown in Fig. 4.1. However, in the superconducting state, the condensed Cooper pairs have zero total spin susceptibility, $\chi_{s,\text{total}} = 0$, and are

not spin polarized by the magnetic field H. Thus, to polarize the Cooper pairs, the spin polarization energy should reach the superconducting condensation energy [50]:

$$\frac{1}{2}\left(\chi_n - \chi_s\right) H^2 = \frac{H_c^2(T)}{8\pi} \tag{4.1}$$

where χ_n is the spin susceptibility at the normal state, H_c is the critical field. A critical field $H = H_P$ can then be identified as the pair-breaking limit due to Pauli paramagnetism only:

$$H_P(T) = \frac{H_c(T)}{\sqrt{4\pi\left(\chi_n - \chi_s\right)}}. \tag{4.2}$$

This is the Pauli-limited critical field. At $T = 0$, we have

$$H_P(0) = \frac{\sqrt{2}\Delta}{g\mu_B} \tag{4.3}$$

where the relation $\frac{H_c^2(0)}{8\pi} = \frac{N(0)\Delta^2}{2}$ is used and g is the electron spectroscopic splitting factor ($g = 2$). In addition, the formation of vortices can also break Cooper pairs and destroy superconductivity with upper critical field $H_{c2}^{\mathrm{orb}} = \Phi_0/2\pi\xi^2$ where ξ is the coherence length and Φ_0 is the flux quantum. This is the orbital limited pair-breaking effect. In a type II superconductor, the phase transition at H_{c2}^{orb} is of the second order. In the presence of the paramagnetic effect only, it has been shown by [51] that the transition to the normal state can be of the first order. In general, it is the competition between the paramagnetic pair-breaking effect and the orbital pair-breaking effect that determines the upper critical field and the order of the phase transition. This is quantified by the Maki parameter:

$$\alpha = \sqrt{2}\frac{H_{c2}^{\mathrm{orb}}(0)}{H_P(0)}. \tag{4.4}$$

For the first-order phase transition, high α is needed. Flulde and Ferrell [52] proposed that the Pauli-limited critical field can be further extended by transitioning into an inhomogeneous superconducting state with finite momentum pairing between the split Fermi surfaces. This is called the FF state. In general, for a FF state to persist in a clean type II superconductor, $\alpha > 1.8$ needs to be satisfied [53].

The general superconducting order parameter can be written in a spatially dependent form [48]

$$\Delta(\mathbf{r}) = V_0 \left\langle \hat{\psi}_\downarrow(\mathbf{r})\hat{\psi}_\uparrow(\mathbf{r}') \right\rangle \tag{4.5}$$

$$= V_0 F(\mathbf{r}-\mathbf{r}') \left[\Delta_0 + \Delta_{\mathbf{Q}} e^{i\mathbf{Q}\cdot\mathbf{R}} + \Delta_{-\mathbf{Q}} e^{-i\mathbf{Q}\cdot\mathbf{R}}\right] \tag{4.6}$$

where F is the form factor and $\mathbf{R}$ is the centre-of-mass momentum. In BCS theory, the electron-pair condensate is homogeneous, i.e. $\Delta(\mathbf{r}) = \Delta, \Delta_{\boldsymbol{Q}} = 0, \Delta_{-\boldsymbol{Q}} = 0$. This is in contrast with the FF state, where the superconducting order parameter is given by

$$\Delta(\mathbf{r}) = \Delta_{\mathbf{Q}} e^{i\mathbf{Q}\cdot\mathbf{r}} \tag{4.7}$$

in which the pairing amplitude $\Delta_{\mathbf{Q}} = \Delta$ is constant but the phase modulates in space with period $2\pi/Q$. This state only modulates in $+\mathbf{Q}$ direction, and the time-reversal symmetry is thus broken. Larkin and Ovchinnikov [54] considered another inhomogeneous state consisting of two opposite wavevectors where the time-reversal symmetry is preserved, i.e. the LO state. The order parameter has the form

$$\Delta(\mathbf{r}) = \Delta\left(e^{i\mathbf{Q}\cdot\mathbf{r}} + e^{-i\mathbf{Q}\cdot\mathbf{r}}\right) = 2\Delta\cos(\mathbf{Q}\cdot\mathbf{r}). \tag{4.8}$$

Here, the pairing amplitude modulates in space but with fixed phase which suggests a modulated electron-pair density $|\Delta|^2$. The LO state has lower free energy than the FF state [51].

4.2 Pair-density waves in the cuprates

The FFLO states are a subset of the pair-density wave (PDW) states that have finite momentum pairing. In some cases, the magnetic field is not necessary to induce a PDW state. For example, in the cuprates, the symmetry of the square CuO_2 plane allows four components of the PDW order parameter, i.e. $\Delta_i = \left(\Delta_{\boldsymbol{P}_x}, \Delta_{\boldsymbol{P}_y}, \Delta_{-\boldsymbol{P}_x}, \Delta_{-\boldsymbol{P}_y}\right)$. The general Ginzberg-Landau-Wilson (GLW)

Table 4.1: Possible PDW ground states. Table reproduced from [49].

Phase	$\left(\Delta_{\mathbf{P}_x}, \Delta_{\mathbf{P}_y}, \Delta_{-\mathbf{P}_x}, \Delta_{-\mathbf{P}_y}\right)$	Induced orders
FF-type	$\left(e^{i\phi_1}, 0, 0, 0\right)$	$l_x, \epsilon_{x^2-y^2}$
FF*-type	$\left(e^{i\phi_1}, e^{i\phi_2}, 0, 0\right)$	$l_x = l_y$ $\rho_{\mathbf{P}_x-\mathbf{P}_y}, M^z_{\mathbf{P}_x-\mathbf{P}_y}$
Unidirectional	$\left(e^{i\phi_1}, 0, e^{i\phi_2}, 0\right)$	$\epsilon_{x^2-y^2}, \Delta_{4e}$ $\rho_{2\mathbf{P}_x}$
Bidirectional-I	$\left(e^{i\phi_1}, e^{i\phi_2}, e^{i\phi_3}, e^{i[\phi_1+\phi_3-\phi_2]}\right)$	Δ_{4e} $\rho_{2\mathbf{P}_x}, \rho_{2\mathbf{P}_y}, \rho_{\mathbf{P}_x-\mathbf{P}_y}, \rho_{\mathbf{P}_x+\mathbf{P}_y}$
Bidirectional-II	$\left(e^{i\phi_1}, ie^{i\phi_2}, e^{i\phi_3}, ie^{i[\phi_1+\phi_3-\phi_2]}\right)$	Δ_{4e} $\rho_{2\mathbf{P}_x}, \rho_{2\mathbf{P}_y} M^z_{\mathbf{P}_x-\mathbf{P}_y}, M^z_{\mathbf{P}_x+\mathbf{P}_y}$

free energy density that preserves time-reversal, parity and gauge symmetries can be written as [49]

$$\begin{aligned}\mathcal{F} = \alpha \sum_i |\Delta_{P_i}|^2 + \beta_1 \left(\sum_i |\Delta_{P_i}|^2\right)^2 + \beta_2 \sum_{i<j} |\Delta_{P_i}|^2 \left|\Delta_{P_j}\right|^2 + \beta_3 \left(|\Delta_{P_x}|^2 |\Delta_{-P_x}|^2 \right. \\ \left. + \left|\Delta_{P_y}\right|^2 \left|\Delta_{-P_y}\right|^2\right) + \beta_4 \left[\Delta_{P_x}\Delta_{-P_x}\left(\Delta_{P_y}\Delta_{-P_y}\right)^* + \left(\Delta_{P_x}\Delta_{-P_x}\right)^* \Delta_{P_y}\Delta_{-P_y}\right],\end{aligned} \tag{4.9}$$

which allows the five possible PDW ground states as summarised in Table 4.1. The difference between the Bidirectional-I and the Bidirectional-II phase is that the phase difference between the two modulation directions is 0 for the former case and $\pi/2$ for the latter case. Including the homogeneous superconducting order parameter (dSC) Δ_0, there are then five possible complex-valued scalar order parameters that are intertwined together, generating a plethora of induced order parameters.

4.2.1 Coupling between dSC and PDW

The coupling between the dSC order and the PDW order can be described by a subset of the overall GLW free energy density functional to the lowest order of coupling terms, namely,

$$\begin{aligned}\mathcal{F} = \beta_{c_1} |\Delta_0|^2 \left(|\Delta_{P_x}|^2 + \left|\Delta_{P_y}\right|^2 + |\Delta_{-P_x}|^2 + \left|\Delta_{-P_y}\right|^2\right) \\ + \beta_{c_2} \left[\Delta_0^2 \left(\Delta_{P_x}\Delta_{-P_x} + \Delta_{P_y}\Delta_{-P_y}\right)^* + \left(\Delta_0^2\right)^* \left(\Delta_{P_x}\Delta_{-P_x} + \Delta_{P_y}\Delta_{-P_y}\right)\right],\end{aligned} \tag{4.10}$$

where the gradient terms are ignored. An interesting hypothetical state that arises from the interplay between dSC and PDW is the nematic pair density wave state

with the order parameter defined as

$$N \equiv \left(|\Delta_{P_x}|^2 + |\Delta_{-P_x}|^2\right) - \left(\left|\Delta_{P_y}\right|^2 + \left|\Delta_{-P_y}\right|^2\right). \tag{4.11}$$

The experimental goal is then to determine how dSC and PDW are intertwined and search for the consequent electron-pair order.

4.3 Visualising nematicity of a pair-density wave state

To image the nematic order of a PDW state, a dilution-refrigerator-based SJTM is used to directly measure the superconducting order parameter in lightly underdoped single crystals of $Bi_2Sr_2CaCu_2O_{8+x}$ (Bi-2212) (hole density $p = 0.17$) at 45 mK. The sample is cryogenically cleaved to reveal the BiO crystal layer. Under the regime of phase-diffusive Josephson tunnelling (I-Z model), the maximum value of the pair tunnelling current I_m is proportional to the electron-pair density via

$$n(\mathbf{r}) \propto I_m(\mathbf{r}) R_N^2(\mathbf{r}) \tag{4.12}$$

where the normal state junction resistance $R_N(\mathbf{r}) \approx 20$ MΩ [33]. The *d*-wave scanning tip is prepared by picking up a $Bi_2Sr_2CaCu_2O_{8+x}$ nano-flake from the sample. A typical topographic image of the BiO layer scanned by the $Bi_2Sr_2CaCu_2O_{8+x}$ tip is shown in Fig. 4.2(a) with the inset showing a typical measured $I - V$ characteristics. With virtually constant $R_N(\mathbf{r})$, we can measure $I_P(V, \mathbf{r})$ and therefore visualise $I_m(\mathbf{r})$ at 45 mK. The Fourier transform of $I_m(\mathbf{r})$ image, $I_m(\mathbf{q})$, is shown in Fig. 4.2(b). Besides the broad peak centred around $\mathbf{q} = \frac{2\pi}{a}(0,0)$ that represents the heterogeneous dSC state, there are four broad peaks centred around $\mathbf{q} \approx \frac{2\pi}{a}\left(0, \pm\frac{1}{4}\right); \frac{2\pi}{a}\left(\pm\frac{1}{4}, 0\right)$.

4.3.1 Visualising the interplay between dSC and PDW

By analysing the relationships among the five wavevectors in $I_m(\mathbf{q})$ in real space, i.e $I_{m,i} = \left\{I_{m,\mathbf{q}=\frac{2\pi}{a}(0,0)}(\mathbf{r}), I_{m,\mathbf{q}=\frac{2\pi}{a}\left(0,\pm\frac{1}{4}\right)}(\mathbf{r}), I_{m,\mathbf{q}=\frac{2\pi}{a}\left(\pm\frac{1}{4},0\right)}(\mathbf{r})\right\}$, the interplay of the five order parameters $\left(\Delta_0, \Delta_{\boldsymbol{P_x}}, \Delta_{\boldsymbol{P_y}}\Delta_{\boldsymbol{-P_x}}, \Delta_{\boldsymbol{-P_y}}\right)$ can then be detected.

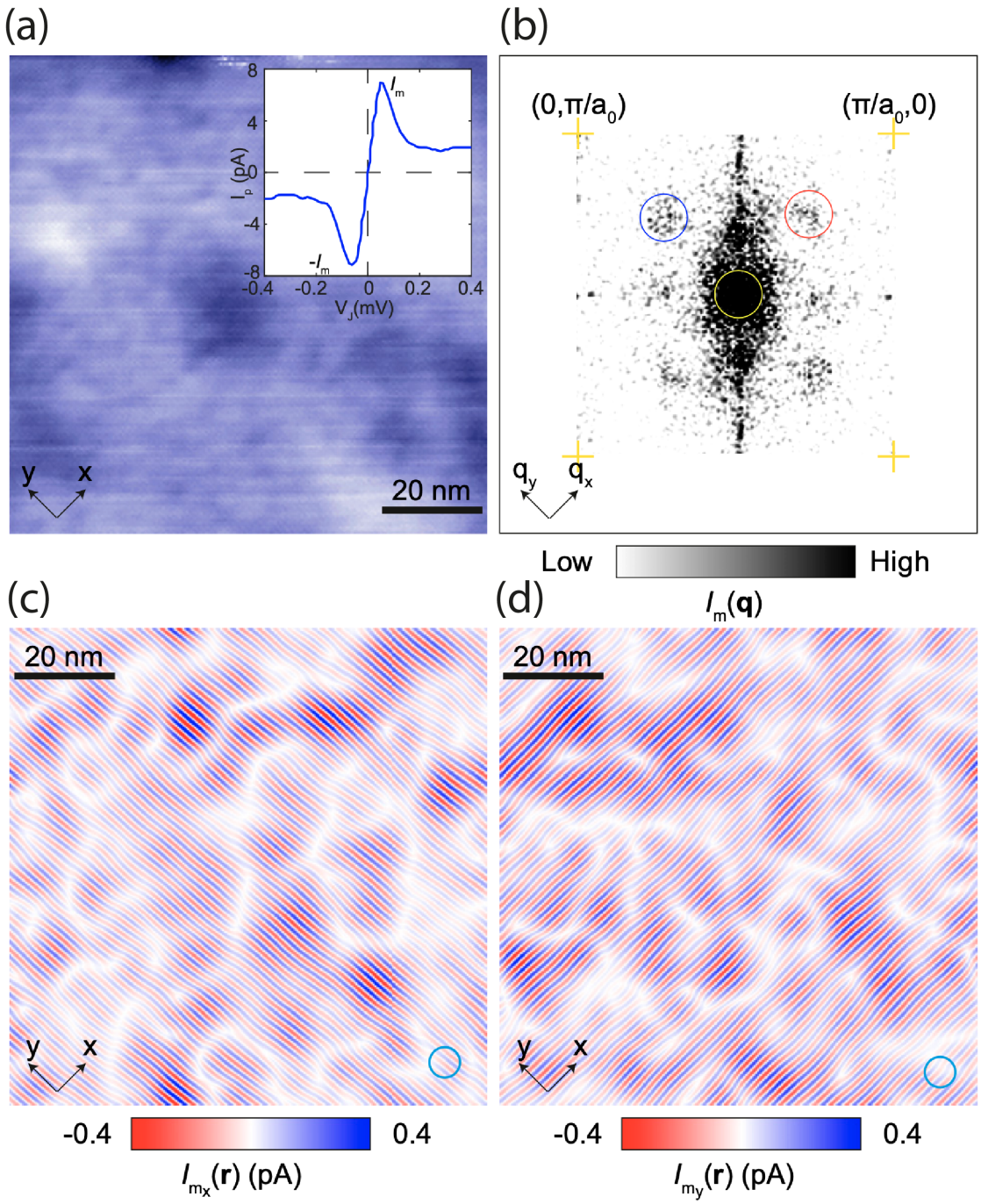

Figure 4.2: Visualising electron-pair density $n(\mathbf{r})$. (a) SJTM topographic image $T(\mathbf{r})$ of BiO termination layer of $Bi_2Sr_2CaCu_2O_{8+x}$. Inset: average electron-pair current spectrum $I_P\,(V_J)$ measured in this FOV at $T = 45$ mK and $R_N \approx 20$ MOhm, with maxima occurring at $\pm I_m$. (b) Power spectral density Fourier transform of $I_m(\mathbf{r}), I_m(\mathbf{q})$, as measured in FOV of (a). Four broad PDW peaks surround the wavevectors $\mathbf{P} = (2\pi/a)(0, \pm 0.25); (2\pi/a)(\pm 0.25, 0)$ as indicated by pairs of red and blue circles respectively. The dSC electron-pair density is represented by the broad peak at $\mathbf{q} = (2\pi/a)(0, 0)$ as indicated by the yellow circle. (c) Fourier filtration of $I_m(\mathbf{q})$ $\mathbf{P} = (2\pi/a)(0, \pm 0.25)$ as in (b), to visualise the $\pm\mathbf{P_x}$ PDW modulating along the CuO_2 x axis. (d) Fourier filtration of $I_m(\mathbf{q})$ $\mathbf{P} = (2\pi/a)(\pm 0.25, 0)$ in (b), to visualize the $\pm\mathbf{P_y}$ PDW modulating along the CuO_2 y axis.

The two orthogonal PDWs can be parametrised as

$$\begin{aligned} I_{m;x,y}(\mathbf{r}) &= A_{x,y}(\mathbf{r}) \cos\left[\mathbf{P}_{x,y} \cdot \mathbf{r} + \delta_{x,y}(\mathbf{r})\right] \\ &\equiv A_{x,y}(\mathbf{r}) \cos\left[\Phi_{x,y}(\mathbf{r})\right] \end{aligned} \tag{4.13}$$

where $\pm\mathbf{P}_{\boldsymbol{x}} = \frac{2\pi}{a}\left(0, \pm\frac{1}{4}\right), \pm\mathbf{P}_{\boldsymbol{y}} = \frac{2\pi}{a}\left(\pm\frac{1}{4}, 0\right)$ and $\delta_{x,y}(\mathbf{r})$ is the spatially dependent phase variation. To independently analyse $I_{m;x}(\mathbf{r})$ and $I_{m;y}(\mathbf{r})$, inverse Fourier transformation of $I_m(\mathbf{q})$ centred at $\pm\mathbf{P}_{\mathbf{x}}$ and $\pm\mathbf{P}_{\boldsymbol{y}}$ respectively then gives

$$I'_m(\mathbf{r}) = \frac{1}{\sqrt{2\pi}\sigma} \int d\mathbf{r}' I_m\left(\mathbf{r}'\right) e^{-i\boldsymbol{P}_{x,y}\cdot\mathbf{r}'} e^{\frac{|\mathbf{r}-\mathbf{r}'|^2}{2\sigma^2}} \tag{4.14}$$

where $\sigma = 3$ nm represents the reciprocal space selection range as indicated in red and blue circles in Fig. 4.2(b). The resulting $I_{m;x}(\mathbf{r})$ and $I_{m;y}(\mathbf{r})$ images are shown in Fig. 4.2(c - d). The modulation amplitude of the Fourier selected PDW components can then be written as

$$A_{x,y}(\mathbf{r}) \equiv 2\sqrt{\left(\mathcal{R}eI'_m(\mathbf{r})\right)^2 + \left(\mathcal{I}mI'_m(\mathbf{r})\right)^2}. \tag{4.15}$$

The amplitude of the heterogeneous dSC state near $\mathbf{q} = \mathbf{0}, A_0(\mathbf{r})$, can be obtained using the similar inverse Fourier transform technique. We then have simultaneously measured $A_x(\mathbf{r}), A_y(\mathbf{r})$ and $A_0(\boldsymbol{r})$ as shown in Fig. 4.3(a - c) in the same field of view of Fig. 4.2(a). To quantify and relationship between the dSC and PDW states, $\langle A_x(\mathbf{r}) + A_y(\mathbf{r})\rangle$ and $\langle A_0(\mathbf{r})\rangle$ are plotted against each other where the average is taken over all positions $\mathbf{r}$. The positive slope $s = \frac{\langle A_x(r)+A_y(r)\rangle}{\langle A_0(r)\rangle} = 0.0389$ shown in Fig. 4.3(d) clearly indicates a mutually attractive relation on the average between the PDWs and the dSC states throughout the spatial variations. This result is completely independent of any spatial variations in the normal state junction resistance $R_N(\mathbf{r})$ since it's divided out in the definition of the slope s.

To understand this result in the GLW free energy framework, we must insert the full order parameter expression for each component $\Delta_i = |\Delta_i| e^{i\phi_i}$ into Eqn. 4.10, which yields

$$\begin{aligned} \mathcal{F} = 2\left|\Delta_0\right|^2 \left|\Delta_x\right|^2 &\left[\beta_{c1} + \beta_{c2}\cos\left(2\phi_0 - \phi_1 - \phi_3\right)\right] \\ &+ 2\left|\Delta_0\right|^2 \left|\Delta_y\right|^2 \left[\beta_{c1} + \beta_{c2}\cos\left(2\phi_0 - \phi_2 - \phi_4\right)\right] \end{aligned} \tag{4.16}$$

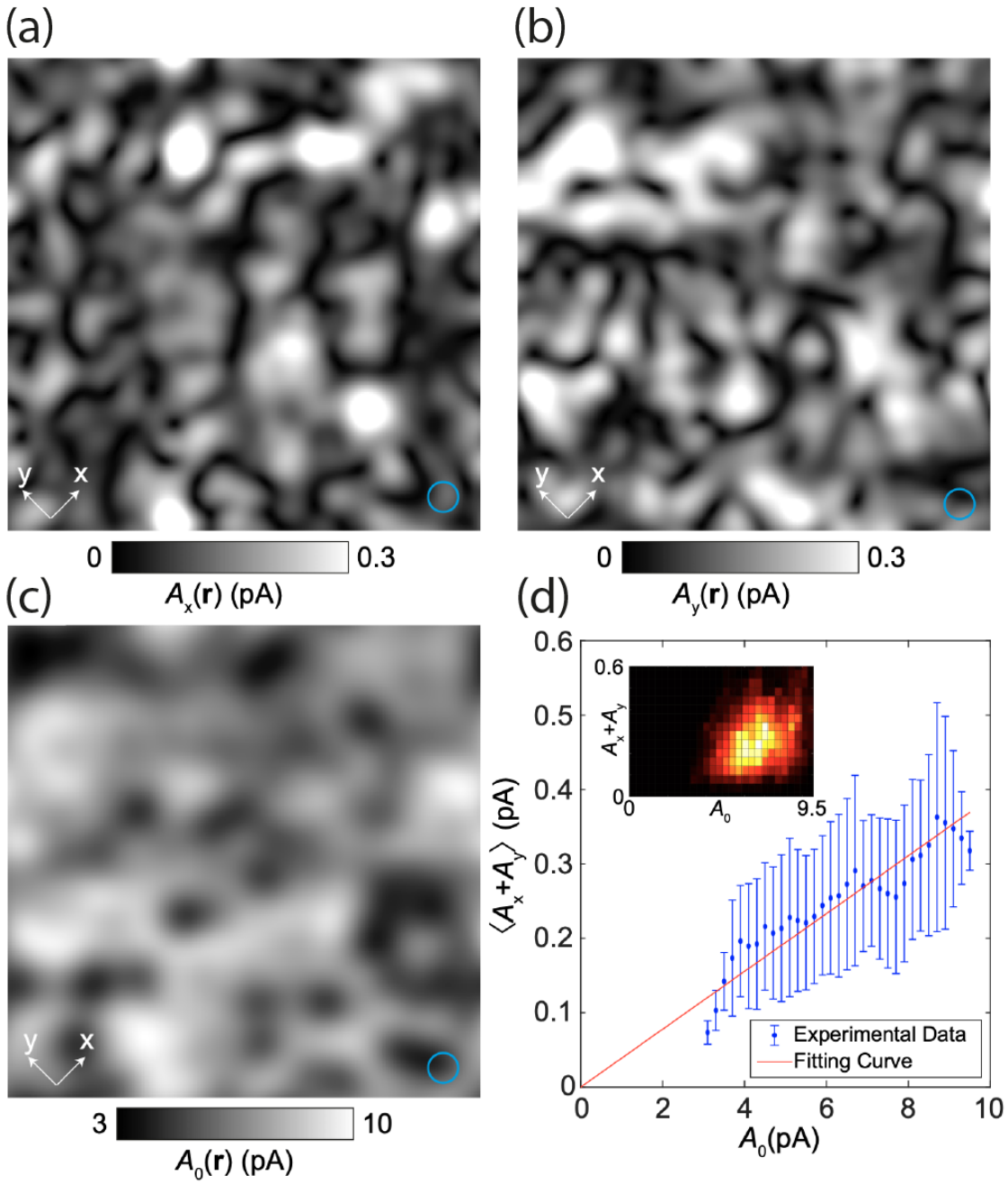

Figure 4.3: Intertwined dSC and PDW order parameters. (a) Amplitude of $I_{\rm m}(\mathbf{r})$ modulations $A_{\rm x}(\mathbf{r})$ for PDW state with $\pm \boldsymbol{P_x}$, from Fig. 4.2(c). (b) Amplitude of $I_{\rm m}(\mathbf{r})$ modulations $A_y(\mathbf{r})$ for PDW state with $\pm \boldsymbol{P_y}$, from Fig. 4.2(d). (c) Amplitude of dSC electron-pair density $A_0(\mathbf{r})$ derived from Eqn. 4.12 with $\mathbf{q} = 0$ as indicated by the yellow circle in Fig. 4.2(b). (d) $\langle A_x(\mathbf{r}) + A_y(\mathbf{r}) \rangle$ averaged over all locations $\mathbf{r}$ where $A_0(\mathbf{r})$ equals the abscissa value A_0. The solid line is a linear fit to these data through $(0, 0)$. Inset: 2D histogram of the same data.

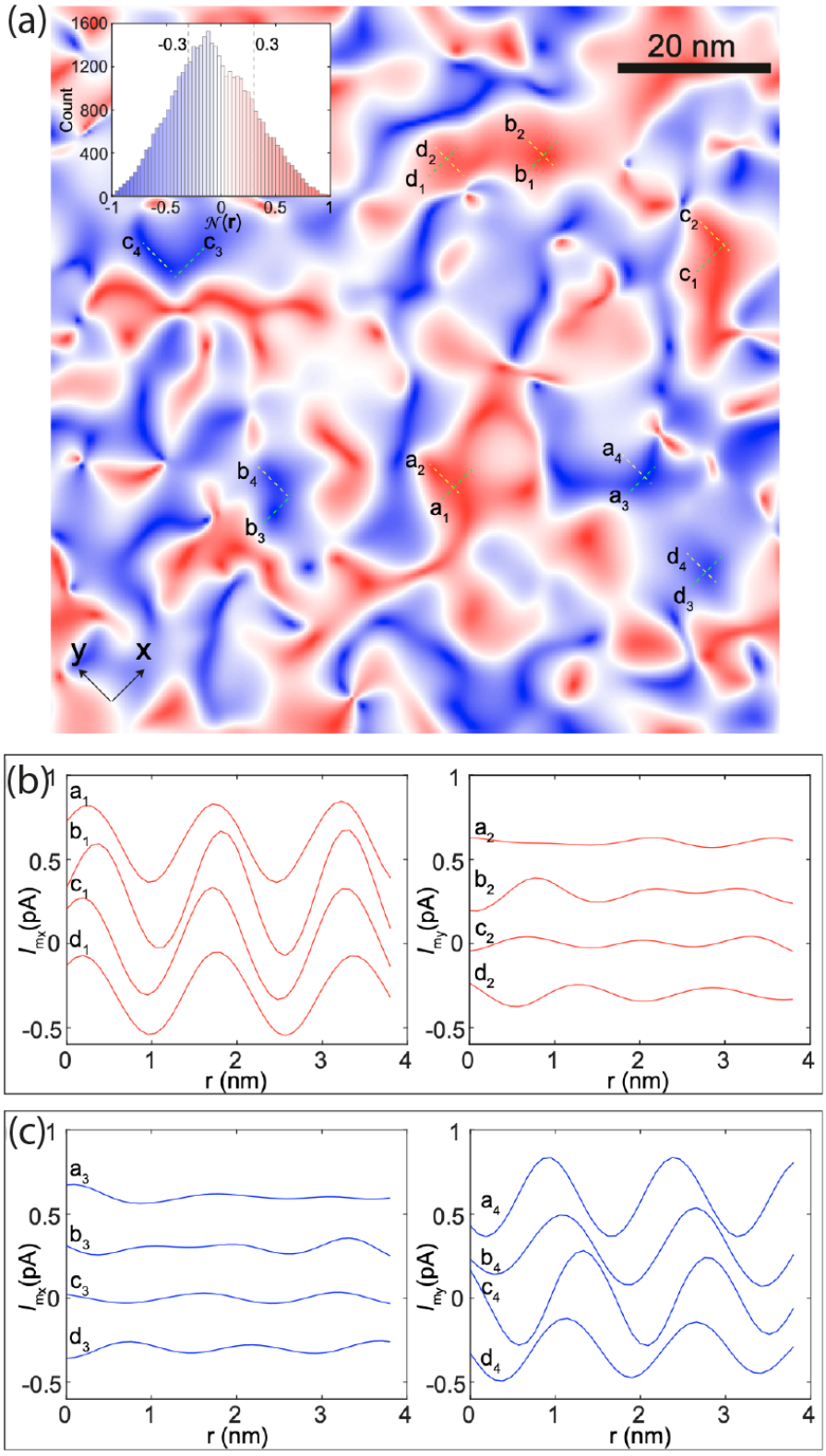

Figure 4.4: (a) Nematic order parameter $\mathcal{N}(\mathbf{r}) = \{A_x(\mathbf{r}) - A_y(\mathbf{r})\} / \{A_x(\mathbf{r}) + A_y(\mathbf{r})\}$ derived from Fig. 4.3 (a) and (b). Domains of opposite nematicity occur with correlation length $\xi \approx 15$ nm. Inset: histogram of all $\mathcal{N}(\mathbf{r})$ values in (a), showing nonzero mean value. The magnitude $|\mathcal{N}| > 0.3$ for approximately 45% of the FOV indicates a strong nematic interaction between the two PDW. (b, Left) Four examples of measured $I_{\mathrm{m}}(\mathbf{r})$ along the x axis. (b, Right) Four examples of measured $I_m(\mathbf{r})$ along the y axis, both within domains where $\mathcal{N}(\mathbf{r}) \gg 0$. (c, Left) Four examples of measured $I_{\mathrm{m}}(\mathbf{r})$ along the x axis. (c, Right) Four examples of measured $I_{\mathrm{m}}(\mathbf{r})$ along the y axis, both within domains where $\mathcal{N}(\mathbf{r}) \ll 0$.

Here the loop current terms are neglected for simplicity. The coupling term β_{c_2} then locks the phase between the dSC and PDW orders [49]. The minimum of the free energy is then given by

$$\mathcal{F}_{\min} = 2\left|\Delta_0\right|^2\left(\left|\Delta_x\right|^2+\left|\Delta_y\right|^2\right)\left[\beta_{c1}-\left|\beta_{c2}\right|\right] \tag{4.17}$$

As a result, a positive correlation between $\left|\Delta_0\right|^2$ and $\left|\Delta_x\right|^2+\left|\Delta_y\right|^2$ indicates a relation of

$$\beta_{c1}-\left|\beta_{c2}\right|<0 \tag{4.18}$$

in the absence of a magnetic field, although there exists evidence showing a repulsive relation when strong gradients are present, such as in the vortex core.

4.3.2 Searching for a nematic PDW state

To search for the proposed nematic PDW phase, I start by defining an empirical nematic order parameter based directly on the measured $I_m(\mathbf{r})$ data:

$$\mathcal{N}(\mathbf{r})=\frac{A_x(\mathbf{r})-A_y(\mathbf{r})}{A_x(\mathbf{r})+A_y(\mathbf{r})} \tag{4.19}$$

where the variations in $R_N(\mathbf{r})$ is again completely irrelevant. According to the $A_x(\mathbf{r})$ and $A_y(\mathbf{r})$ data shown in Fig. 4.3, $\mathcal{N}(\mathbf{r})$ can be calculated and is shown in Fig. 4.4. Upon virtual inspection, Fig. 4.4(a) reveals a strong PDW nematicity in the cuprate $Bi_2Sr_2CaCu_2O_{8+x}$. This is demonstrated by plotting the histogram of $\mathcal{N}(\mathbf{r})$ shown in the inset of Fig. 4.4(a), where 45% of the FOV has $|\mathcal{N}(\mathbf{r})|>0.3$. This phenomenon is also evident from the original $I_m(\mathbf{r})$ data, as we can plot linecuts along the x and y directions within the domains, where $|\mathcal{N}(\mathbf{r})|\gg 0$ is shown in Fig. 4.4(b-c). This indicates that where $I_{m;x}(\mathbf{r})$ modulation is strong, $I_{m;y}(\mathbf{r})$ modulation is weak and vice versa.

Having identified the nematic PDW domains in nearly optimal-doped Bi-2212, the natural question is what sets the nematic domain boundaries. A hint comes from a recent transport study on 1% Zn substituted $La_{2-x}Ba_xCuO_4$ (LBCO) away from $p=1/8$ doping ($p=0.125$) [55]. Based on resistivity and susceptibility measurements, they find that two-dimensional (2D) superconductivity

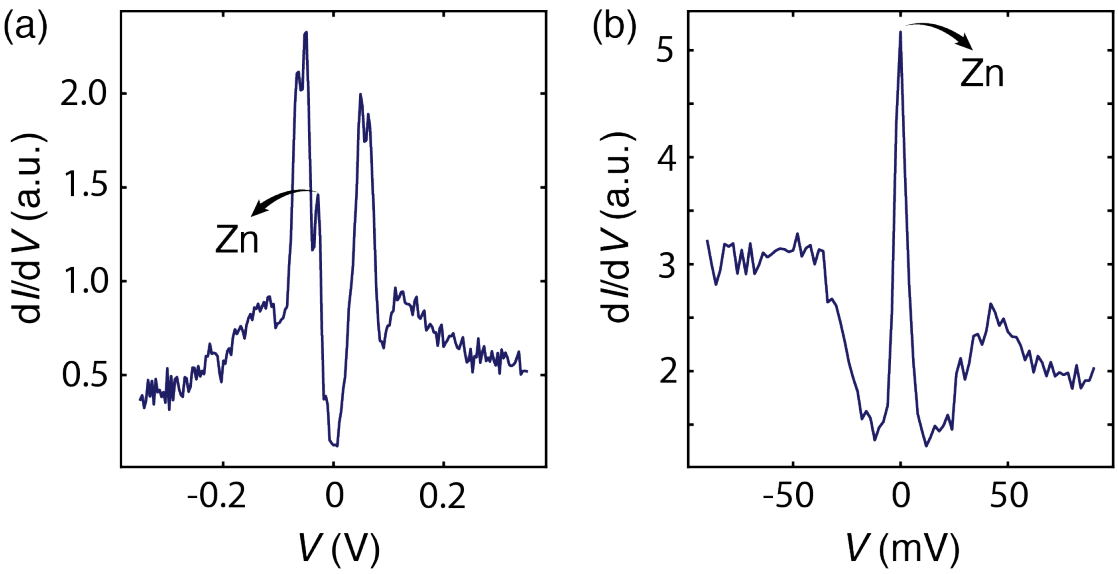

Figure 4.5: (a) SIS tunnelling spectra at a Zn impurity site on a near-optimally doped Bi-2212 sample measured by a superconducting Bi-2212 nano flake tip which shows coherence peaks near -20 mV. (b) NIS tunnelling spectra at a Zn impurity site on a near-optimally doped Bi-2212 sample measured by a normal tip, which shows coherence peaks near 0 V.

transition occurs below 26 K, which is well above that of the three-dimensional (3D) superconductivity. This is similar to the case of $p = 1/8$ doping LBCO where the occurrence of 2D superconductivity and suppression of 3D superconductivity is due to the frustration of the interlayer Josephson coupling, which is caused by the appearance of the PDW order [49, 56]. The inference is that the Zn impurities locally stabilise and pin the PDW order. In superconductive Bi-2212, the effects of Zn impurities are to 1) induce an impurity state near the energy of 1 eV and 2) suppress superconducting condensate [57]. The Zn impurity states can be directly measured in the differential conductance dI/dV spectrum that shows a broad peak near -1 meV [58]. For our BSCCO tip, the measured dI/dV spectrum is a result of the convolution between the coherence peaks of the tip near ± 20 mV and the Zn impurity peak of the sample near -1 mV. This gives rise to a spectral local maximum near 20 mV representing the Zn impurity state. The Zn impurity states can then be visualised by measuring the quantity

$$Z(\boldsymbol{r}) \equiv I(20\,\mathrm{mV}, \mathbf{r}) - I(-20\,\mathrm{mV}, \mathbf{r}) \tag{4.20}$$

where $I(V)$ is the single particle tunnelling current in the SIS STM junction. Each Zn impurity maximum is identified by blue circles in the $Z(\mathbf{r})$ image. And the $Z(\mathbf{r})$ and $\mathcal{N}(\mathbf{r})$ images are atomically registered in the same FOV. By superimposing the Zn impurity atoms onto the magnitude of the nematic order parameter $|\mathcal{N}(\mathbf{r})|$, it is evident that the Zn atoms are typically located near the nematic domain boundaries, as shown in Fig. 4.6(b). To quantify this phenomenon, we can compare the histogram of the distance between the Zn atom to the nearest domain boundary to the histogram of the distance between the randomly distributed points to the nearest domain boundary. Fig. 4.6(c) demonstrates that the Zn impurity sites reside highly towards the nematic PDW domain boundaries. Thus, our results suggest that the Zn impurity atoms at the Cu sites pin the nematic PDW domains, which agrees with the transport measurements in Zn-doped LSCO [55].

Our SJTM study of lightly underdoped BSCCO suggests that the PDW in BSCCO tends to be unidirectional and lattice-commensurate ($\lambda = 4a_0$), which is predicted by the CuO_2 Hubbard model in the strong coupling regime [55, 56, 59–66]. Furthermore, at the doping level ($p = 0.17$) in which our experiments are performed, the charge density wave (CDW) order is virtually non-existent. This indicates that the PDW order is not a subsidiary order of the CDW order but rather the primary order. Also, the nematic PDW order that we discovered breaks the 4-fold (C_4) rotational symmetry of the CuO_2 lattice but preserves the long-range translational symmetry. This agrees with the definition of the vestigial order, which only partially breaks the symmetry of the parent order state.

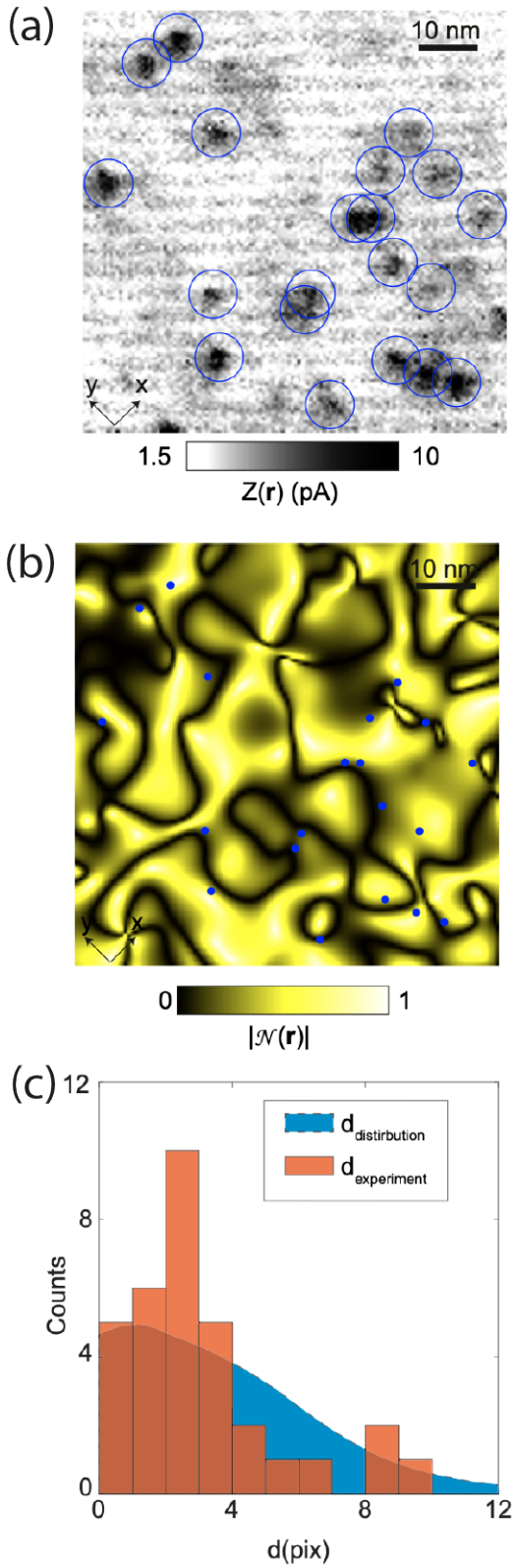

Figure 4.6: (a) Locations of Zn impurity atoms $Z(\mathbf{r})$ as detected in $Z(r) \equiv I(\mathbf{r}, 20\text{mV}) - I(\mathbf{r}, -20\text{mV})$ are shown as blue circles. (B) $|\mathcal{N}(\mathbf{r})|$, the amplitude of the nematic order parameter from Fig. 4.4(a), with the sites of Zn impurity resonances overlaid as blue dots. (c) The distribution of distances between each Zn impurity atom and its nearest PDW domain walls (red). This is compared to the expected average distance if no correlation exists between Zn impurity atoms and the PDW domain walls (blue). Zn impurity atoms are concentrated near the PDW domain walls.

Part of this chapter appears as:

Proc. Nat'l Acad. Sci. ***119****, 2207449119*

— Wangping Ren *at al.*

5

Electron pairing mechanism of high-T_C cuprate superconductivity

Contents

In this chapter, I will present an analogue isotope effect experiment to study the electron-pairing mechanism in nearly optimally doped $Bi_2Sr_2CaCu_2O_{8+x}$ (Bi-2212), in which the superexchange interactions are controllably varied and the consequent effects on the electron-pair wavefunction Ψ are directly measured[1]. The experimental results

[1]The data analysis presented in this chapter was performed using MATLAB. M. H. Hamidian at Cornell University carried out the SJTM measurements.

compare excellently with predictions from strong-correlation theory for hole-doped charge-transfer insulators, indicating that the charge-transfer superexchange is key to the electron-pairing mechanism of superconductive Bi-2212.

5.1 Charge-transfer superexchange

The elementary CuO_2 plane is believed to be responsible for the high-temperature superconductivity in the cuprates. It was proposed by Philip W. Anderson in 1987 [21] that it was the *superexchange* interactions between electrons on the adjacent Cu sites that caused the electron-pair binding. The superexchange spin-spin interaction occurs at the energy $J \approx 4t^4/\mathcal{E}^3$, where $\mathcal{E}$ is the charge-transfer energy that defines the energy difference between the relevant orbitals on the adjacent Cu and O atoms, and electrons transition between them at rate $t/\hbar$.

Besides the d-electrons in the transition metal ion, the oxygen p orbital also plays a significant role in most transition metal oxides. In the case of cuprate superconductors, the singly occupied Cu^{2+} $(3d^9)$ ions are separated by the doubly occupied O^{2-} $(2p^6)$ ions in the square CuO_2 plane. The energy of the O p_σ orbital ε_p lies above that of the Cu d orbital ε_d (Fig. 5.1). Here, because of the Coulomb double occupancy energy U at Cu d orbitals, the degeneracy of the Cu $d_{x^2-y^2}$ orbitals is lifted so that the O p_σ orbitals are separated from the upper Cu $d_{x^2-y^2}$ band by the charge transfer energy

$$\mathcal{E} = (\varepsilon_d + U) - \varepsilon_p. \tag{5.1}$$

The exchange interaction between the singly occupied d-electrons thus involves hopping via the intermediate O orbitals. This is called the *superexchange*. For simplicity, consider the interaction between two Cu sites mediated by one O site only and ignore the onsite Coulomb repulsion at the O site. In the case of two anti-parallel spins on the Cu sites with one intervening O site (Fig. 5.1(b)), the basis

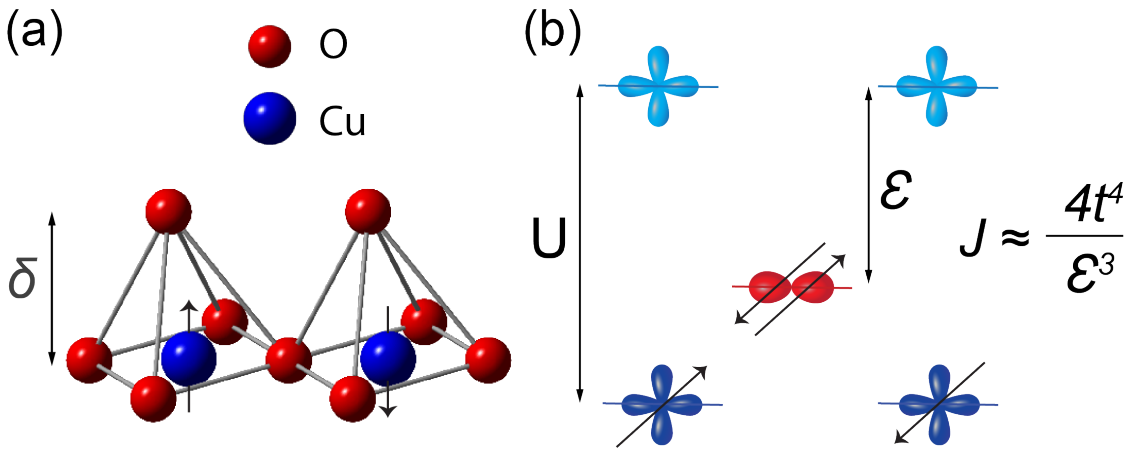

Figure 5.1: (a)Schematic representation of CuO_5 pyramids whose bases comprise the CuO_2 plane. (b) Schematic of the electronic structure of the CuO_2 plane.

that spans the Hilbert space is nine-dimensional. The corresponding Hamiltonian matrix has the following form [67]:

$$\mathcal{H} = \left(\begin{array}{cc|cccc|ccc} 0 & 0 & +t_{pd} & +t_{pd} & 0 & 0 & 0 & 0 & 0 \\ 0 & 0 & 0 & 0 & +t_{pd} & +t_{pd} & 0 & 0 & 0 \\ \hline +t_{pd} & 0 & U+\mathcal{E} & 0 & 0 & 0 & -t_{pd} & 0 & -t_{pd} \\ +t_{pd} & 0 & 0 & U+\mathcal{E} & 0 & 0 & 0 & -t_{pd} & -t_{pd} \\ 0 & +t_{pd} & 0 & 0 & U+\mathcal{E} & 0 & +t_{pdd} & 0 & +t_{pdd} \\ 0 & +t_{pd} & 0 & 0 & 0 & U+\mathcal{E} & 0 & +t_{pd} & +t_{pd} \\ \hline 0 & 0 & -t_{pd} & 0 & +t_{pd} & 0 & U & 0 & 0 \\ 0 & 0 & 0 & -t_{pd} & 0 & +t_{pd} & 0 & U & 0 \\ 0 & 0 & -t_{pd} & -t_{pd} & +t_{pd} & +t_{pd} & 0 & 0 & 2\,(U+\mathcal{E}) \end{array}\right)$$

where t_{pd} is the hopping rate between the Cu and O sites. In the limit of large U, states with at least one doubly occupied d-orbital can be projected out, and the downfolded effective Hamiltonian has the Heisenberg form:

$$\mathcal{H}_{\text{eff}} = J\mathbf{S}_1 \cdot \mathbf{S}_2 \tag{5.2}$$

with the superexchange coupling

$$J = \frac{4t_{pd}^4}{\mathcal{E}^2}\left(\frac{1}{U} + \frac{1}{\mathcal{E}}\right) \tag{5.3}$$

where $\mathbf{S_1}, \mathbf{S_2}$ are the electron spin operators at Cu sites. Since the $J > 0$, states with antiparallel d-electron spins have lower energy, and thus, the superexchange interaction leads to antiferromagnetism. Note that the superexchange interaction

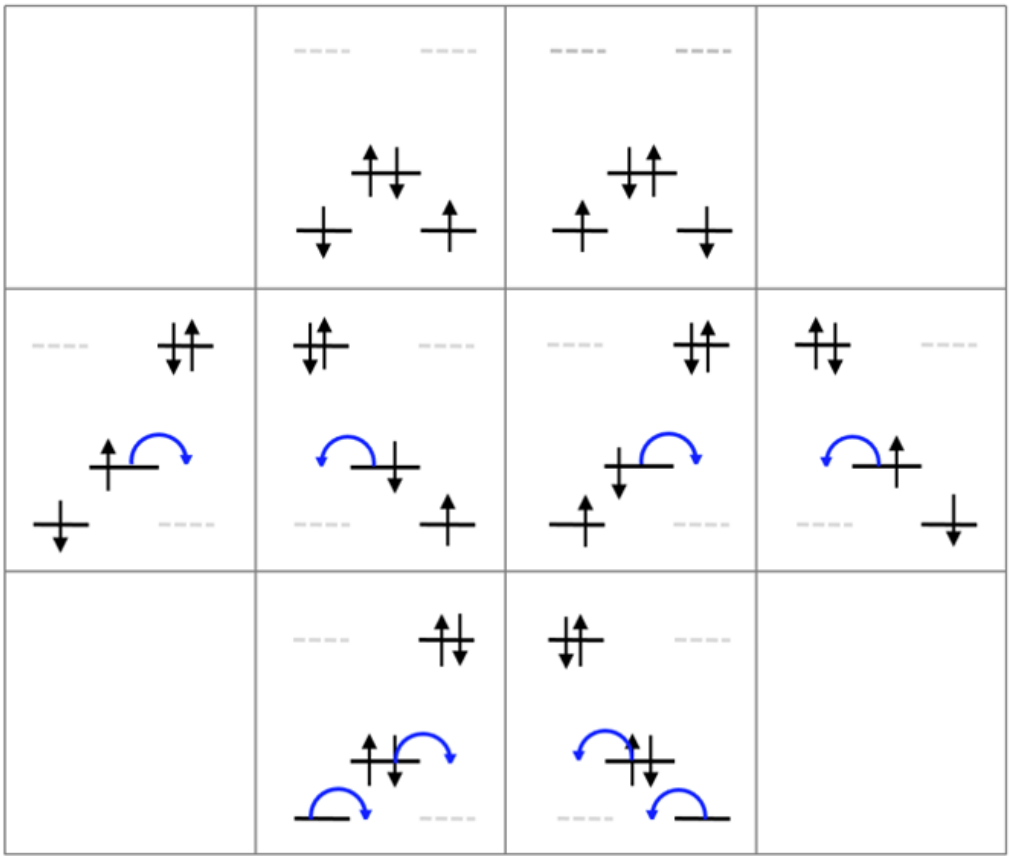

Figure 5.2: Possible electron configurations in the CuO_2 unit cell due to the superexchange interaction. Ground states are shown in the top row, followed by various excited states. Figure reproduced from [68].

involves a multi-stage hopping process with two possibilities. The first one is described by the first term in Eqn. 5.3 and involves a single doubly occupied d orbital. This is analogous to the direct exchange between d-electrons in the one-band Hubbard model with $J_{dd} = 4t_{\text{eff}}^2/U$ where $t_{\text{eff}} = t_{pd}^2/\mathcal{E}$. The second possibility involves two doubly occupied d orbitals shown in Fig. 5.2. This is represented by the second term in Eqn. 5.3. In the strong coupling limit where $\frac{U}{t} \gg 1$, the superexchange coupling constant in Eqn. 5.3 reduces to

$$J \approx \frac{4t_{pd}^4}{\mathcal{E}^3}. \tag{5.4}$$

Indeed, because of the large energy cost to doubly occupy any $d_{x^2-y^2}$ orbital, the d electrons become fully Mott localised and the CuO_2 plane is in a charge-transfer insulator state.

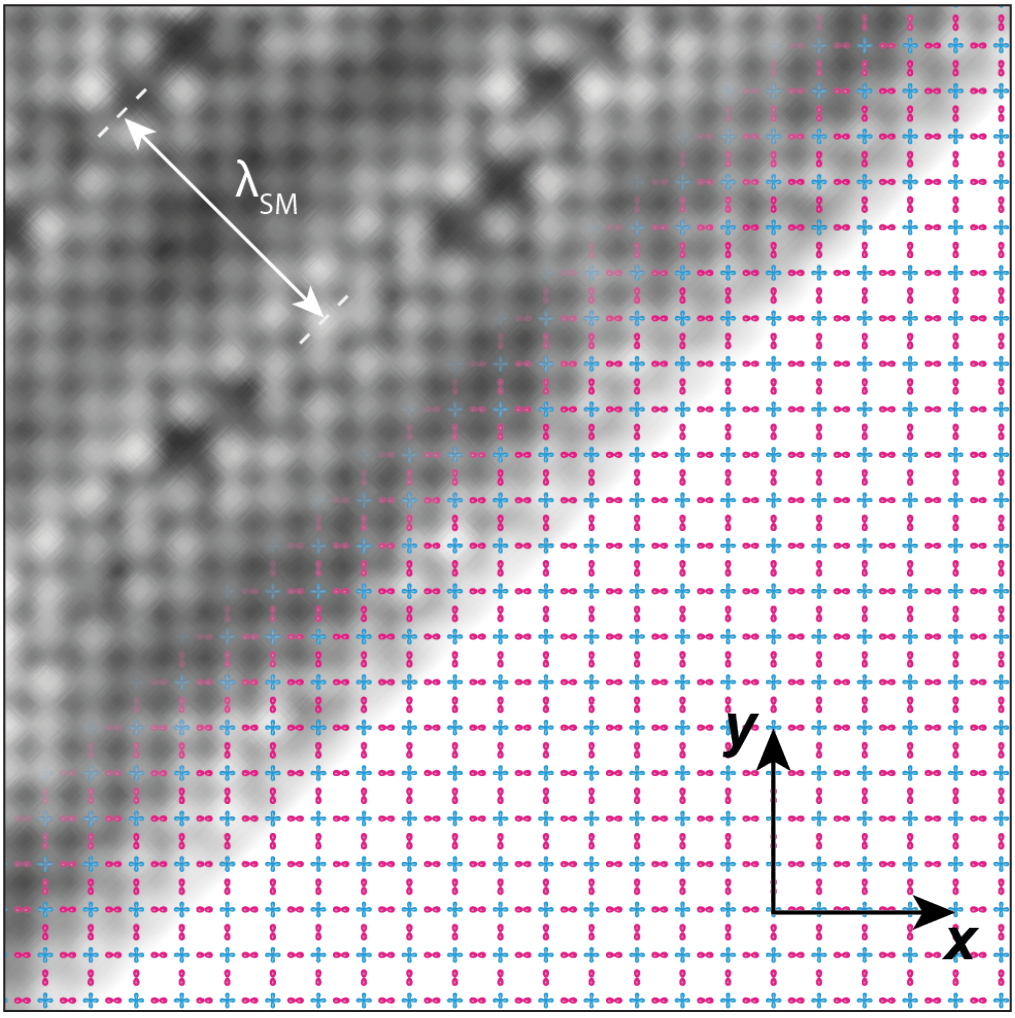

Figure 5.3: Schematic of CuO_2 partially overlaid by a $Bi_2Sr_2CaCu_2O_{8+x}$ topographic image $T(\mathbf{r})$ to exemplify how the crystal supermodulation modulates along the (1,1) axis, with one period $0 \leq \Phi \leq 2\pi$ being approximately 26 Å. The Cu to apical O distance δ is modulated at the same wavevector but perpendicular to this plane.

Differing from the Mott insulator state where $U \ll \mathcal{E}$, the lowest excitation state of a charge-transfer insulator involves the O orbital, as $d^n d^n \rightarrow d^n p^5 d^{n+1}$, instead of $d^n d^n \rightarrow d^{n-1} d^{n+1}$ in the Mott insulator case. Consequently, any doped holes into the charge transfer insulator would go into the O orbitals. Under such circumstances, an electronic structure with $t \approx 0.4$ eV and $\mathcal{E} \approx 1$ eV implies a superexchange energy $J \approx 100$ meV which should stabilise a robust spin-1/2, $\mathbf{Q} = (\pi, \pi)$ antiferromagnetic state. Indeed, this is exactly what was observed by inelastic neutron scattering in La_2CuO_4 [69], confirming that the charge-transfer superexchange interaction is the mechanism of antiferromagnetism in undoped CuO_2.

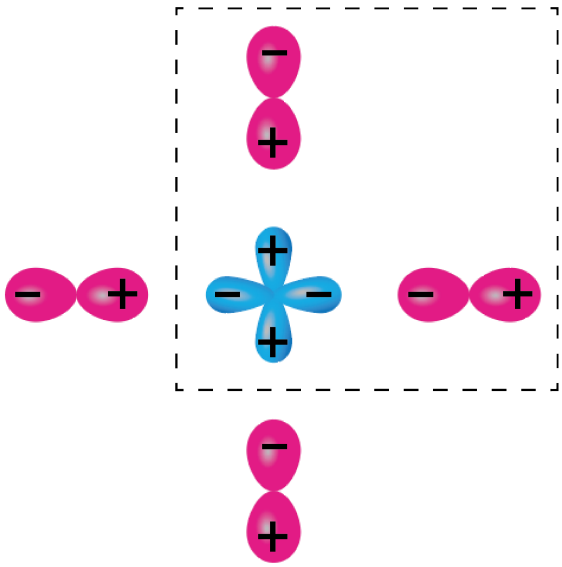

Figure 5.4: Schematic of the Emery three-band model. Cu d orbital is shown in light blue, and O p orbitals in pink. The dashed square indicates the CuO_2 unit cell that contains five electrons (undoped).

5.2 Superexchange mediated electron pairing

5.2.1 Three-band Hubbard model

Upon doping holes into the CuO_2 plane, which primarily enters the p_σ orbitals [70], the electrons become delocalised, and the long-range antiferromagnetic order is disrupted. This scenario can be closely modelled by the three-band (or Emery) Hubbard model [71], wherein the electron mobility is characterized by the hopping rate t:

$$\mathcal{H} = \sum_{i\alpha j\beta\sigma} t_{ij}^{\alpha\beta} c_{i\alpha\sigma}^{\dagger} c_{j\beta\sigma} + \sum_{i\alpha\sigma} \varepsilon_\alpha n_{i\alpha\sigma} + U_{dd} \sum_{i\sigma} n_{id\uparrow} n_{id\downarrow} \tag{5.5}$$

where i, j enumerate planer CuO_2 unit cells; α, β label any of the three orbitals; $t_{ij}^{\alpha\beta}$ are transition rates for electrons between orbitals α, β at sites i, j; ε_α are orbital energies; and $n_{id\uparrow}, n_{id\downarrow}$ are $d_{x^2-y^2}$ orbital occupancies by spin state. Note that only the interaction on Cu sites is considered. The CuO_2 unit cell is depicted in Fig. 5.4 where 5 electrons are included (4 from the two O orbitals, 1 from the Cu orbital). Using the following Nambu spinor basis [72]:

$$\Psi(\mathbf{k}) = \begin{pmatrix} \Psi_\uparrow(\mathbf{k}) \\ \Psi_\downarrow(\mathbf{k}) \end{pmatrix} \quad \Psi_\uparrow(\mathbf{k}) = \begin{pmatrix} d_\uparrow(\mathbf{k}) \\ p_\uparrow^x(\mathbf{k}) \\ p_\uparrow^y(\mathbf{k}) \end{pmatrix} \quad \Psi_\downarrow(\mathbf{k}) = \begin{pmatrix} d_\downarrow^\dagger(-\mathbf{k}) \\ p_\downarrow^{x\dagger}(-\mathbf{k}) \\ p_\downarrow^{y\dagger}(-\mathbf{k}) \end{pmatrix} \tag{5.6}$$

which contains the electron operators on the Cu $d_{x^2-y^2}$ and O p_x and p_y orbitals, Eqn. 5.5 can then be re-written as [73]:

$$\mathcal{H} = \sum_{k\sigma} \Psi^{\dagger}_{k\sigma} h_0(k) \Psi_{k\sigma} + U \sum_i n^d_{i\uparrow} n^d_{i\downarrow} \tag{5.7}$$

where $h_{\mathbf{0}}(\mathbf{k})$ is the non-interacting Hamiltonian. Eqn. 5.7 then has the same form as the one-band Hubbard model (Eqn. 1.23) with the replacements: $c_{k\sigma} \rightarrow \Psi_{k\sigma}$. Heuristically, such a model represents a strongly correlated metallic state with strong antiferromagnetic exchange interactions between spins. Consequently, a natural question arises: is it the superexchange interaction between Cu spins that binds two electrons together and gives rise to the high- T_c superconductivity in cuprates? This is signified by the emergence of the electron pair condensate $\Psi \equiv \langle c_{i\downarrow} c_{j\uparrow} \rangle$, a quantity that is directly measurable using SJTM as discussed in detail in Chapter 2.

5.2.2 DMFT

Because of the large parameter space, exact diagonalisation of the three-band model has proven exceptionally challenging. However, with the modern advancement of numerical techniques and computing power, the solution of Eqn. 5.7 is possible, such as the application of dynamical-mean field theory (DMFT). In this section, I will follow closely the thesis of Kowalski [72] and give a brief introduction to DMFT and its application in superconductivity.

Introduction

Early insights into the correlated electron problem emerged in 1989 when Metzner and Vollhardt [74] analysed the Hubbard model in infinite dimensions ($d \rightarrow \infty$), equivalently, with infinitely many neighbouring atoms. In this limit, they proposed that the electron self-energy is momentum-independent, i.e. $\Sigma(\boldsymbol{k}, \omega) \overset{d\rightarrow\infty}{\longrightarrow} \Sigma(\omega)$, and the competition between U and t is preserved under appropriate scaling. Consequently, the infinite-dimensional Hubbard model can be regarded as a local problem in space where spatial fluctuations are neglected while preserving temporal on-site electron-electron correlations. This understanding motivated Georges et al.

[75] to develop a dynamical mean-field theory in infinite dimensions for calculating the self-energy $\Sigma(\omega)$, which maps the lattice Hubbard model onto a self-consistent Anderson impurity model. In this framework, the local on-site interaction can be viewed as an impurity embedded in a non-interacting electron bath. Unlike classical mean-field theory, this site in DMFT is now a dynamic entity that undergoes transitions between four possible states $|0\rangle, |\uparrow\rangle, |\downarrow\rangle, |\downarrow\uparrow\rangle$, and thus the term 'dynamical'.

To present the self-consistent DMFT equations, let's start with the original one-band lattice Hubbard model:

$$H = -\sum_{\langle ij\rangle,\sigma} t_{ij}\left(c^{\dagger}_{i\sigma}c_{j\sigma} + c^{\dagger}_{j\sigma}c_{i\sigma}\right) + U\sum_{i} n_{i\uparrow}n_{i\downarrow} \tag{5.8}$$

where the electron hopping t_{ij} is between the nearest neighbour sites and $\left\{c^{\dagger}_{i\sigma}, c_{j\sigma}\right\}$ the fermion operators with spin index σ. In the path integral language, the corresponding full Green's function $G^{\sigma}_{ii}(\tau,\tau') \equiv -\left\langle \mathcal{T} c_{i\sigma}(\tau)c^{\dagger}_{i\sigma}(\tau')\right\rangle_{S}$ that governs the temporal fluctuations of the electron occupancy at a typical lattice site reads

$$G^{\sigma}_{ii}(\tau,\tau') = \frac{1}{\mathcal{Z}}\int \mathcal{D}\psi^{*}_{i\sigma}\mathcal{D}\psi_{i\sigma}\left[c_{i\sigma}(\tau)c^{\dagger}_{i\sigma}(\tau')\right]e^{-S} \tag{5.9}$$

where

$$\mathcal{Z} = \int \mathcal{D}\psi^{*}_{i\sigma}\mathcal{D}\psi_{i,\sigma}e^{-S} \tag{5.10}$$

is the partition function, and

$$\begin{aligned} S = \int_{0}^{\beta} d\tau \Bigg[&\sum_{i\sigma} c^{\dagger}_{i\sigma}(\tau)\left(\frac{\partial}{\partial\tau} - \mu\right)c_{i\sigma}(\tau) + \sum_{ij\sigma} t_{ij}c^{\dagger}_{i\sigma}(\tau)c_{j\sigma}(\tau) \\ &+ \sum_{i} U c^{\dagger}_{i\uparrow}(\tau)c_{i\uparrow}(\tau)c^{\dagger}_{i\downarrow}(\tau)c_{i\downarrow}(\tau) \end{aligned} \tag{5.11}$$

is the imaginary-time action for the Hubbard model [76] and $\psi^{*}_{i\sigma}, \psi_{i\sigma}$ the Grassmann variables. In the non-trivial limit of infinite dimensions, Georges et al. [75] show that the Hubbard action S reduces to an effective local action

$$\begin{aligned} S \xrightarrow{d\to\infty} S_{\mathrm{Imp}} = &-\int_{0}^{\beta} d\tau \int_{0}^{\beta} d\tau' \sum_{\sigma} c^{\dagger}_{o\sigma}(\tau)\mathcal{G}^{-1}_{0}(\tau-\tau')\, c_{o\sigma}(\tau') \\ &+ U\int_{0}^{\beta} d\tau n_{o\uparrow}(\tau)n_{o\downarrow}(\tau) \end{aligned} \tag{5.12}$$

which is essentially a description of a single impurity site o under the time-dependent mean field $\mathcal{G}_0^{-1}$ with onsite interaction U. Physically, this is completely analogous to the Anderson impurity model, where the extra degrees of freedom of the noninteracting electron bath is added. The Anderson Hamiltonian reads [72]

$$H_{\mathrm{AM}} = \overbrace{\sum_{\sigma} \epsilon_o c_{o\sigma}^{\dagger} c_{o\sigma} + U n_{o\uparrow} n_{o\downarrow}}^{\text{Impurity part}} + \overbrace{\sum_{l\sigma} \epsilon_l c_{l\sigma}^{\dagger} c_{l\sigma}}^{\text{Electron bath part}} + \overbrace{\sum_{\langle o,j\rangle,\sigma} \left(V_{oj} c_{o\sigma}^{\dagger} c_{j\sigma} + \text{ h.c. } \right)}^{\text{Hybridisation part}}. \quad (5.13)$$

where AM stands for Anderson Model. Since the non-interacting electrons enter H_{AM} as a quadradic form, it can then be integrated out [77], and this results in an action of the same form as in Eqn. 5.12, with the 'mean-field'

$$\mathcal{G}_0^{-1}\left(i\omega_n\right)^{\mathrm{AM}} = i\omega_n + \mu - \Delta_{\mathrm{AM}}\left(i\omega_n\right) \quad (5.14)$$

where $\Delta_{\mathrm{AM}}\left(i\omega_n\right)$ includes the hybridisation term and the conducting bath that is integrated out, $\omega_n = (2n+1)\pi/\beta\,(\beta = 1/k_B T)$ the fermionic Matsubara frequency, μ the chemical potential. Thus, the Anderson impurity model Eqn. 5.13 can be regarded as the Hamiltonian representation of the effective local action of S_{Imp} . The interacting Green's function of S_{Imp} can then be obtained from the Dyson's equation

$$\left[G_{\mathrm{Imp}}\ \left(i\omega_n\right)\right]^{-1} = \left\langle \mathcal{T} c\left(i\omega_n\right) c^{+}\left(i\omega_n\right) \right\rangle_{S_{\mathrm{Imp}}}^{-1} = \mathcal{G}_0^{-1}\left(i\omega_n\right) - \Sigma_{\mathrm{Imp}}\left(i\omega_n\right) \quad (5.15)$$

where Σ_{Imp} is the impurity self-energy. To establish a mapping between the Hubbard model and the Anderson impurity model, this requires equivalence between the Green's function $G\left(i\omega_n\right)$ calculated from the effective impurity action S_{Imp} and the onsite local part of the original lattice Green's function $G_{ii}\left(i\omega_n\right)$. The self-consistency condition then reads [72]

$$\frac{1}{\mathcal{G}_0^{-1}\left(i\omega_n\right)^m - \Sigma\left(i\omega_n\right)} = G_{\mathrm{Imp}}\left(i\omega_n\right) = G_{ii}\left(i\omega_n\right) = \sum_k \frac{1}{i\omega_n + \mu - \epsilon(k) - \Sigma\left(i\omega_n\right)} \quad (5.16)$$

where the original lattice self-energy $\Sigma\left(i\omega_n\right)$ is momentum independent as $d \to \infty$ and $\Sigma = \Sigma_{\mathrm{Imp}}\left(i\omega_n\right)$.

The local Green's function G and self-energy Σ of the Hubbard model can then be determined from a closed set of the DMFT mean-field equations Eqn. 5.12 - Eqn. 5.16. These equations can be solved iteratively until convergence using modern numerical techniques. A schematic describing the algorithm is shown in Fig. 5.5.

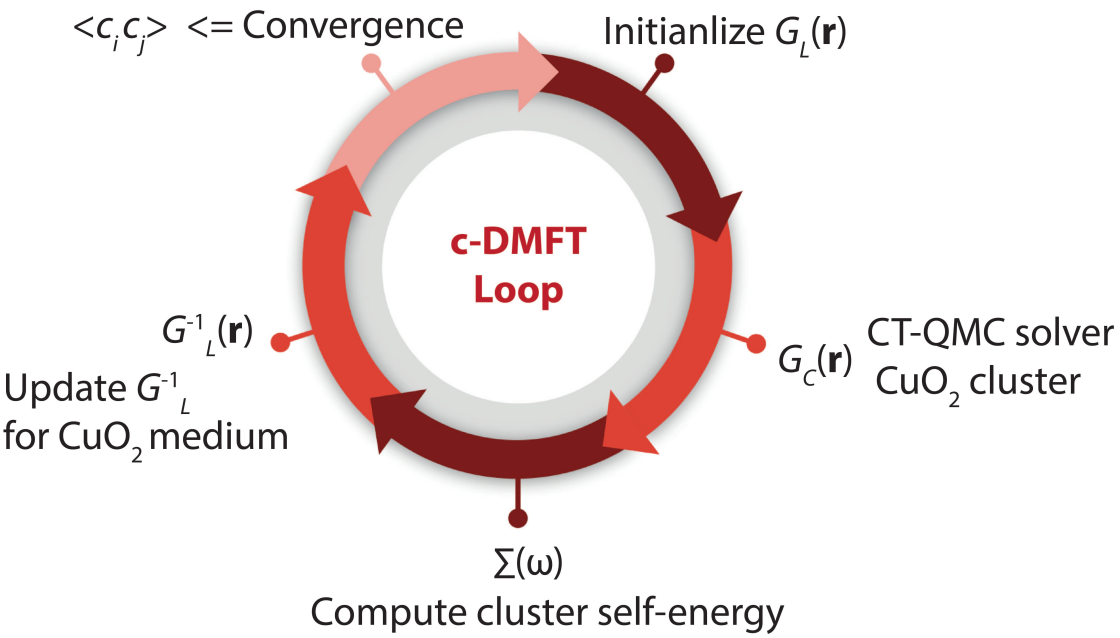

Figure 5.5: Self-consistent loop for the iterative solution of DMFT equations. G_L, lattice Green's function. G_C, cluster Green's function. CT-QMC, continuous-time Monte Carlo. c-DMFT, cluster dynamical mean-field theory. Figure reproduced from [68].

Superconductivity

Superconductivity is characterised by the non-vanishing of the order parameter, i.e. $\Delta_k = \langle c_{k\uparrow} c_{-k\downarrow} \rangle \neq 0$, which is conveniently described by the anomalous Green's function $F(\mathbf{k}, \tau) = -\langle \mathcal{T} c_{\mathbf{k}\uparrow}(\tau) c_{-\mathbf{k}\downarrow} \rangle \overset{\tau \to 0^+}{\longrightarrow} \Delta_{\mathbf{k}}$. With the non-vanishing $F(k, \tau)$, the DMFT mean field equations can be extended to calculate the superconductivity of the one-band Hubbard model in Eqn. 5.8. In the basis of Nambu spinor $\Psi_k^+ \equiv \left(c_{k\uparrow}^+, c_{-k\downarrow}\right)$, the matrix representation of the single-particle Green's function is

$$\widehat{G}(\mathbf{k}, \tau) \equiv -\left\langle \mathcal{T} \Psi_{\mathbf{k}}(\tau) \Psi_{\mathbf{k}}^+(0) \right\rangle \tag{5.17}$$

$$= \begin{pmatrix} G(\mathbf{k}, \tau) & F(\mathbf{k}, \tau) \\ F(\mathbf{k}, \tau)^\dagger & -G(-\mathbf{k}, -\tau)^\dagger \end{pmatrix}. \tag{5.18}$$

Since the quadratic terms in the Hubbard Hamiltonian can be eventually integrated out in the calculation of its impurity action, we can then add a pairing field $\eta(\mathbf{k}) = \eta'(\mathbf{k}) + i\eta''(\mathbf{k})$ that couples the particle pairs $c_{\mathbf{k}\uparrow} c_{-\mathbf{k}\downarrow}$ to the noninteracting part of Eqn. 5.8 so that it reads [78]

$$H_0 = \Sigma_k \Psi_k^\dagger \left[\epsilon_k \sigma_3 - \eta'(\mathbf{k}) \sigma_1 + \eta''(\mathbf{k}) \sigma_2 \right] \Psi_{\mathbf{k}} \tag{5.19}$$

where σ_i are the Pauli matrices. The corresponding impurity action has the form

$$S_{\mathrm{Imp}} = U \int_0^\beta d\tau n_\uparrow(\tau) n_\downarrow(\tau) - \int_0^\beta d\tau \int_0^\beta d\tau' \Psi^+(\tau) \mathcal{G}_0^{-1}(\tau - \tau') \Psi(\tau') \tag{5.20}$$

where $\mathcal{G}_0^{-1}$ contains the dynamical pairing field applied to all sites of the bath. Physically, this describes an impurity being immersed in a superconducting bath. The matrix self-energy is

$$\widehat{\Sigma} = \mathcal{G}_0^{-1} - \hat{G}^{-1} = \begin{pmatrix} \Sigma(i\omega_n) & S(i\omega_n) \\ S(i\omega_n) & -\Sigma(i\omega_n)^\dagger \end{pmatrix} \tag{5.21}$$

where S is the anomalous self-energy that describes pairing. The lattice matrix Green's function can then be written as

$$\hat{G}(k, i\omega_n) = \begin{pmatrix} \omega_n + \mu - \epsilon(k) - \Sigma(i\omega_n) & S(i\omega_n) \\ S(i\omega_n) & \omega_n - \mu + \epsilon(k) + \Sigma(i\omega_n)^\dagger \end{pmatrix}. \tag{5.22}$$

Finally, self-consistency is achieved by equating the impurity matrix Green's function calculated from the impurity action to the lattice matrix Green's function of Eqn. 5.22. After convergence is achieved, the superconducting order parameter can then be calculated.

DMFT predictions

Recently, cluster dynamical mean-field theory (c-DMFT) analysis of the CuO_2 Hubbard model has yielded quantitative predictions of the hole-doped cuprates. Kowalski et al. [73] use four CuO_2 unit cells (4 Cu orbitals and 8 O orbitals) as a quantum impurity cluster and solve the c-DMFT equations based on the three-band Hubbard model using realistic parameters of Bi-2212. A calculated density-of-states vs. energy spectrum is shown in Fig. 5.6, which clearly shows a charge-transfer gap for 13 % hole-doped Bi-2212 at $T = 0$. More importantly, their numerical results show that the superconducting order parameter Ψ decreases monotonically as the charge-transfer energy $\mathcal{E}$ increases (Fig. 5.8), suggesting that the electron pairing in CuO_2 is controlled by $\mathcal{E}$ and thus the superexchange J (Eqn. 5.4). Furthermore, theory based on DMFT also indicates that the interplay between $\mathcal{E}$ and Ψ can be adjusted by altering the distance δ between each Cu atom and the

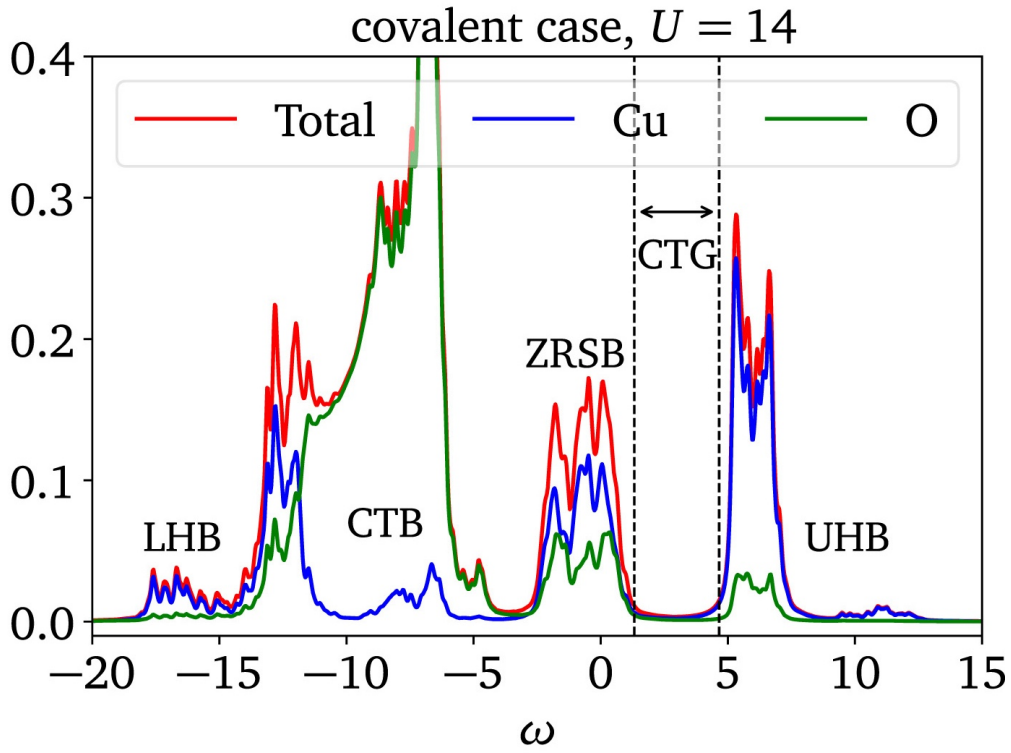

Figure 5.6: c-DMFT predicted density of states vs. frequency spectrum based on the three-band model for 13 % hole-doped Bi-2212 at $T = 0$ in the covalent case ($\epsilon_p - \epsilon_d = 1.50$ eV, $t_{pd} = 1.37$ eV, $t'_{pp} = 0.13$ eV). LHB, lower Hubbard band. UHB, upper Hubbard band. CTG, charge-transfer gap. CTB, charge-transfer band. Figure reproduced from Kowalski et al. [73].

out-of-plane apical O atom of its CuO_5 pyramid [71]. This is because as δ is varied, so is the Coulomb potential at the planar Cu and O atoms, which modifies $\mathcal{E}$ and thus controls Ψ in a predictable manner [71, 79, 80]. Indeed, this situation has been strongly supported since the discovery of cuprate superconductivity [81–84]. These quantitative predictions based on real material parameters provide great experimental opportunities: including determining the dependency of Ψ on $\mathcal{E}$ at the Cu atom beneath each displaced apical oxygen atom. This may provide valuable insight into the change in Ψ with respect to $\mathcal{E}$, i.e. $(d\Psi/d\mathcal{E})$, as a direct evaluation of a charge-transfer superexchange electron-pairing mechanism. The challenge for experimentalists thus lies in measuring the correlation between Ψ and $\mathcal{E}$ directly and simultaneously at the superconducting CuO_2 plane. If such data is acquired, it can serve a role similar to the *isotope effect* in conventional BCS superconductors, by empirically identifying the specific electron-electron interaction responsible for

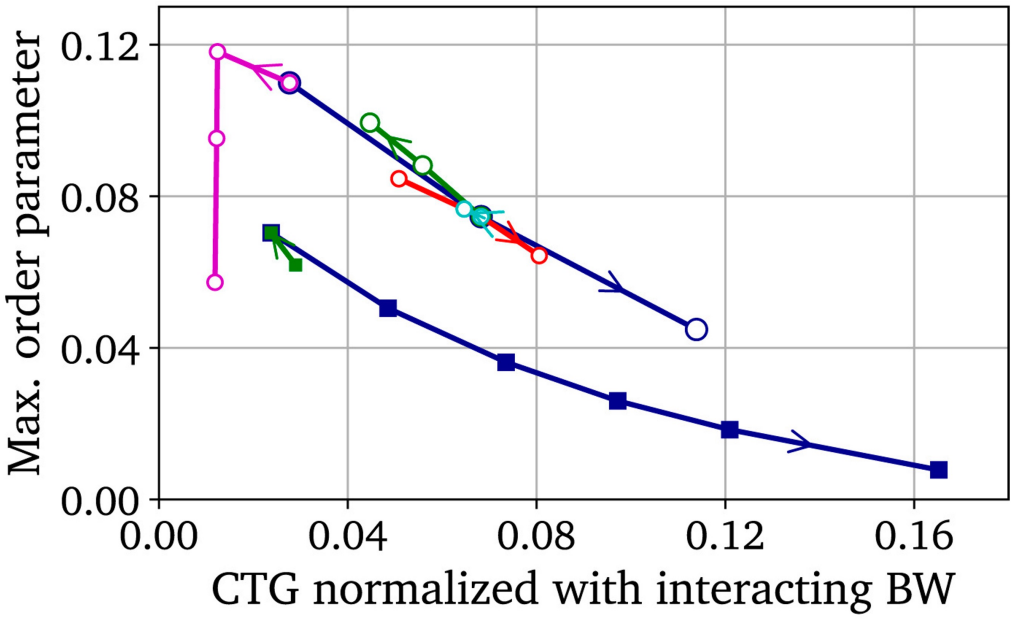

Figure 5.7: Superconducting order parameter as a function of the charge-transfer gap (CTG) predicted by the c-DMFT calculations for optimally doped cuprates. For each colour, only one material parameter is varied. Figure reproduced from Kowalski et al. [73].

electron-pair formation in cuprates.

5.2.3 Previous bulk studies

In the past, many studies concerned the relationship between $\mathcal{E}$ and J in bulk cuprate crystals. For example, optical reflectivity measurements [85, 86] show that the charge-transfer energy $\mathcal{E}$ is 1 eV $< \mathcal{E} <$ 2 eV in the undoped insulating state of the cuprate crystals which become superconducting after hole-doping. An energy $J \sim 150$ meV is identified as the superexchange energy of the electron-pair excitations according to Raman scattering studies [85–87]. Spectroscopic studies using single-electron tunnelling [88] indicate that in the insulating parent state, the charge transfer energy in $Bi_2Sr_2CaCu_2O_{8+x}$ is $\mathcal{E} \gtrsim 1$ eV. Additionally, as $\mathcal{E}$ measured in the undoped insulator increases, there's a decreasing trend in the maximum T_c measured in the corresponding superconductor across various material samples. Also, from ARPES studies [89], the reported transitions to unoccupied states is consistent with the on-site Cu double occupancy energy $U \sim 2.7$ eV, and the charge-transfer energy in optimally-doped $Bi_2Sr_2CaCu_2O_{8+x}$ which

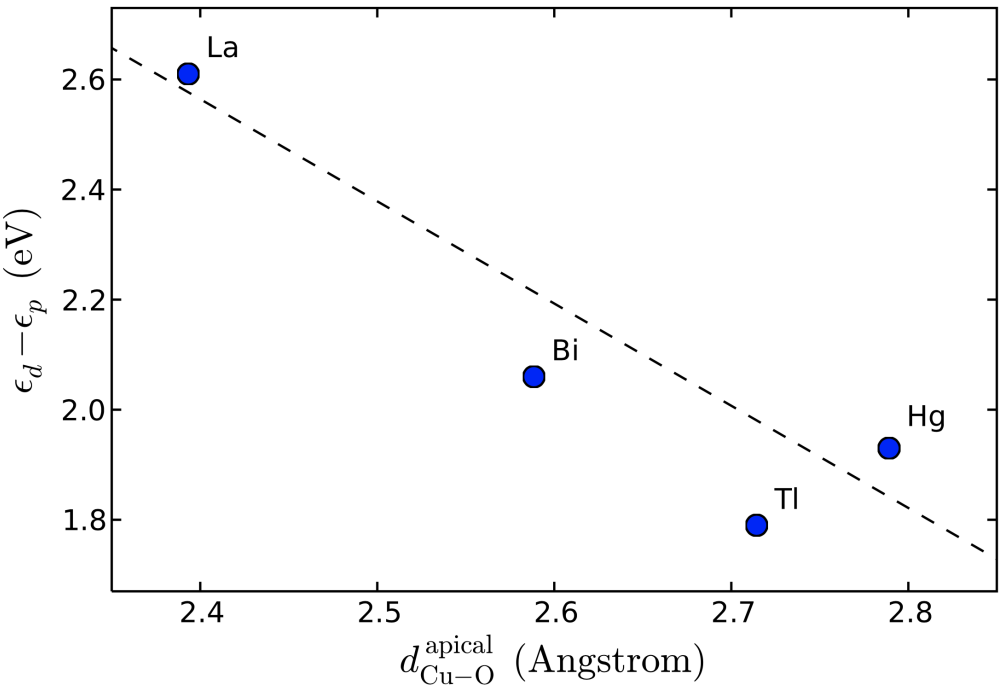

Figure 5.8: Apical O distance as a function of the charge-transfer energy from DMFT. Figure reproduced from Weber et al. [71].

is $\mathcal{E} \approx 1.1$ eV. Resonant inelastic X-ray scattering [90, 91] directly shows that 140 meV $< J <$ 180 meV from spin wave excitation spectra spanning many cuprate materials. Furthermore, a recent X-ray absorption spectra study [92] of optimally-doped superconducting $(Ca_xLa_{1-x})\,(Ba_{1.75-x}La_{0.25+x})\,Cu_3O_y$ at both the Cu-L edge and O-K edge reveals that $\mathcal{E} \approx 1.3$ eV.

According to Eqn. 5.4, a comprehensive understanding of the charge-transfer superexchange as the mechanism of CuO_2 superconductivity necessitates examining the empirical relationship between the electron-pair condensate Ψ and the charge-transfer energy $\mathcal{E}$. However, this has been difficult to achieve experimentally. Despite the pioneering studies on bulk crystals mentioned above, accessing different $\mathcal{E}$ values typically involves switching between crystal families in the antiferromagnetic insulator state. This makes it impossible to simultaneously measure $\mathcal{E}$ and Ψ in the same superconducting state. Alternatively, the maximum superconducting critical temperature T_c after hole doping is often proposed as a proxy for Ψ and then compared with the $\mathcal{E}$ derived from the parent insulator, for a range of different

compounds. But this method is not definitive. Changing the crystal family affects many material parameters besides $\mathcal{E}$, and T_c is influenced by other factors such as dimensionality and superfluid phase stiffness [16]. More fundamentally, modern theoretical analysis has recently revealed that there is no direct correspondence between T_c and Ψ in the CuO_2 Hubbard model [73, 93]. Therefore, although encouraging, studies comparing maximum superconducting T_c and with insulating $\mathcal{E}$ cannot conclusively determine the electron-pairing mechanism. On the other hand, muon spin rotation studies do show that Ψ decreases rapidly with increasing correlations while approaching the charge-transfer insulator state [17]. Ultimately, to identify the fundamental physics of electron pairing, it is crucial to directly and systematically measure the dependence of the electron-pair condensate Ψ on the charge-transfer energy $\mathcal{E}$ at the same hole density.

5.3 Methods for measuring δ, $\mathcal{E}$ and Ψ

To investigate this possibility, it is crucial to determine both Ψ and $\mathcal{E}$ as a function of the apical distance δ above each planer Cu atom. My approach combines atomic-resolution imaging with a fortuitous characteristic of the canonical cuprate $Bi_2Sr_2CaCu_2O_{8+x}$. Due to the mismatch between the preferred bound lengths of the rock-salt and perovskite layers, a periodic crystal modulation of period ~ 26 Å along the axis of the CuO_2 plane is generated as shown in Fig. 5.3. This crystal supermodulation also induces periodic variations in δ up to 12 % [94] as measured by the single-particle tunnelling spectroscopy as well as the Josephson tunnelling current [33]. However, the influence of this supermodulation on $\mathcal{E}$ and Ψ is still undetermined.

5.3.1 Imaging $\Phi(\mathbf{r})$ and $\delta(\mathbf{r})$

The strategy is to image $\mathcal{E}(\mathbf{r})$ and $\Psi(\mathbf{r})$ directly at the atomic scale, which are varied by the apical distance $\delta(\mathbf{r})$ produced by the crystal supermodulation. In practice, near optimally doped (hole density $p = 17$ %) single crystals of $Bi_2Sr_2CaCu_2O_{8+x}$ are inserted into the STM head right after its cleavage under cryogenic and UHV

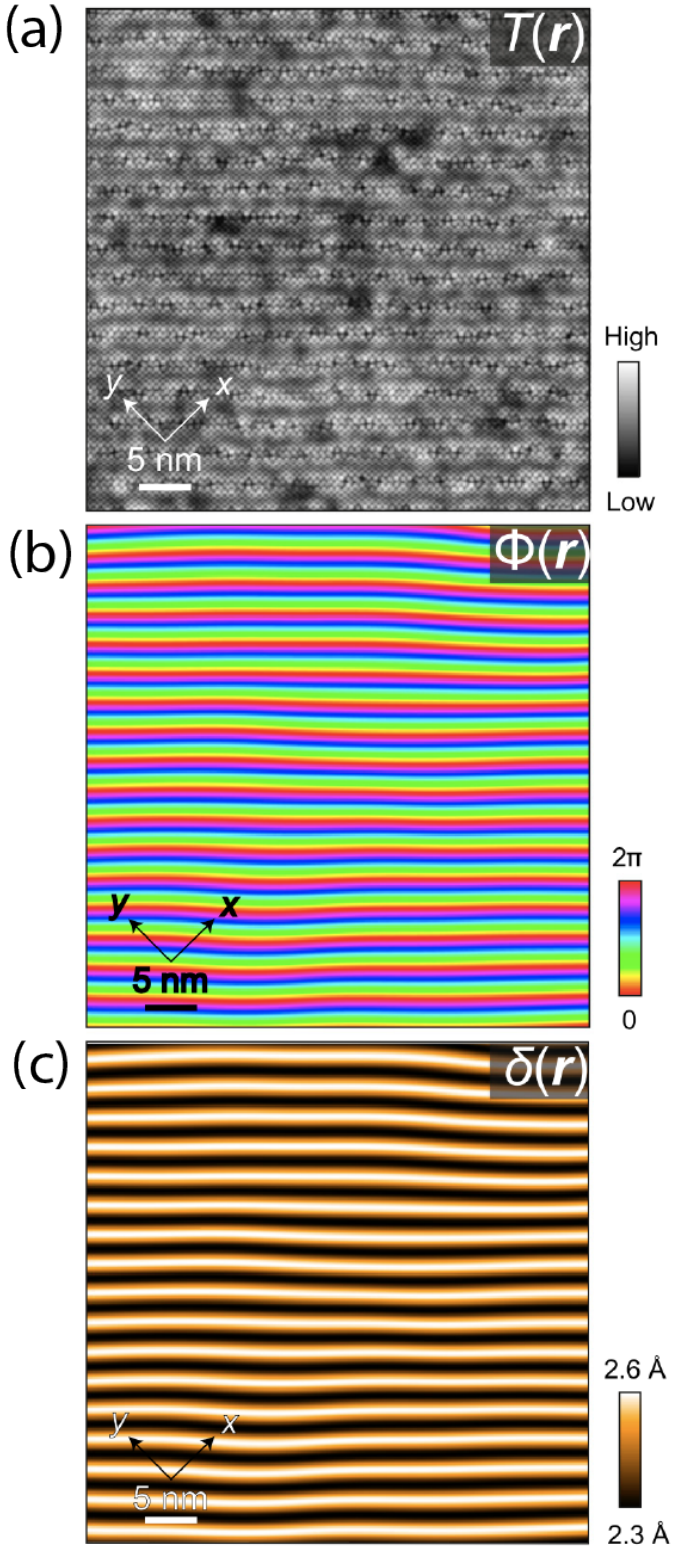

Figure 5.9: (a) Exemplary $Bi_2Sr_2CaCu_2O_{8+x}$ topograph $T(\mathbf{r})$ at the BiO termination layer. The planar $Cu-O$ axes are at 45° to the supermodulation, as shown. The supermodulation runs from top to bottom with wavevector $\mathbf{Q}_s \approx (0.15, 0.15)2\pi/a_0$, obviously with a relatively short correlation length. (b) From (a), the supermodulation phase $\Phi(\mathbf{r})$ is derived. (c) From (b), the apical distance $\delta(\mathbf{r})$ is derived from X-ray refinement data for the $Bi_2Sr_2CaCu_2O_{8+x}$ crystal structure.

conditions to reveal the BiO termination layer shown in Fig. 5.9(a). The CuO plane is around 5 Å beneath the BiO layer, separated by the SrO layer that contains the apical oxygen atoms. To determine the apical distance δ beneath every location $\mathbf{r}$, the supermodulation in the topography $T(\mathbf{r})$ of the BiO surface is first imaged by atomic resolution STM. To the first harmonic, this surface corrugation occurring at the supermodulation wavevector $\mathbf{Q}_s \approx (0.15, 0.15)2\pi/a_0$ can be parametrised by $T(\mathbf{r}) = A(\mathbf{r})\cos\Phi(\mathbf{r})$, where $\Phi(\mathbf{r}) = \mathbf{Q}_s \cdot \mathbf{r} + \theta(\mathbf{r})$ and $\theta(\mathbf{r})$ represents the disorder effects. $\Phi(\mathbf{r})$ is extracted from the Fourier transform of the topographic image $T(\mathbf{r})$ by using the Lock-in technique (Appendix A) as shown in Fig. 5.9(b). The topographic elevation is minimal at $\Phi = \pi$ and maximal at $\Phi = 0$. Then by inferring from Bi-2212 X-ray crystallography data [95], the spatial structure of the apical distance $\delta(\mathbf{r})$ can be related to the $T(\mathbf{r})$ above, which shows that the apical distance is minimal at $\Phi = 0$ and maximal at $\Phi = \pi$ as shown in Fig. 5.10. This is due to the larger supermodulation displacement in the CuO layer compared to its neighbouring SrO layer. Thus, to the first harmonic, the apical distance image can be determined as $\delta(\mathbf{r}) \approx 2.44 - 0.14\cos\Phi$ Å as shown in Fig. 5.9(c).

5.3.2 Measuring $\mathcal{E}$ and Ψ

By using single particle tunnelling spectroscopy, the local density of electronic states $N(\mathbf{r}, E)$ can be determined from the measurement of the differential conductance spectrum $dI/dV(\mathbf{r}, V) \equiv g(\mathbf{r}, V)$ at every location $\mathbf{r}$ as a function of V up to 2 V. As this energy scale is comparable to that of the CuO 3-band model (Eqn. 5.5), this should reveal $\mathcal{E}$ in the tunnelling spectrum at every location $\mathbf{r}$. Lastly, to determine the electron pair condensate Ψ, we measure the electron-pair density $|\Psi|^2 \equiv n_P$ by using SJTM. This is because Ψ is, in general, a complex value and cannot be measured directly. In addition, the energy gap extracted from the single-particle tunnelling spectrum is obscured by the pseudogap, rendering it unsuitable for use as the superconducting gap in lightly hole-doped cuprates.

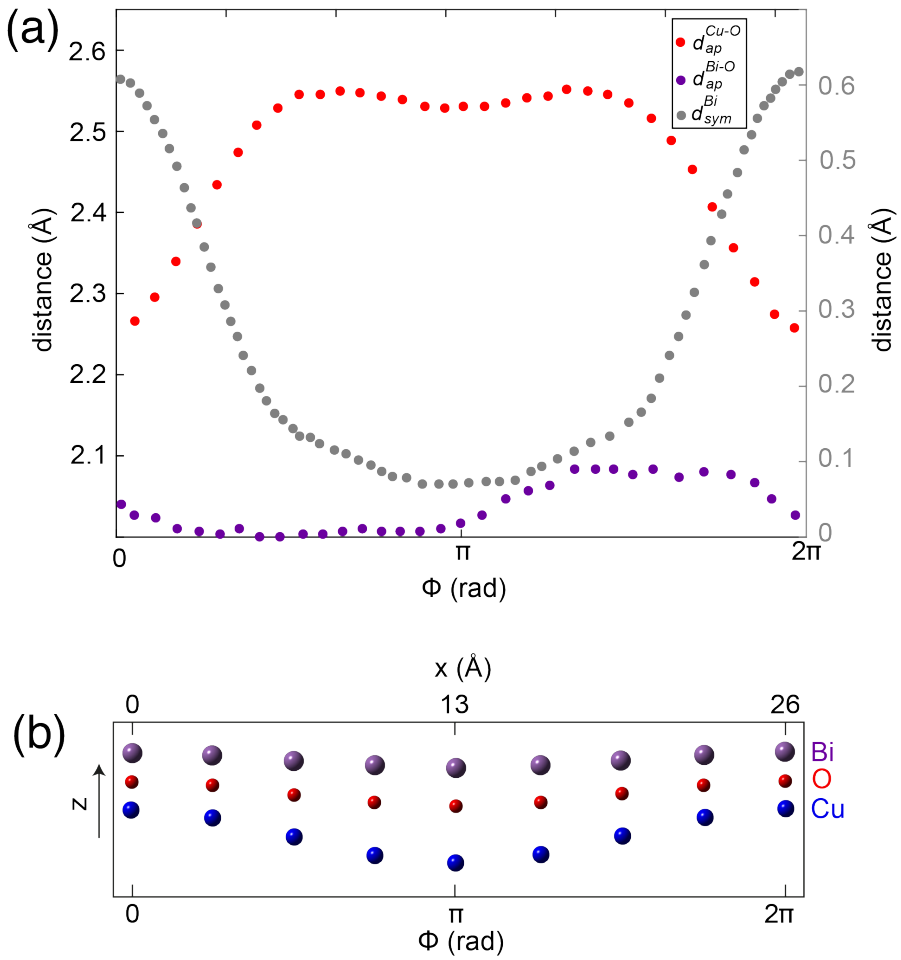

Figure 5.10: (a) Left hand axis: apical Cu-O and Bi-O distances as a function of supermodulation phase (red and purple dots) Φ from [95]. Right-hand axis: displacement of Bi-O termination layer from symmetry plane of crystal as a function of supermodulation phase Φ from X-ray data (gray dots). (b) Schematic showing the atomic modulations induced along the z axis by the supermodulation. The CuO_2 layer modulates with a larger amplitude than the SrO layer, resulting in δ being maximal at $\Phi = \pi$, where the topographic elevation has its minimum.

5.4 Simultaneous visualisation of $\mathcal{E}(\mathbf{r})$ and $\Psi(\mathbf{r})$

To search for the supermodulation induced effects on $\mathcal{E}(\mathbf{r})$, we measure the tunnelling $g(V)$ spectrum at every location $\mathbf{r}$ within the high-voltage range $-1.6\ \text{V} \leq V \leq 2\ \text{V}$ at high junction resistance of $R_N \sim 85\ \text{G}\Omega$ ($V_s = 600\ \text{mV}, I_s = 7\ \text{pA}$), which precludes any tip-induced electric field effect. Two spectra averaged at $\Phi = 0$ (blue) and $\Phi = \pi$ (red) locations in the FOV of Fig. 5.11(a) are shown in Fig. 5.11(b) in logarithmic scale. This clearly shows an exponential growth of density of states at

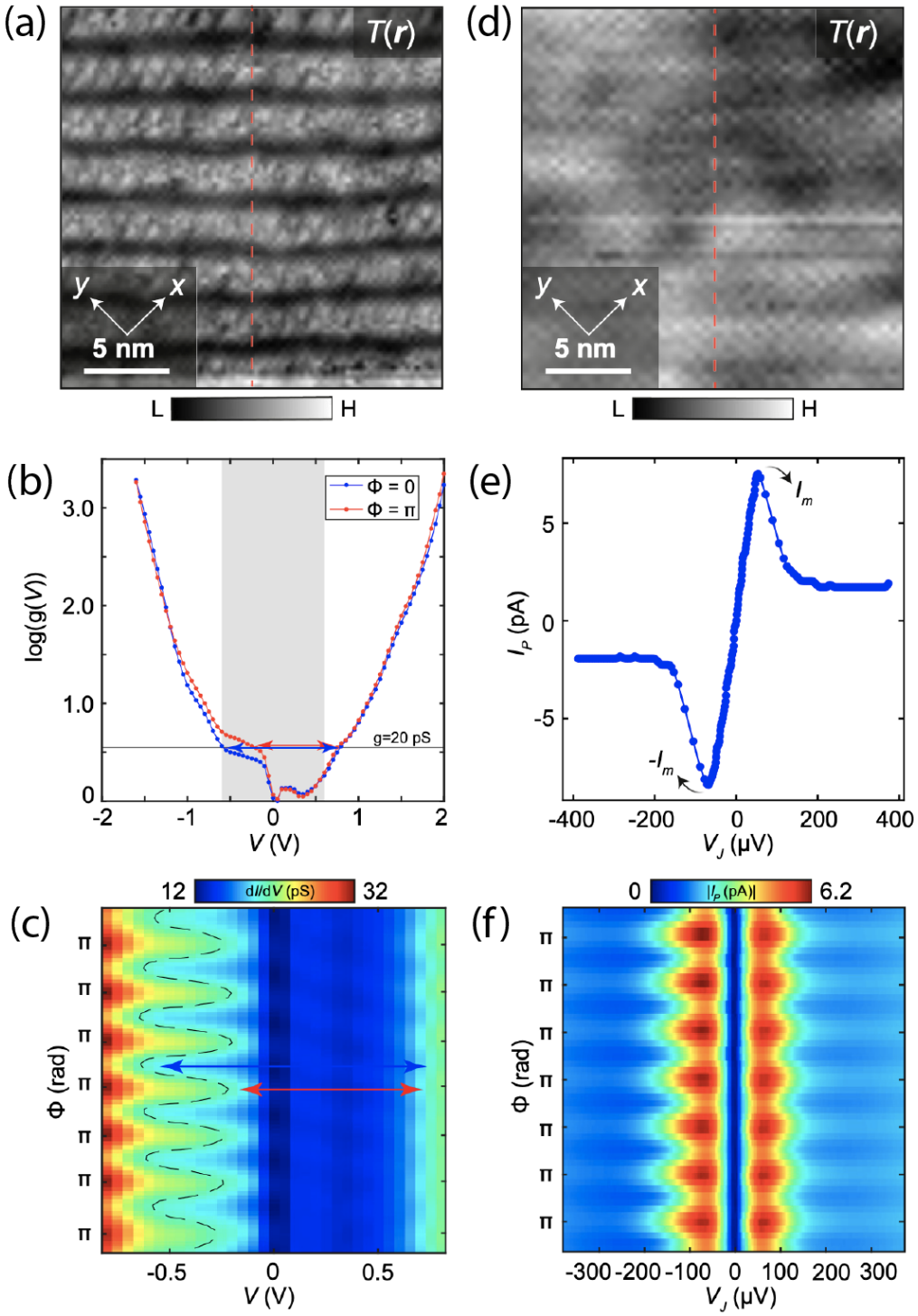

Figure 5.11: (a) Topographic image of BiO termination layer at $T = 4.2$ K, using a nonsuperconducting W-tip. The trajectory of the dashed red line corresponds to the data in (c). (b) $g(V)$ spectra of single-electron tunnelling measured at high-voltage and high tunnel junction resistance $R_N \approx 85\,\mathrm{G\Omega}$ in the FOV of (a) averaged at supermodulation phases $\Phi = 0$ and $\Phi = \pi$. (c) Measured $g(V)$ along the dashed line in (a). Typical examples of $\mathcal{E}(\Phi = 0)$ and $\mathcal{E}(\Phi = \pi)$ indicated by blue and red double-headed arrows, respectively. (d) Topographic image of BiO termination layer at $T = 2.1$ K, using a superconducting tip. The trajectory of the dashed red line corresponds to the data in (f). (e) Typical $I_P\,(V_J)$ spectrum of electron-pair tunnelling measured at low voltage and $R_N \approx 21\,\mathrm{M\Omega}$ in the FOV of (d). (f) Measured $|I_P\,(V_J)|$ along the dashed linecut in (d). For clarity, (c) and (f) have been Fourier filtered at the crystal supermodulation wavevector.

the gap edges of upper and lower bands, revealing the charge-transfer gap. I then use the standard method to estimate $\mathcal{E}$ as the minimum energy difference between the valence and conduction bands at a constant conductance $G \approx 20$ pS, as indicated by the double-headed arrows (appendix B). The extracted $\mathcal{E}$ value is consistent with the charge-transfer energy $\mathcal{E} \approx 1.2$ V measured by other techniques mentioned in section 5.2.3. The choice of the conductance value $G \approx 20$ pS has several reasons. First, this avoids disorder in the density of states caused by the oxygen dopants around $V = 0.9$ V. Second, $\mathcal{E}(G, \mathbf{r})$ extracted from different values of G ranging from 20 pS to 80 pS exhibit similar spatial structure (Fig. B.2). Furthermore, the spatial modulation pattern in $\mathcal{E}(G, \mathbf{r})$ at the supermodulation wavevector $\mathbf{Q_s}$ is independent of the choice of G as shown in the power spectral density Fourier transform $\mathcal{E}(G, \mathbf{q})$. This indicates that the $\mathcal{E}(\Phi)$ relation will stay qualitatively unchanged for a range of G, but with different amplitude variations in $\mathcal{E}$. To reveal the $\mathcal{E}(\mathbf{r})$ modulation more explicitly, Fig. 5.11(b) shows a contour plot of $g(\mathbf{r}, V)$ along the red dashed line in Fig. 5.11(a), directly revealing that $\mathcal{E}(\mathbf{r})$ modulates at $\mathbf{Q_s}$ with $\mathcal{E}(\Phi = 0) \approx 1.35$ eV (blue arrow) and $\mathcal{E}(\Phi = \pi) \approx 0.95$ eV (red arrow).

Similarly, Fig. 5.11(d) shows a topographic image measured with a superconducting nano flake tip. To visualise supermodulation-induced variations in $n_P(\mathbf{r})$, we measure the tunnelling current spectrum in the μV range with a normal state junction resistance $R_N \sim 21$ MΩ. Fig. 5.11(e) shows a typical tunnelling current spectrum measured at 45 mK which exhibits the phase-diffusive behaviour with pair tunnelling current $I_p(V)$ expressed in Eqn. 2.45. As introduced in chapter 2, n_P can be extracted by identifying the maximum of the pair-tunnelling current I_m and using the relation $n_P(\mathbf{r}) \propto I_m(\mathbf{r})R_N^2(\mathbf{r})$ or equivalently $n_P(\mathbf{r}) \propto g_0(\mathbf{r})R_N^2(\mathbf{r})$. The modulations in $n_P(\mathbf{r})$ can be visualised by plotting $I_p(\mathbf{r}, V)$ along the red dashed line in Fig. 5.11(f) in the direction of $\mathbf{Q}_s$. This contour plot clearly demonstrates modulations of the $I_m(\mathbf{r})$ at wavevector $\mathbf{Q}_s$.

Next, I will present a quantitative description of the modulations of $\mathcal{E}(\mathbf{r})$ and $n_P(\mathbf{r})$ at $\mathbf{Q_s}$. Starting with two FOVs with their topographic images $T(\mathbf{r})$ shown in Fig. 5.12(a) and Fig. 5.12(b). In Fig. 5.12(a), $T(\mathbf{r})$ is simultaneous to the high

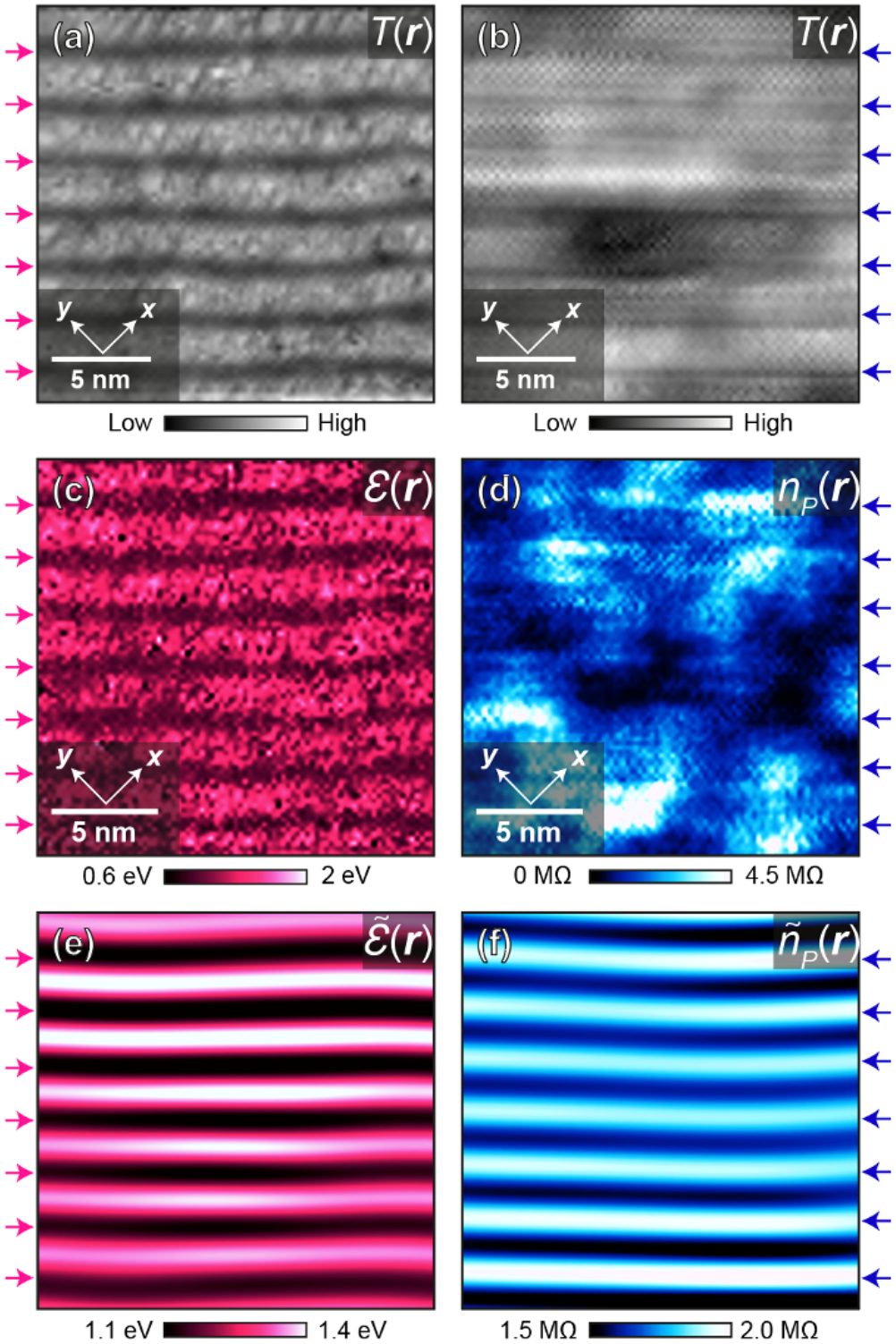

Figure 5.12: (a) Topographic image $T(\mathbf{r})$ simultaneous with high-voltage $g(\mathbf{r}, V)$ measured at $R_N \approx 85\,\mathrm{G\Omega}$, yielding (c). The pink arrowheads are at supermodulation $\Phi = \pi$. (b) Topographic image $T(\mathbf{r})$ simultaneous with low-voltage $I_P\,(\mathbf{r}, V_J)$ and $R_N(\mathbf{r})$ maps, yielding (d). The blue arrowheads are at $\Phi = \pi$. (c) Measured $\mathcal{E}(\mathbf{r})$ in the FOV of (a). The mean value is $\mathcal{E} = 1.195$ eV. The pink arrowheads are at $\Phi = \pi$ of the supermodulation. (d) Measured $n_P(\mathbf{r})$ in the FOV of (b). The blue arrowheads are at $\Phi = \pi$. (e) Fourier filtered $\tilde{\mathcal{E}}(\mathbf{r})$ at supermodulation wavevectors $\pm\mathbf{Q}_s$ in the FOV of (a) and (c). The pink arrowheads are at $\Phi = \pi$. (F) Fourier filtered $\tilde{n}_P(\mathbf{r})$ at supermodulation wavevectors $\pm Q_s$ in the FOV of (b) and (d). The blue arrowheads are at $\Phi = \pi$.

voltage $g(\mathbf{r}, V)$ measurements. Fig. 5.12(b) is taken using the superconducting nanoflake tip and is simultaneous to the $I_p(\mathbf{r}, V)$ measurements. Both topographic images are analysed to extract the supermodulation phase $\Phi(\mathbf{r})$. The red and blue arrows indicate $\Phi = \pi$ phase of Fig. 5.12(a) and Fig. 5.12(b), respectively. A high-voltage, single particle tunnelling $g(\mathbf{r}, V)$ map is measured at $R_N \approx 85$ GΩ and $T = 4.2$ K in the same FOV of Fig. 5.12(a). The resulting $\mathcal{E}(\mathbf{r})$ image is presented in Fig. 5.12(c) by measuring the energy difference between the top of the valence band and the bottom of the conducting band at a constant conductance $G = 20$ pA. The modulation at $\mathbf{Q_s}$ appear to have little difference if $\mathcal{E}(\mathbf{r})$ is estimated at the range 20 pS $\leq V \leq 80$ pS. Concomitantly, a low-voltage, electron-pair tunnelling $I_p(\mathbf{r}, V)$ map is measured at $R_N \approx 21$ MΩ and $T = 2.0$ K in the same FOV of Fig. 5.12(b). The $n_P(\mathbf{r})$ image in Fig. 5.12(d) is obtained by multiplying $g_0(\mathbf{r}) \equiv g(\mathbf{r}, 0)$ with $R_N^2(\mathbf{r})$, both of which are measured in the same FOV as in Fig. 5.12(b). The normal state junction resistance R_N is calculated by self-normalising two sets of $g(V)$ spectra, one for $V_{\max} < \Delta/e$ and the other for $V_{\max} > \Delta/e$ (Appendix C). Lastly, Fourier filtering both $\mathcal{E}(\mathbf{r})$ and $n_P(\mathbf{r})$ images at $\mathbf{Q_s}$ reveals the supermodulation induced first-harmonic modulations $\tilde{\mathcal{E}}(\mathbf{r})$ and $\tilde{n}_P(\mathbf{r})$ in Fig. 5.12(e) and Fig. 5.12(f).

5.5 Towards the mechanism of electron-pairing

5.5.1 Relationship between n_P and $\mathcal{E}$

Next, we seek to quantify the effect of the supermodulation displaced apical distance δ on the charge-transfer energy $\mathcal{E}$ and the electron-pair density n_P at each planer Cu atom. First, the apical distance is plotted against the supermodulation phase shown by the grey dots in Fig. 5.13(b). Then by the corresponding simultaneous measurements $\Phi(\mathbf{r}) : \mathcal{E}(\mathbf{r})$, the image of the charge transfer energy $\mathcal{E}$ is Fourier filtered near the wavevectors $\pm\mathbf{Q}_s$ and $\mathcal{E}(\Phi)$ is plotted by the red dots in Fig. 5.13(b) where it is normalised to its mean value. Similarly, according to the simultaneous measurements of $\Phi(\mathbf{r}) : n_P(\mathbf{r})$, the electron-pair density n_P is Fourier filtered near the wavevectors $\pm\mathbf{Q_s}$ and $\bar{n}_P(\Phi)$ is plotted by the blue dots in Fig. 5.13(b) where it is normalised to its mean value. In the data analysis, I use a

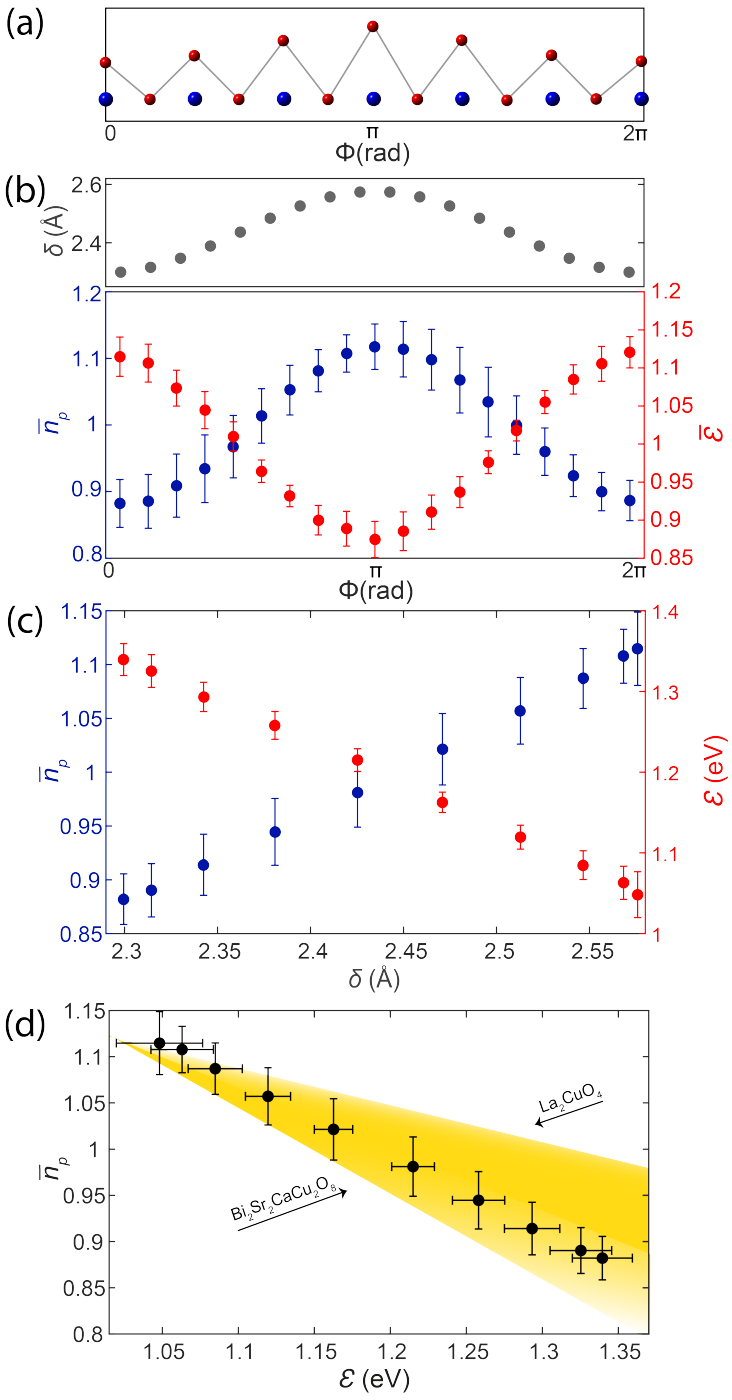

Figure 5.13: (a) Schematic of planar Cu to apical O distance modulations $\delta(\mathbf{r})$ in Bi-2212 shown versus supermodulation phase Φ. (b) Gray dots: $\delta(\Phi)$ showing the displacement of the apical oxygen atom within the CuO_5 pyramid versus supermodulation phase Φ. Red dots: measured $\overline{\mathcal{E}}(\Phi)$ showing the typical value for the Cu-O charge-transfer energy $\mathcal{E}$ for each value of the supermodulation phase Φ normalised to the mean value of $\mathcal{E}$. These data are from the same FOV as Fig. 5.12(a),(c) and (e). Blue dots: measured $\bar{n}_P(\Phi)$ showing the measured value of electron-pair density versus supermodulation phase Φ. (c) Measured dependence of Cu-O charge-transfer energy $\mathcal{E}$ and electron-pair density n_P on the displacement δ of the apical O atoms from the planar Cu atoms. (d) Measured relationship of electron-pair density $\bar{n}_P$ to the Cu-O charge-transfer energy $\mathcal{E}$ in the CuO_2 plane of Bi-2212. The yellow shaded region shows the range of predicted slopes for $d\bar{n}_P/d\mathcal{E} \equiv -\alpha\,\mathrm{eV}^{-1}$, as $0.3 \leq \alpha \leq 1.0\,\mathrm{eV}^{-1}$ from DMFT calculations with the parameter limits reported for La_2CuO_4 and $Bi_2Sr_2CaCu_2O_x$, as indicated by black arrows.

$\mathcal{E}(\mathbf{r})$ FOV that has 7 periods of supermodulation and a $n_P(\mathbf{r})$ FOV that has 13 periods. Next, the relation between $\mathcal{E}$ and δ and between n_P can be determined by eliminating the common variable Φ which results in Fig. 5.13(c). The slopes in Fig. 5.13(c) give $\frac{d\mathcal{E}}{d\delta} \approx -1.04 \pm 0.12$ eV/Å and $\frac{d\bar{n}_P}{d\delta} \approx 0.85 \pm 0.22$ Å^{-1} for Bi-2212, which provides quantitative evidence of the characteristics of cuprate electronic structure. Finally, by eliminating the common variable Φ, the fundamental atomic relationship between the charge-transfer energy $\mathcal{E}$ and the electron-pair density $\bar{n}_P$ is plotted in Fig. 5.13(d), which shows that $\frac{d\bar{n}_P}{d\mathcal{E}} \approx -0.81 \pm 0.17$ eV^{-1} or equivalently $\frac{d|\overline{\langle c_\uparrow c_\downarrow \rangle}|}{d\mathcal{E}} \approx -0.40 \pm 0.09$ eV^{-1}. Here, the apical distance is analogous to the 'isotope effect' in conventional BCS superconductors, where it varies the strength of the charge transfer energy and, in turn, the superexchange interaction, which ultimately alters the electron-pair condensate.

5.5.2 Comparison with c-DMFT predictions

The relationship between Ψ and $\mathcal{E}$ has been predicted by numerical study of the 3-band Hubbard model using the c-DMFT technique introduced in the previous chapter. The predicted values of $\alpha = dn_P/d\mathcal{E}$ can be extracted and then compared to the experimental result shown in Fig. 5.13(d). However, in the experiments, the proportionality constant that relates $g_0 R_N^2$ to n_P is unknown, and the comparison between $g_0 R_N^2$ and $n_P = |\Psi|^2$ is meaningless. Therefore, both the experimentally measured and theoretically predicted values need to be normalised consistently. To achieve this, experimentally acquired value $g_0 R_N^2$ at each atomic position is averaged to its mean value across the entire experimental FOV, i.e.

$$\bar{n}_P = \frac{g_0 R_N^2}{\langle g_0 R_N^2 \rangle}. \tag{5.23}$$

The pairing amplitude $|\Psi|$ calculated from c-DMFT is normalised to its reference value for the so-called covalent case $|\Psi|_{\text{cov}} = 0.0774$, whose input parameters are based on Bi-2212. This procedure can be shown as

$$\left|\overline{\langle c_\uparrow c_\downarrow \rangle}\right|^{\text{Bi-2212}} = \frac{|\Psi|}{|\Psi|_{\text{cov}}}. \tag{5.24}$$

Similar normalisation is applied to the calculated c-DMFT results for La_2CuO_4 [79]

$$\left|\overline{\langle c_\uparrow c_\downarrow \rangle}\right|^{\mathrm{LSCO}} = \frac{|\Psi|}{|\Psi|_{\mathrm{LSCO}}} \tag{5.25}$$

where $|\Psi|_{\mathrm{LSCO}} = 0.0154$. The yellow shaded triangular region in Fig. 5.13(d) represents c-DMFT predictions of the direct response of the electron-pair condensate on the alteration of the charge-transfer energy, namely, $\frac{d\bar{n}_P}{d\mathcal{E}} \approx -\alpha$ eV^{-1}, with α in the range $0.3 \leq \alpha \leq 1.0$ for material parameters ranging from La_2CuO_2 to $Bi_2Sr_2CaCu_2O_8$. Specifically for $Bi_2Sr_2CaCu_2O_8$, the three-band CuO_2 Hubbard model based c-DMFT calculation for the superexchange mediated electron-pairing mechanism yields $\frac{d|\overline{\langle c_\uparrow c_\downarrow \rangle}|}{d\mathcal{E}} \approx -0.46 \pm 0.05$ eV^{-1} or equivalently $\alpha \approx 0.93 \pm 0.1$ eV^{-1}, which agrees quantitatively with the experimental measurements presented in Fig. 5.13(d).

5.6 Summary and outlook

Taken all together, the anti-correlation between the charge-transfer energy $\mathcal{E}$ and the electron-pair density n_P directly suggests that the charge-transfer superexchange interaction is key to the electron-pairing mechanism in 17% hole-doped cuprate superconductor $Bi_2Sr_2CaCu_2O_{8+x}$. To further test this mechanism across the $Bi_2Sr_2CaCu_2O_{8+x}$ phase diagram, future experiments can measure $\left|\frac{d\bar{n}_P}{d\mathcal{E}}\right|$ as a function of hole-doping level. If successful, the result will directly validate that the *charge transfer superexchange* mechanism is universally responsible for superconductivity in the cuprates. The proposed experiments can be challenging. On one hand, in previous studies, a nanometer scale flake had to be picked up by the scanning tip to achieve electron-pair tunnelling into cuprates. This technique works successfully but is technically challenging, unreliable and with limited atomic resolution. On the other hand, to measure the charge-transfer energy, one needs to measure the single-particle tunnelling spectrum up to two volts and at a junction resistance of GΩ, which requires extreme stability of the STM. The Gemini STM described in Chapter 2 is ideal for carrying out these experiments. With its superior mechanical stability and milli-kelvin temperature, it is capable of imaging

electron-pair density using a Niobium tip with far better atomic resolution and stable high-voltage spectroscopic imaging.

6

Visualising exciton crystal at atomic scale

Contents

Like Cooper pairs, excitons are composite bosons made of electron-hole pairs predicted to exhibit macroscopic condensation. 1T-TiSe$_2$ is known to host an unconventional charge-density wave (CDW) state hypothesized to result from exciton condensation. This chapter reports my recent spectroscopic imaging STM experiments of 1T-TiSe$_2$[1] that directly reveal the charge-transfer process between the Se and Ti atoms, which is responsible for exciton formation. Further, direct imaging of the excitonic energy gap shows a highly heterogeneous spatial pattern inconsistent with a conventional Peierls CDW but indicates strong electron-electron interactions.

[1]The data analysis presented in this chapter utilized the Python package STMPY available at `https://github.com/harrispirie/stmpy`.

6.1 Concept of exciton condensate

6.1.1 A distinct type of composite boson

Below a certain transition temperature T_c, Bose-Einstein condensation leads to remarkable macroscopic quantum phenomena such as superconductivity and superfluidity, in which the composite bosons condense into the ground state. Here, ^{4}He atoms and Cooper pairs are examples of composite bosons that are made of an even number of fermions and are categorised as type I bosons by Kohn and Sherrington [96]. In contrast to type I bosons, fermion and its hole can also form a bound pair which is the type II boson. A particular example is the bound electron-hole pair called the exciton.

The exciton and its condensate exhibit distinct properties as compared to Cooper-pairs described in Chapter 1. Particularly, the condensation of excitons possesses neither superfluidity nor ODLRO. Instead, diagonal long-range order (DLRO) is present that signifies a change of real-space long-range order such as the formation of a superlattice. For example, in a two-band solid where the valence band maximum is peaked at $\mathbf{k} = \mathbf{0}$ and the conduction band has its minimum at wavevector $\mathbf{q}$, the one-particle density is predicted to be oscillating at non-zero wavevector $\mathbf{q}$, generating a charge density wave. In this case, the wavefunction for a single exciton can be written as [96]

$$\Psi_1 = \left(1/\Omega^{1/2}\right) \sum_{\mathrm{k}} f(\mathbf{k}) c^{\dagger}_{1,\mathbf{k}+\mathbf{q}} c_{0,\mathbf{k}} \Psi_0 \tag{6.1}$$

where $\Psi_0 = \prod_{\mathbf{p}} c^{\dagger}_{0,\mathbf{p}} \Psi_{\mathrm{vac}}$ is the fully occupied insulating ground state, $n = 0$ denotes the valence band and $n = 1$ is the conduction band, $c^{\dagger}(c)$ is the electron creation (annihilation) operator, Ω is the system volume and $f(\mathbf{k})$ is the internal pair form factor. A condensation of N excitons into the insulating ground state Ψ_0 is then described by

$$\Psi_N \approx \left(B_{\mathrm{k}}{}^{\dagger}\right)^N \Psi_0, \tag{6.2}$$

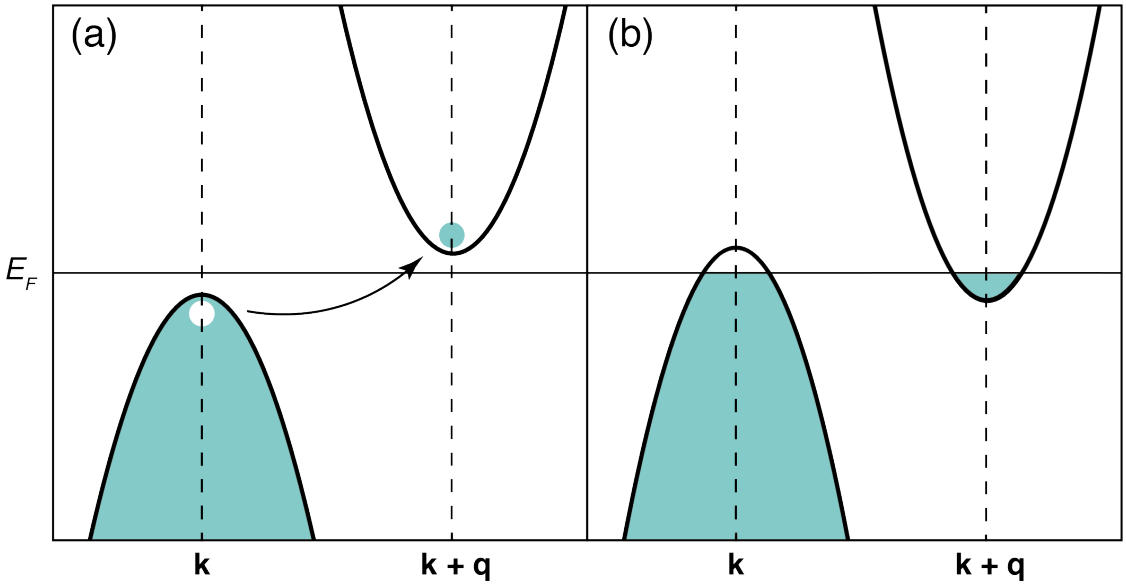

Figure 6.1: Band structure schematics for a two-band solid with an indirect bandgap E_G in the normal state ($T > T_c$). (a) the semiconductor case. (b) The semimetal case.

where ${B_{\mathbf{q}}}^{\dagger} = \left(1/\Omega^{1/2}\right) \sum_{\mathrm{k}} f(\mathbf{k}) c^{\dagger}_{1,\mathbf{k}+\mathbf{q}} c_{0,\mathbf{k}}$ is the exciton creation operator. This suggests that the condition, $\left\langle {B_{\mathrm{q}}}^{\dagger} \right\rangle \neq 0$, ensures the following relation

$$\left\langle c^{\dagger}_{1,\mathbf{k}+\mathbf{q}} c_{0,\mathbf{k}} \right\rangle \neq 0. \tag{6.3}$$

This results in $\mathbf{q}$ being a multiple of the reciprocal lattice vector [97].

Previously, signatures of excitonic condensation phases have been observed in many systems. For example, the excitonic superfluid, as shown in the semiconductor quantum Hall bilayer systems [98], or the localised excitons in an excitonic insulator $1T$-$TiSe_2$ [99]. Despite these encouraging achievements, no experiments have directly visualised excitons at the atomic scale. In this Chapter, I will present my attempt to directly visualise exciton condensates in the CDW phase of $1T$-$TiSe_2$ by using the spectroscopic imaging STM I built during my DPhil.

6.1.2 Formation of the excitonic insulating phase

In the picture of a two-band solid with a bandgap E_G, interband Coulomb interaction can lead to exciton condensation during a transition from a small band-gap semiconductor to a semimetal with small band-overlap (Fig. 6.1) [97]. For simplicity,

consider a semiconductor with a direct band gap, analogous to the BCS theory; the excitonic order parameter can be defined as [100]

$$\Delta(\mathbf{k}) \equiv -\frac{1}{\Omega}\sum_{\mathbf{k}'} V\left(\mathbf{k}-\mathbf{k}'\right)\left\langle c^{\dagger}_{1,\mathbf{k}'}c_{0,\mathbf{k}'}\right\rangle \tag{6.4}$$

where V describes the Coulomb interaction, 0 denotes the valance band, and 1 denotes the conduction band. The occurrence of exciton condensation means that $\left\langle c^{\dagger}_{1,\mathbf{k}}c_{0,\mathbf{k}}\right\rangle \neq 0$. This leads to a finite gap value $\Delta(\mathbf{k}) \neq 0$, rendering the system insulating.

In the semiconductor case (Fig. 6.1(a)), when the band gap E_G is larger than the exciton binding energy E_B, no excitons are formed ($\Delta = 0$). Decreasing E_G until $0 < E_G < E_B$, the system transitions to the excitonic phase as the Fermi surface becomes unstable to the formation of excitons whose condensation leads to a new insulating state. Further decreasing E_G until it crosses over the Fermi level, the normal state is a semimetal with a negative band gap (Fig. 6.1(b)). Assuming the overlap between the two bands is small and E_G is restricted to $E_c < E_G < 0$, the screening effect of the Coulomb attraction is weak between an electron and its hole due to low carrier density, which favours exciton formation. The semimetal ground state is thus unstable to the spontaneous formation of excitons [97]. Further decreasing E_G until the two bands are deeply overlapped, i.e. $E_G < E_c$, the screening effect is too strong to have exciton condensation. In conclusion, excitonic phases can emerge from the semiconductor to semimetal transition below a certain temperature T_c when the band gap is within the range $E_c < E_G < |E_c| = E_B$. Fig. 6.2 shows the resulting phase diagram. The semiconducting region has no screening effect, so the excitons are tightly bound stable objects of the BEC type. In the semimetal region, band-overlaps give way to the screening effect where the excitonic phase can be approximated to the BCS type [100].

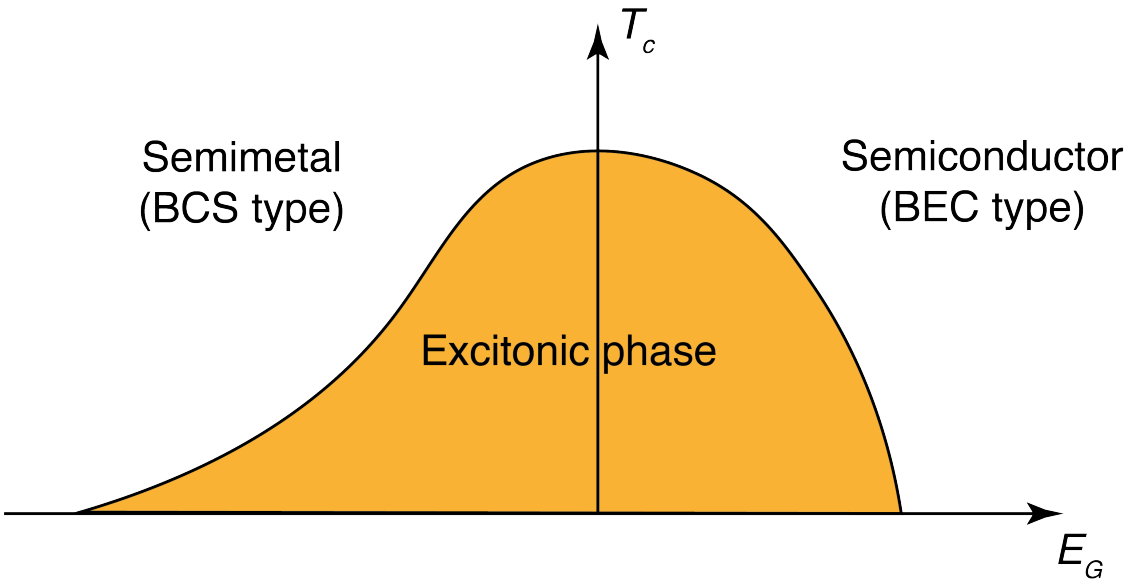

Figure 6.2: Phase diagram for the semiconductor-to-semimetal phase transition. Figure adapted from [100].

6.2 SI-STM measurements of 1T-TiSe$_2$

6.2.1 The excitonic insulator

1T-TiSe$_2$ is a member of the transition-metal dichalcogenide (TMD) family with a 1T polytype crystal structure (Fig. 6.3(a)). This layered material is interconnected by weak Van der Waals bonds, making it easy to cleave. Historical predictions [101] suggest that, below a specific temperature, 1T-TiSe$_2$ behaves as an exciton insulator due to its distinctive band structure with a small band gap magnitude. Whether this compound is a semimetal [102] or a semiconductor [103] is debated. These excitons are believed to form between the top of the Se-4p band and the bottom of the Ti-3d band, separated by the wavevector $\mathbf{q}_0$ (Fig. 6.3(b)). At approximately 200 K, 1T-TiSe$_2$ undergoes a second-order phase transition to a commensurate 2 $\times$ 2 $\times$ 2 charge-density wave (CDW) with wavelength $2\pi/|\mathbf{q}_0|$, as evidenced by heat capacity and resistivity measurements [104, 105]. In the CDW phase, the band structure is modified as both the Se valance band and the Ti conduction band are backfolded with accompanying spectral weight transfer and an opening of an energy gap near the Fermi level (Fig. 6.3(c)).

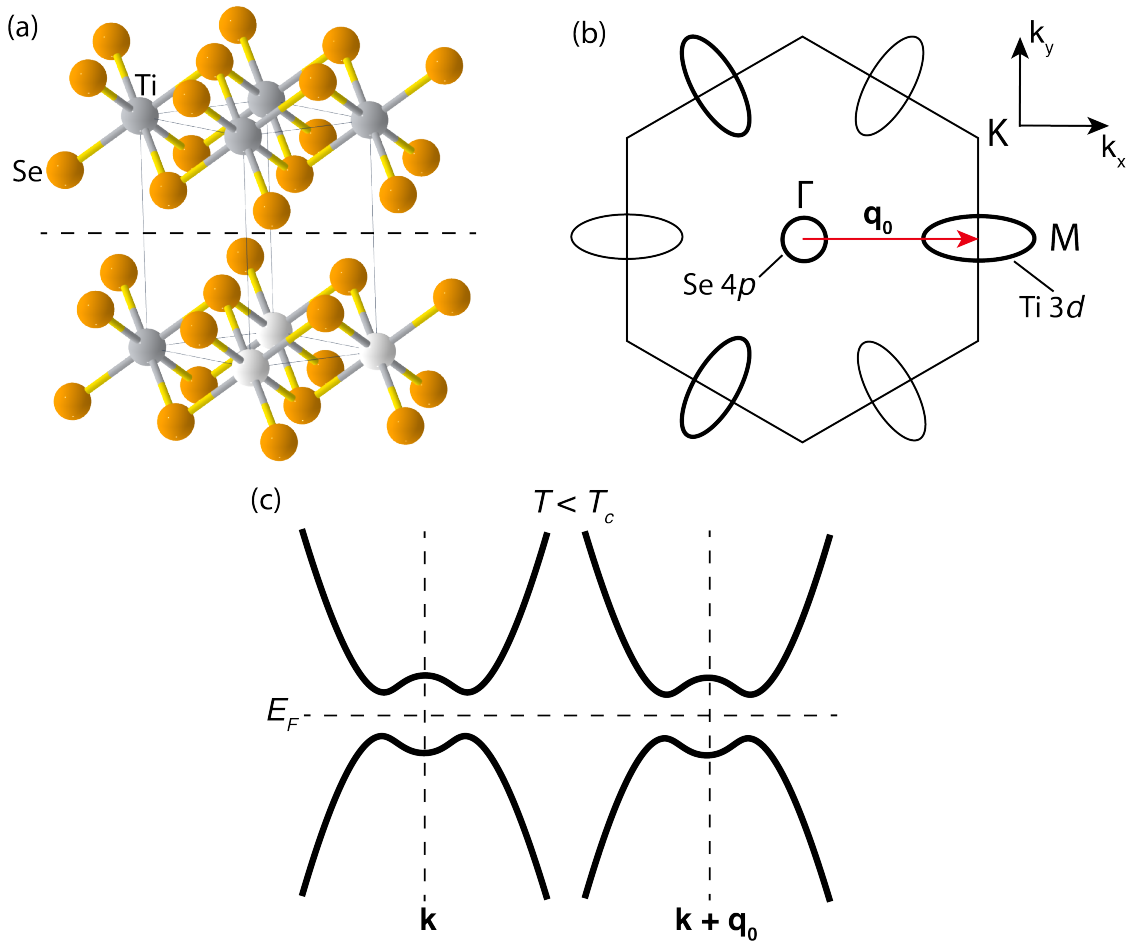

Figure 6.3: Crystal and electronic structure of 1T-$TiSe_2$. (a) Crystal structure of the 1T polytype. The dashed line shows the cleaving plane. Orange sphere: Se atom. Grey sphere: Ti atom. (b) Schematic of the Fermi surface shown within the first Brillouin zone (BZ). The Se valence band is at the Γ point, and the elliptical Ti conduction band is at the BZ boundary (M point). (c) Schematic of the electronic structure in the excitonic phase. Compared with the normal state structure in Fig. 6.1, both bands are backfolded onto each other, and an energy gap opens at the Fermi level. Spectral weight transfer also exists, which is not shown here.

The mechanism of the CDW formation in 1T-$TiSe_2$ is distinct from the conventional Peierls CDW where electron-phonon interaction is dominant. One of the reasons is that the Fermi surface is too small to have any nesting effects. Instead, the nature of the CDW formation is hypothesized to result from a pure electronic origin, i.e. exciton condensation driven by inter-band Coulombic interactions [106]. Bound pairs of the electrons from the Ti-3d band and the holes from the Se-4p band can condense into the ground state and crystallize into the CDW formation. Indeed,

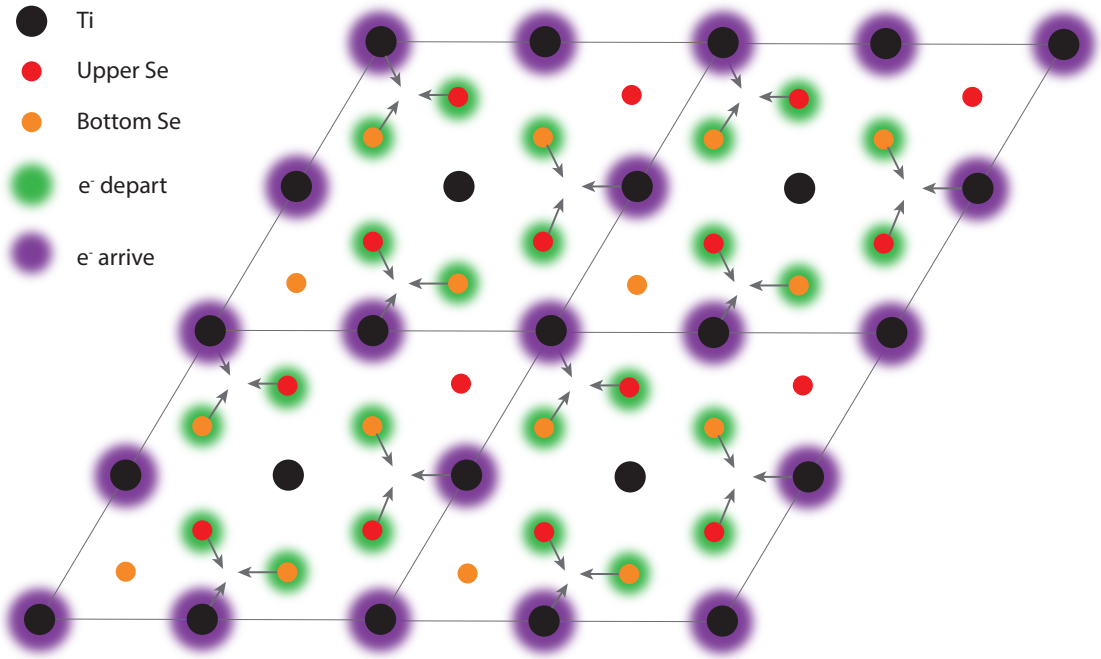

Figure 6.4: Schematic of charge-transfer pattern in $1T$-$TiSe_2$ as viewed from the top of the c axis. Grey arrows indicate directions of atomic displacements. Solid grey lines mark the CDW unit cell boundaries. Figure inferred from Peng et al. [108].

BCS-type theoretical calculations based on sole electronic correlation (no lattice effects) match well with ARPES results [107]. Furthermore, just as the diminishing of a phonon mode at the CDW transition signifies the electron-phonon coupling in a Peierls CDW, a recent experiment demonstrates an electronic plasmon mode softening at the CDW transition in $1T$-$TiSe_2$ [99], which strongly suggests that exciton condensation plays the central role. Thus, using STM, I aim to search for direct evidence of exciton condensates by atomic-scale visualisation.

6.2.2 Imaging localised exciton condensate

I studied the bulk $1T$-$TiSe_2$ crystal with a tungsten tip using the Gemini STM described in Chapter 3. In practice, the crystal is cleaved in cryogenic ultra-high vacuum conditions to reveal the Se layer and then directly inserted into the STM head. All measurements are taken at $T = 13$ K. A typical STM topographic image measured at $T \ll T_c$ is shown in Fig. 6.5(a), which clearly shows CDW modulations with wavelength $2a_0$ (a_0 is the unit cell length) in the three directions separated by

60 degrees. Typical $\mathrm{d}I/\mathrm{d}V$ spectra are shown in Fig. 6.5(b), which directly reveals an energy gap of about 100 meV near the chemical potential.

Visualising exciton charge-transfer

In momentum space, it is evident from ARPES experiments that there exists spectral weight transfer at the CDW transition from the top of the Se valence band at the Γ point to the bottom of the Ti conduction bands at Brillouin zone boundaries [107]. Such a spectral weight transfer can be understood in real space as the electron transfer from the Se atoms to the Ti atoms, equivalent to creating electron-hole pairs (excitons). The triple-Q CDW is accompanied by lattice displacement, resulting in the shortening or extension of Ti-Se bonds. This gives charge accumulation and depletion at different atomic sites [108]. A schematic of the real-space charge-transfer picture viewed from the top of the lattice c axis is shown in Fig. 6.4.

At 13 K, differential conductance spectra $g(V) = \mathrm{d}I/\mathrm{d}V(V)$ are measured from -200 mV to 200 mV at every atomic position $\mathbf{r}$. To get the spectral weight for the valence (conduction) band, each differential conductance spectrum is integrated from -50 mV to -150 mV (0 mV to 50 mV), yielding the following two quantities

$$\mathrm{ST}_v(\mathbf{r}) = \int_{-100\mathrm{mV}}^{-150\mathrm{mV}} g(\mathbf{r}, E)\, dE, \tag{6.5}$$

$$\mathrm{ST}_c(\mathbf{r}) = \int_{0\mathrm{mV}}^{50\mathrm{mV}} g(\mathbf{r}, E)\, dE, \tag{6.6}$$

where ST_v (ST_c) denotes the valence (conduction) band spectral weight. The integration energy range is approximated from ARPES experiments [107]. The spectral weight images for both the filled and empty states are shown in Fig. 6.6(b), (c), respectively. To better visualise the atomic spectral weight transfer, the two images in Fig. 6.6(b), (c) are superimposed to yield the total spectral weight transfer image $\mathrm{ST}(\mathbf{r})$ via the relation $\mathrm{ST}(\mathbf{r}) = \mathrm{ST}_v(\mathbf{r}) + \alpha\mathrm{ST}_c(\mathbf{r})$ where α is the scaling factor, which is shown in Fig. 6.7. In $\mathrm{ST}(\mathbf{r})$, red colour indicates electron depletion and blue colour indicates electron accumulation.

For a more detailed examination of the inter-atomic charge transfer, the CDW unit cell is averaged over the entire FOV and is shown in Fig. 6.9(a) by the black

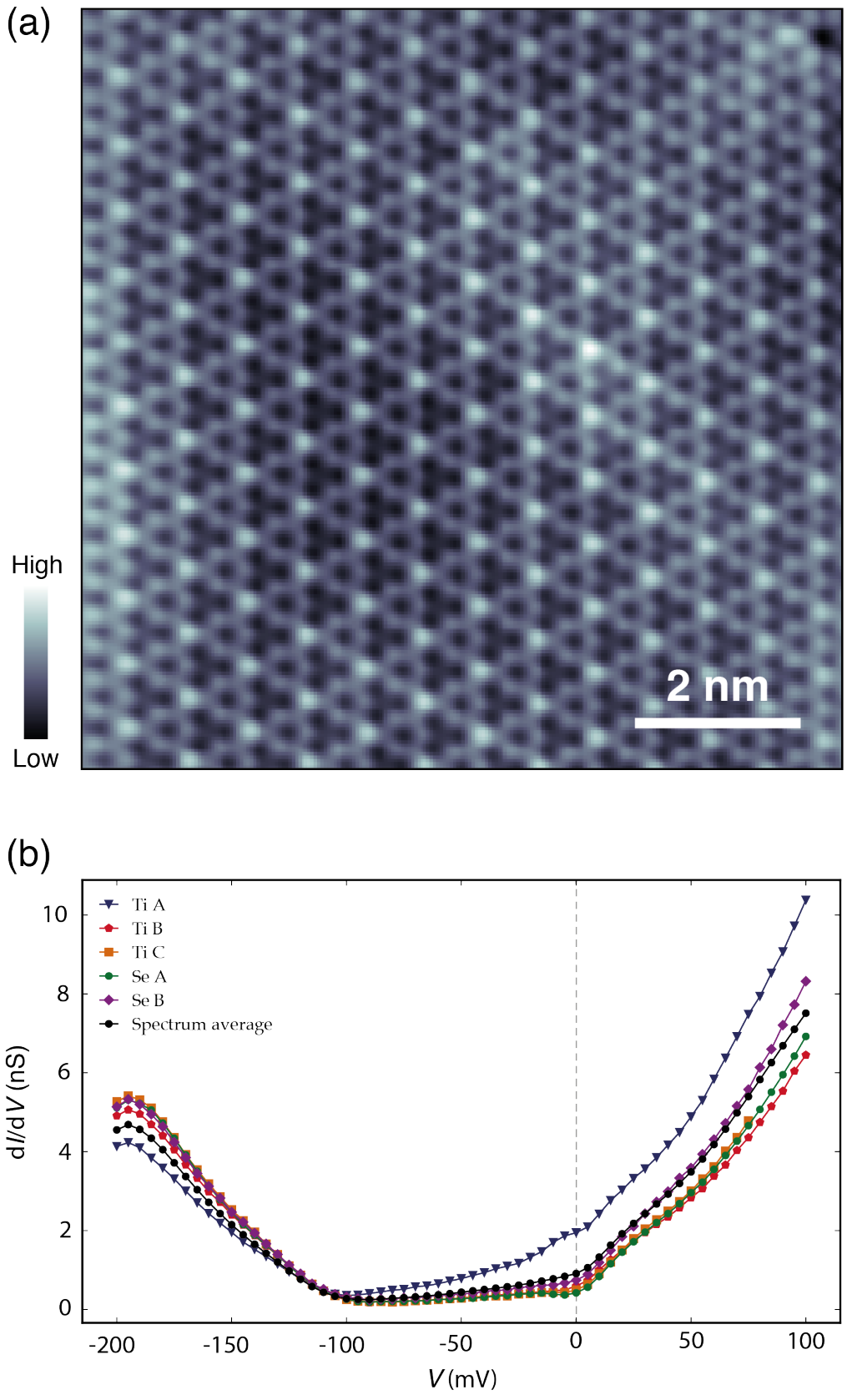

Figure 6.5: (a) Topographic image of $1T$-$TiSe_2$ showing the Se surface. The 2×2 CDW is evident. Set-up condition: $V_s = 200$ mV, $I_s = 50$ pA. (b) Differential conductance spectra were measured at 5 different atomic sites in (a).

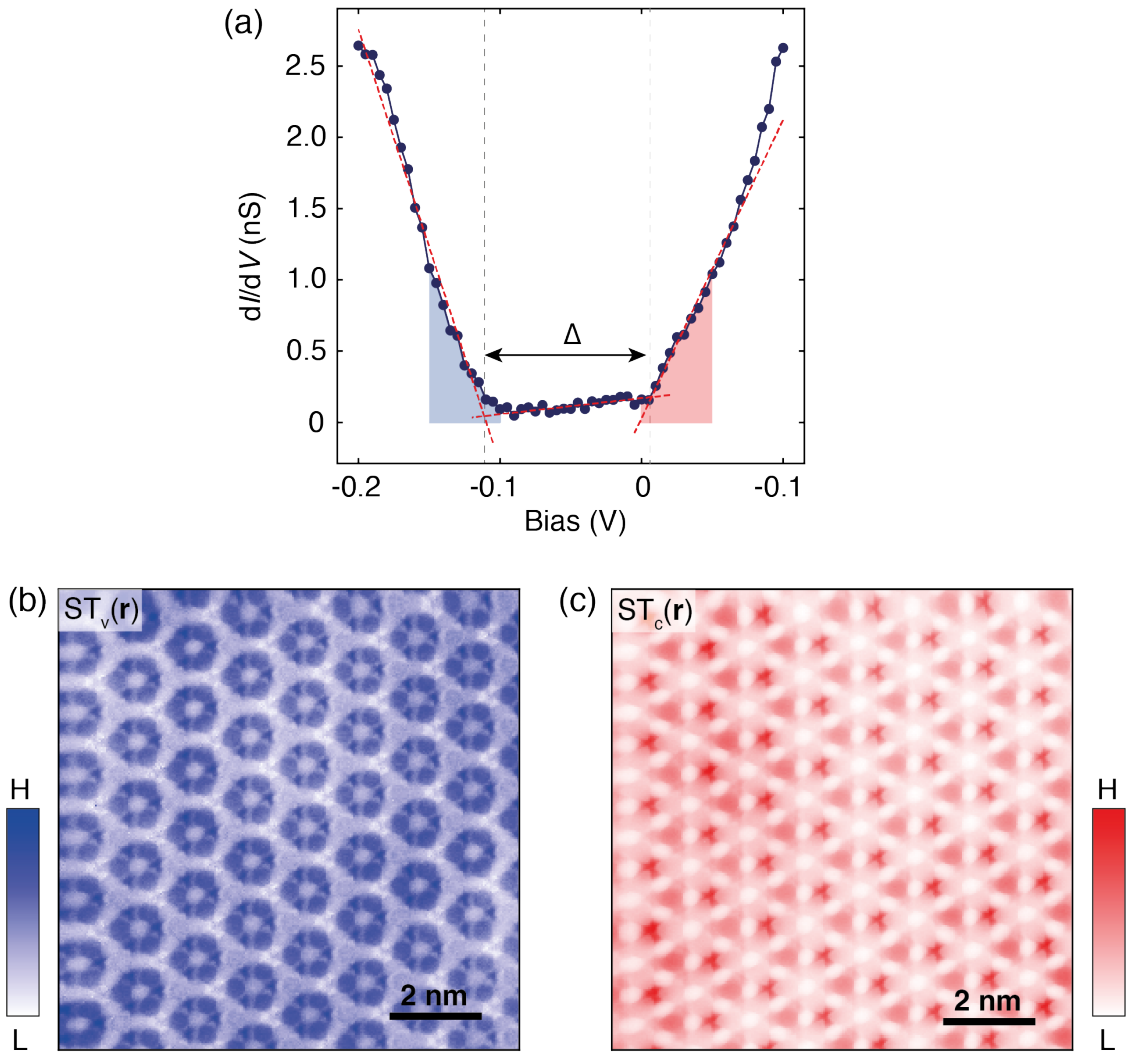

Figure 6.6: (a) A typical differential conductance spectrum. The Blue (red) shaded area defines the valence (conduction) band spectral weight. Red dashed lines are linear fittings of the filled and empty bands and the gap floor. The energy difference between the intersection points is defined as the excitonic energy gap. (b) Valence band spectral weight image. (c) Conduction band spectral weight image.

dashed rhombus. It is clear that, within the CDW unit cell, two types of Ti atoms and Se atoms are distinguished by charge depletion or accumulation. The existence of charge transfer is clear since, in the normal state, one would expect to have 4 Ti atoms visible in $\mathrm{ST}_c(\mathbf{r})$ and 4 Se atoms visible $\mathrm{ST}_v(\mathbf{r})$ within a CDW unit cell. However, looking at the Se atom labelled 1; the electrons are transferred from the Se atom to the three surrounding Ti atoms, which could be attributed to the formation of localised excitons between the Ti and Se atoms.

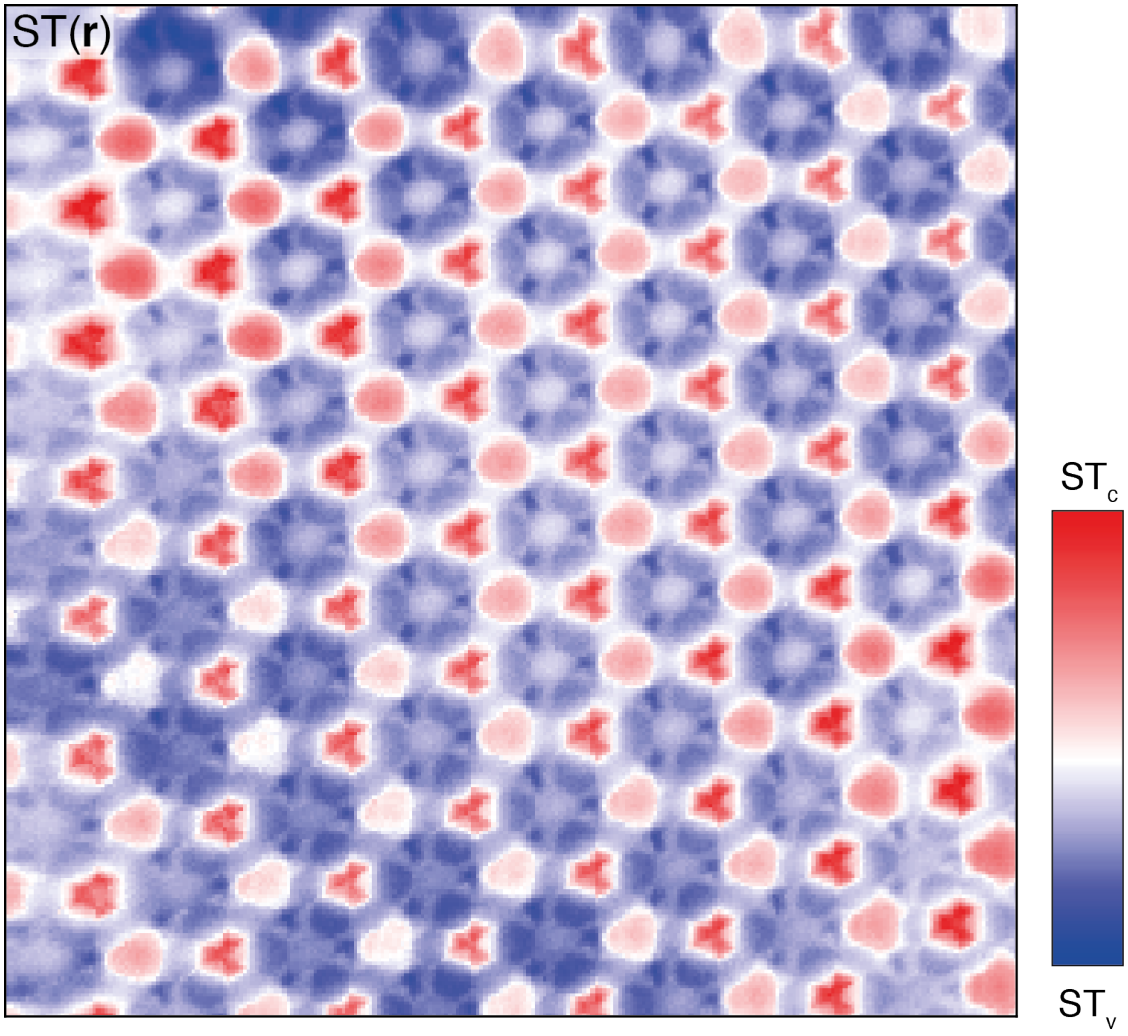

Figure 6.7: Total spectral weight transfer image defined as $\mathrm{ST}(\mathbf{r}) = \mathrm{ST}_v(\mathbf{r}) + \alpha \mathrm{ST}_c(\mathbf{r})$ where α is the scaling factor.

Imaging the energy gap variations

Second, the energy gap is visualised in the same FOV as Fig. 6.7(a) by extracting the gap value in the single-particle tunnelling spectrum at every atomic position $\mathbf{r}$. We use the standard gap extraction procedure by linearly fitting the filled and empty bands as well as the gap floor and then assigning the energy difference between the intersection points as the gap value [88]. A typical differential conductance spectrum that illustrates this procedure is shown in Fig. 6.5(a). The gap edges used as inputs of the linear fittings are determined by the eye from the spatially averaged $\mathrm{d}I/\mathrm{d}V$ spectrum. The resulting gap map $\Delta(\mathbf{r})$ is shown in Fig. 6.8. The

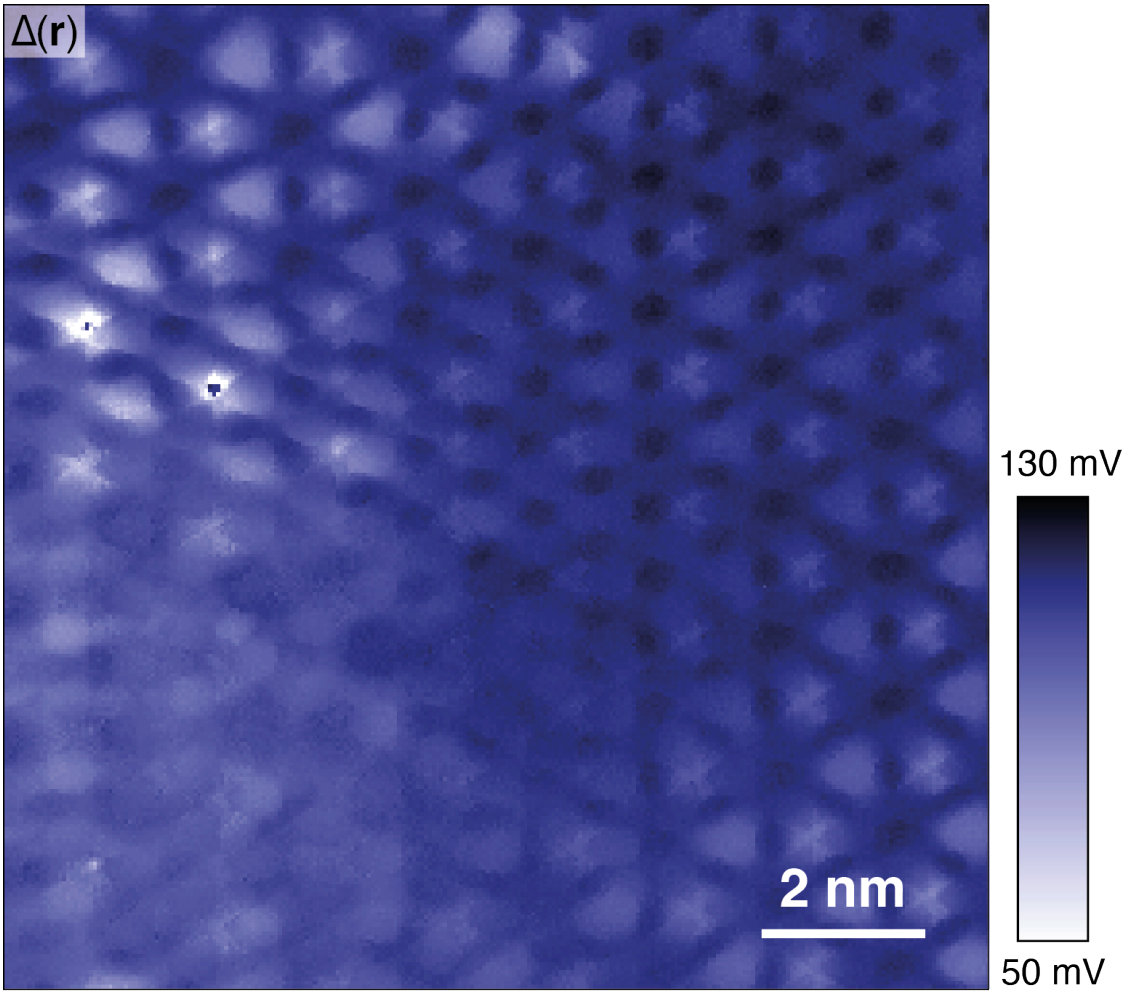

Figure 6.8: Image of the excitonic gap that is highly heterogeneous.

Fourier transform of the gap map reveals both atomic Bragg peaks and modulations at the $2a_0$-CDW wavevectors. This differs from the homogeneous Peierls CDW gap, where no electron-electron correlation is involved.

Similarly, by averaging the CDW unit cell over the entire gap FOV, we have the averaged gap image 6.9(b). By comparing with the spectral weight transfer image in the same FOV on the left side, it is evident that the gap value is low wherever the spectral weight is high. This can be interpreted as a smaller gap value facilitating charge transfer and thereby enhancing exciton formation.

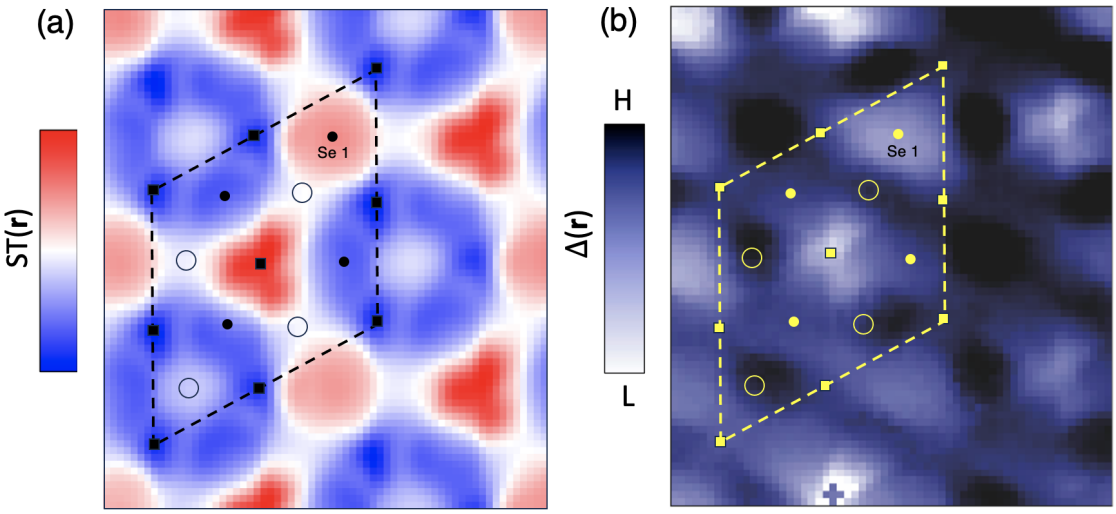

Figure 6.9: (a) Total spectral weight transfer map averaged over the entire FOV in Fig. 6.7. Black dashed rhombus indicates a CDW unit cell. Black solid circles indicate the upper Se atoms, black solid squares indicate the Ti atoms and open black circles indicate the bottom Se atoms which are not seen by STM. (b) The gap map averaged over the entire FOV in Fig. 6.8. Yellow dashed rhombus indicates a CDW unit cell. Yellow solid circles indicate the upper Se atoms, yellow solid squares indicate the Ti atoms, and open yellow circles indicate the bottom Se atoms. Note that the labelled atomic locations are proposed ones. Further experiments on simultaneous high-resolution topographies are needed for precise atomic registration.

6.3 Summary and outlook

Using spectroscopic imaging STM, I have shown direct visualisation of the charge transfer processes between the Ti and Se atoms associated with exciton formation. Although a detailed comparison with the schematic of real-space charge transfer image in Fig. 6.4 shows some difference, observation of two types of Ti atoms and Se atoms is agreed. Moreover, the heterogeneous nature of the energy gap image reveals that electronic correlation plays an important role and suggests the CDW formation in 1T-$TiSe_2$ is likely to originate from the electronic nature rather than the phonon-mediated effects. There are also outstanding questions that remain to be answered. For example, what is the structural factor of the excitons? Are there other broken symmetries associated with exciton formation besides the broken translational symmetry, such as chirality? At the time this thesis is being written, the experiment is still ongoing, and I hope to address these interesting questions soon.

Appendices

A

Method for extracting the supermodulation phase

The quasi-periodic crystal supermodulation is clearly observed in the topographic image $T(\mathbf{r})$ of the BiO layer of Bi-2212. This modulation pattern can be parameterized as

$$T'(\mathbf{r}) = A_s(\mathbf{r}) \cos \Phi(\mathbf{r}), \tag{A.1}$$

$$\Phi(\mathbf{r}) = \mathbf{Q_s} \cdot \mathbf{r} + \theta(\mathbf{r}), \tag{A.2}$$

where $\mathbf{Q_s}$ is the supermodulation wavevector, $\Phi(\mathbf{r})$ is the total phase and $\theta(\mathbf{r})$ represents the phase disorder. In order to extract $\Phi(\mathbf{r})$, the topographic image $T(\mathbf{r})$ is first Fourier-filtered that only keeps wavevectors near $\mathbf{q} = \pm\mathbf{Q}_s$. This process can be expressed as

$$T'(\mathbf{r}) = \frac{1}{\sigma\sqrt{2\pi}} \int T(\mathbf{q}) \left(e^{\frac{|\mathbf{q}-\mathbf{Q_s}|^2}{2\sigma^2}} + e^{\frac{|\mathbf{q}+\mathbf{Q_s}|^2}{2\sigma^2}} \right) \exp(-i\mathbf{q} \cdot \mathbf{r}) \mathrm{d}\mathbf{q} \tag{A.3}$$

where $T(\mathbf{q})$ is the Fourier transform of $T(\mathbf{r})$.

Next, to quantify the phase disorder $\theta(\mathbf{r})$, a method based on the principle of the lock-in amplifier is used [109]. Here, the Fourier-filtered image $T'(\mathbf{r})$ is multipulied by the reference modulations $\alpha(\mathbf{r}) = \sin(\mathbf{Q}_s \cdot \mathbf{r})$ and $\beta(\mathbf{r}) = \cos(\mathbf{Q}_s \cdot \mathbf{r})$ respectively, resulting

$$X(\mathbf{r}) \equiv T'(\mathbf{r})\alpha(\mathbf{r}) \tag{A.4}$$

$$Y(\mathbf{r}) \equiv T'(\mathbf{r})\beta(\mathbf{r}). \tag{A.5}$$

Then after applying a low-pass filter to the product images that removes the a.c. term, the phase disorder can be expressed as

$$\theta(\mathbf{r}) = \arctan\left(\frac{Y(\mathbf{r})}{X(\mathbf{r})}\right). \tag{A.6}$$

Finally, the total phase modulation image can be obtained by adding back the perfect modulation $\mathbf{Q}_\mathrm{s} \cdot \mathbf{r}$, yielding $\Phi(\mathbf{r}) = [\mathbf{Q}_s \cdot \mathbf{r} + \theta(\mathbf{r})] \bmod 2\pi$ (as shown in Fig. 5.9(b)).

B

Visualising the charge transfer energy $\mathcal{E}$

B.1 The setup effect

In visualising the supermodulation-induced charge-transfer energy variations, the setup effect's influence must be carefully considered. From Chapter 2, the topographic image is expressed as

$$T\left(\mathbf{r}, V_S\right) = \mathrm{T}_0 \ln\left[\int_0^{E=eV_S} N(\mathbf{r}, E)dE\right] \tag{B.1}$$

where $N(\mathbf{r}, E)$ is the sample LDOS and V_s is the set-up bias voltage. The differential conductance is expressed as

$$g(\mathbf{r}, V) = eI_s N(\mathbf{r}, E) / \int_0^{eV_s} N(\mathbf{r}, E)dE. \tag{B.2}$$

Here, the differential conductance $g(\mathbf{r}, V)$ is only proportional to the sample LDOS provided that the denominator of Eqn. B.2 is homogeneous. Since the integrated LDOS term is also present in the topography (Eqn. B.1), any significant modulations of the Bi-2212 crystal supermodulation would then modulate $\int_0^{eV_s} N(\mathbf{r}, E)dE$ at the supermodulation wavevector $\mathbf{Q_s}$, rendering $g(\mathbf{r}, V)$ not being proportional to $N(\mathbf{r}, E)$. This is the "setup effect".

To analyse this effect in our charge-transfer energy visualisation, we simulate the effects by multiplying a typical differential conductance image $g(\mathbf{r}, V)$ by a

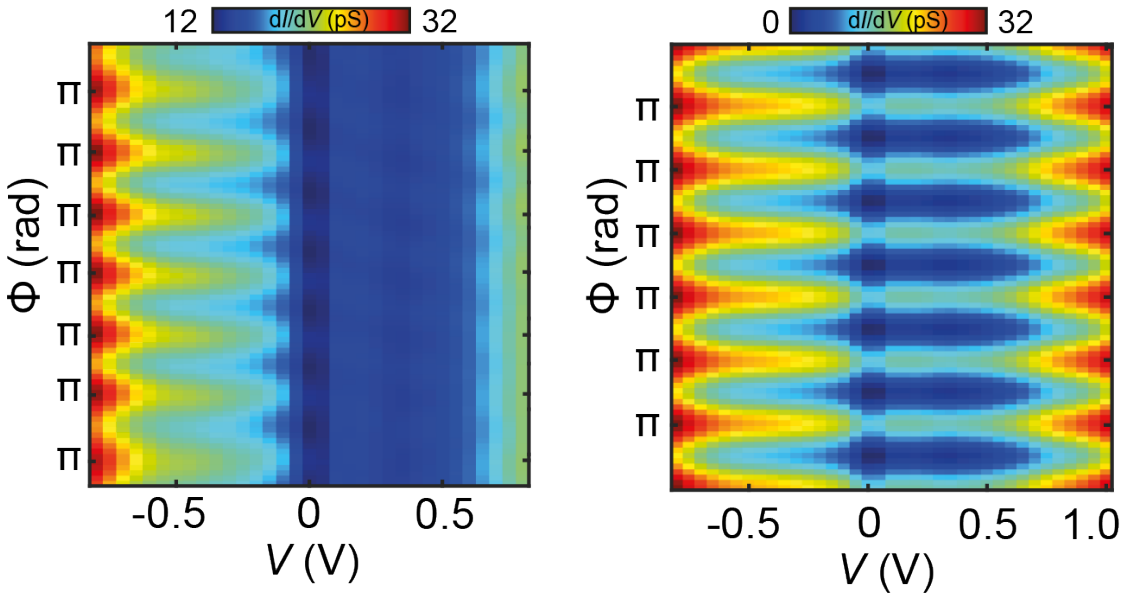

Figure B.1: (a) Spectrogram reproduced from Fig. 5.11(c). Modulations of the lower filled bands are clearly visible. The upper empty states modulate very weakly. (b) Simulated spectrogram that would occur due to a setup effect arising from the topographic supermodulation. Both the filled and empty states modulate strongly.

periodic function $A\cos(\mathbf{Q}_s \cdot \mathbf{r})$ that simulates the supermodulation presented in the topography. The simulated spectrogram is shown in Fig. B.1 (b). If the setup effect caused by the topographic supermodulation is the dominant phenomenon, the two images in Fig. B.1 would look very similar. However, upon close comparison, it is clear that the prominent modulation at $\mathbf{Q_s}$ in the conduction band of the simulated data is virtually non-existent in the experimental data. This demonstrates that the setup effect is not the predominant feature of the modulations at $\mathbf{Q_s}$ in the measured $g(\mathbf{r}, V)$ data.

B.2 Defining the charge-transfer gap

In our studies, the charge-transfer energy $\mathcal{E}$ is defined as the energy separation between the edges of the valence and conduction bands at a constant differential conductance $G = 20$ pS as shown in Fig. 5.11(b). The reasons for this definition are explained below.

First, it is important to realise that the $\mathcal{E}(\mathbf{r})$ variations at $\mathbf{Q_s}$ are not dependent on any specific chosen G value. For instance, $\mathcal{E}(\mathbf{r})$ images that are extracted from

different values of G ranging from 20 pS to 80 pS are shown in Fig. B.2. The variations in the spatial structure of the charge-transfer energy is very similar in $\mathcal{E}(\mathbf{r})$ images defined with different choices of G. This is evident in the power spectrum density Fourier transform of $\mathcal{E}(\mathbf{r})$ which shows clear $\pm\mathbf{Q_s}$ peaks. This implies that the connection between $\mathcal{E}$ and the supermudulation phase Φ will be consistent for any G examined in this context, though there might be variations in the amplitude of $\mathcal{E}$. Second, Oxygen dopants cause strong peaks in the differential conductance spectrum in the range 40 pS $< G <$ 80 pS, resulting in inaccurate estimation of $\mathcal{E}$. This is another reason for choosing $G = 20$ pS, where the dopant-atom complication is kept at a minimum.

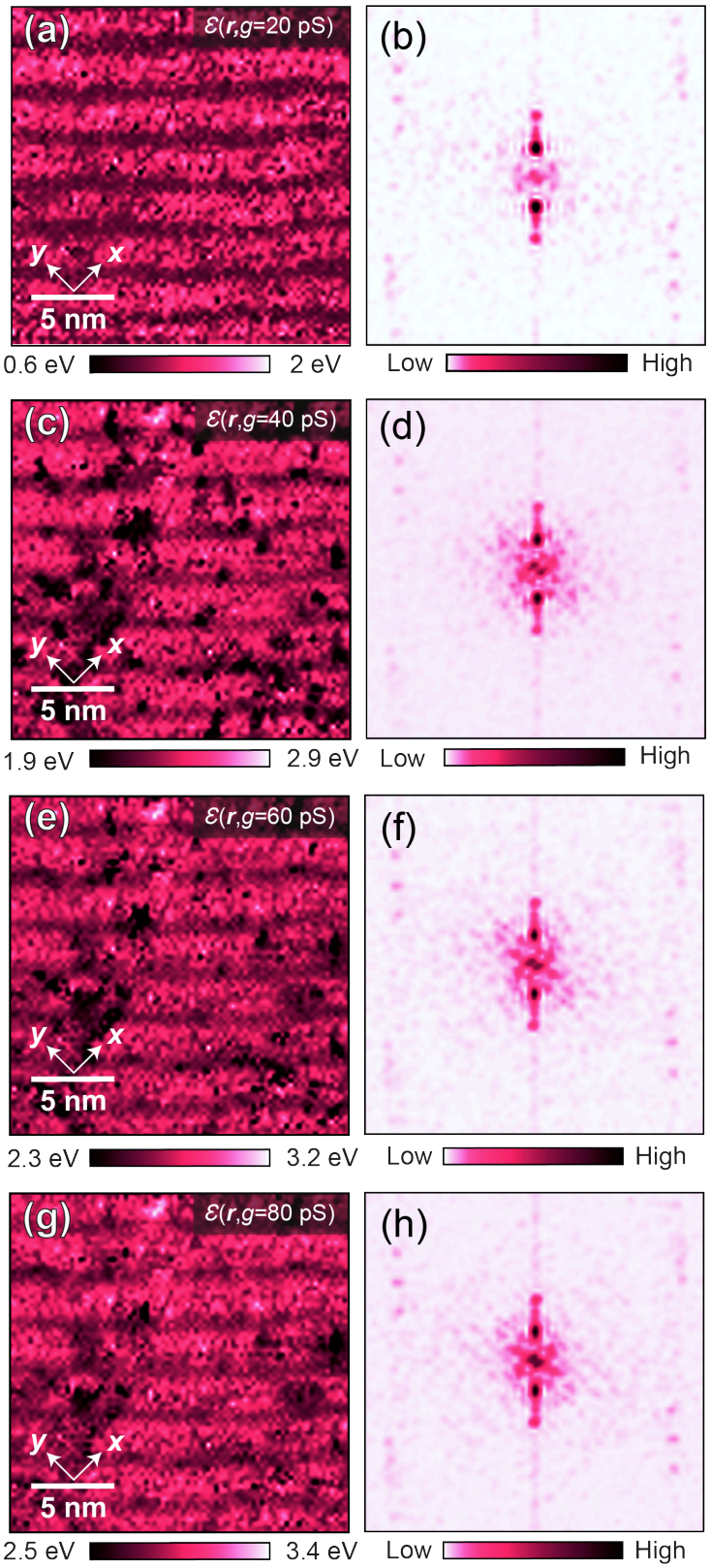

Figure B.2: $\mathcal{E}(G, \mathbf{r})$ images defined at constant differential conductance of (a): 20 pS, (c): 40 pS, (e): 60 pS and (g): 80 pS. (b), (d), (f) and (h) show the corresponding power spectrum density images that demonstrate clear $\mathbf{Q_s}$ peaks for different G values.

C

Evaluating the normal-state junction resistance $R_N(\mathbf{r})$

It is challenging to determine the normal state resistance R_N in the Josephson junction since the Josephson tunnelling current is measured in the range of several hundreds of μV but R_N is only quantifiable at 100 mV range (far away from the coherence peaks in the dI/dV spectrum of a SIS junction) where Ohmic $I-V$ behaviour is shown. Therefore, we adapt a two-step procedure where we first measure spectra at low voltage range (-15 mV $< V <$ 15 mV) $g_1(\mathbf{r}, V)$ with a setpoint $I_{s1} = 100$ pA, $V_{s1} = 15$ mV and spectra at high voltage range (-350 mV $< V <$ 350 mV) $g_2(\mathbf{r}, V)$ with a setpoint $I_{s2} = 350$ pA, $V_{s2} = 350$ mV. Then the normal state resistance of the low voltage spectra can be calculated from scaling that of the high voltage spectra. The detailed procedure is shown below:

1. $g_1(\mathbf{r}, V_J)$ is fit with a parabolic curve $g_1 = a_1 V_J^2 + b_1$ over the voltage range $[-V_{s1}, V_{s1}]$ at every position $\mathbf{r}$.

2. $g_2(\mathbf{r}, V_J)$ is fit with a parabolic curve $g_2 = a_2 V_J^2 + b_2$ over the voltage range $[-V_0, V_0]$, where 15 mV $< V <$ 50 mV.

3. The scaling factor between $g_2(\mathbf{r})$ and $g_1(\mathbf{r})$ is determined via the relation $g_1(\mathbf{r}) = g_2'(\mathbf{r}) = \alpha(\mathbf{r}) g_2(\mathbf{r}) + \beta(\mathbf{r})$, where $\alpha = \frac{a_1}{a_2}, \beta = b_1 - b_2 \frac{a_1}{a_2}$.

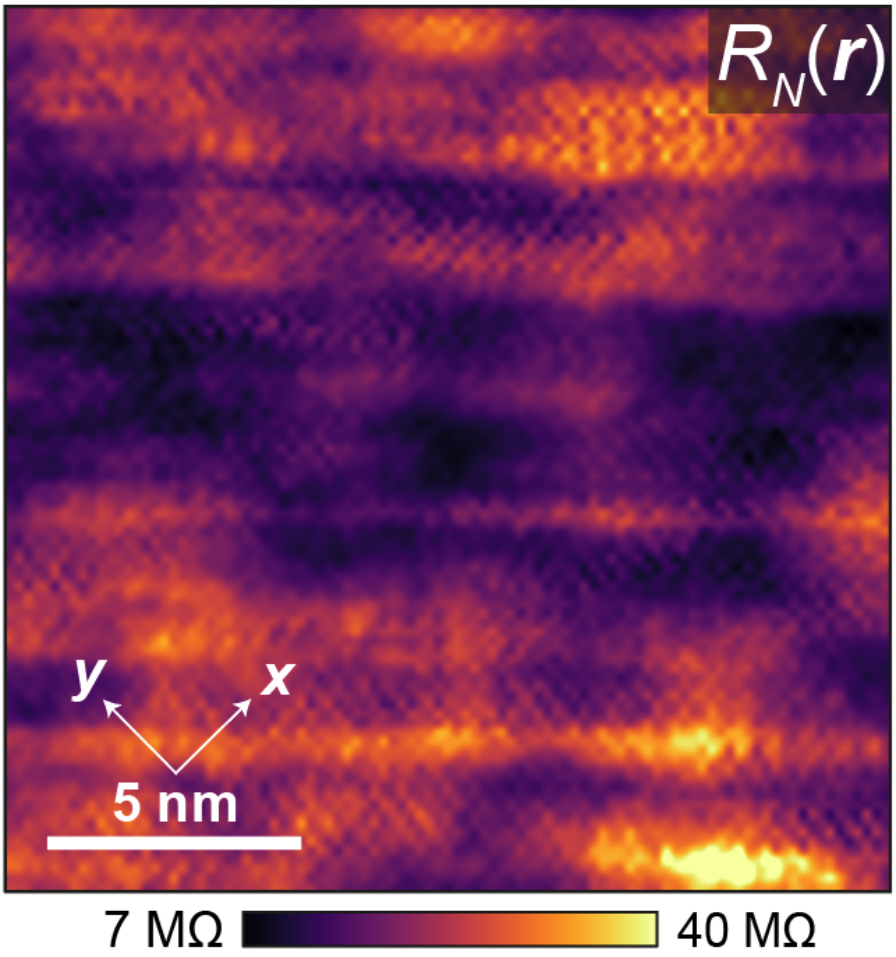

Figure C.1: Image of the normal-state junction resistance $R_N(r) \equiv 1/g_2'(r, V_{s2})$ at which the $g_1(\boldsymbol{r}, V_J)$ map was measured.

4. The normal state junction resistance of the low voltage difference conductance map $g_1(\mathbf{r}, V_J)$ can be calculated through $R_N(\mathbf{r}) \equiv \frac{1}{g_2'(\mathbf{r}, V_{s2})}$.

A image of the normal-state junction resistance in the same FOV of Fig. 5.11(d) is shown in Fig.C.1.

References

[1] R. P. Feynman, R. B. Leighton, and M. Sands. *The Feynman lectures on physics.* Vol. 3. Addison-Wesley, 1965.

[2] C. A. Reynolds et al. "Superconductivity of isotopes of mercury". *Physical Review* 78.4 (1950), p. 487.

[3] D. Feng and G. Jin. *Introduction to Condensed Matter Physics, Volume 1.* World Scientific Publishing Company, 2005.

[4] C. N. Yang. "Concept of off-diagonal long-range order and the quantum phases of liquid He and of superconductors". *Reviews of Modern Physics* 34.4 (1962), p. 694.

[5] C. C. Tsuei and J. R. Kirtley. "Pairing symmetry in cuprate superconductors". *Reviews of Modern Physics* 72.4 (2000), p. 969.

[6] J. Bardeen, L. N. Cooper, and J. R. Schrieffer. "Microscopic theory of superconductivity". *Physical Review* 106.1 (1957), p. 162.

[7] L. N. Cooper. "Bound electron pairs in a degenerate Fermi gas". *Physical Review* 104.4 (1956), p. 1189.

[8] J. G. Bednorz and K. A. Müller. "Possible high-T_c superconductivity in the Ba-La- Cu- O system". *Zeitschrift für Physik B Condensed Matter* 64.2 (1986), pp. 189–193.

[9] W. L. McMillan. "Transition temperature of strong-coupled superconductors". *Physical Review* 167.2 (1968), p. 331.

[10] A. Schilling et al. "Superconductivity above 130 k in the Hg–Ba–Ca–Cu–O system". *Nature* 363.6424 (1993), pp. 56–58.

[11] E. Fradkin, S. A. Kivelson, and J. M. Tranquada. "Colloquium: theory of intertwined orders in high temperature superconductors". *Reviews of Modern Physics* 87.2 (2015), p. 457.

[12] S. E. Barrett et al. "^{63}Cu Knight shifts in the superconducting state of $YBa_2Cu_3O_{7-\delta}$ (T_c= 90 K)". *Physical Review B* 41.10 (1990), p. 6283.

[13] M. Hashimoto et al. "Energy gaps in high-transition-temperature cuprate superconductors". *Nature Physics* 10.7 (2014), pp. 483–495.

[14] H. Ding et al. "Angle-resolved photoemission spectroscopy study of the superconducting gap anisotropy in $Bi_2Sr_2CaCu_2O_{8+x}$". *Physical Review B* 54.14 (1996), R9678–R9681.

[15] T. Xiang and C. Wu. *D-wave superconductivity.* Cambridge University Press, 2022.

[16] V. J. Emery and S. A. Kivelson. "Importance of phase fluctuations in superconductors with small superfluid density". *Nature* 374.6521 (1995), pp. 434–437.

[17] Y. J. Uemura et al. "Universal correlations between T_c and $\frac{n_s}{m^*}$ (carrier density over effective mass) in high-T_c cuprate superconductors". *Physical Review Letters* 62.19 (1989), p. 2317.

[18] B. Keimer et al. "From quantum matter to high-temperature superconductivity in copper oxides". *Nature* 518.7538 (2015), pp. 179–186.

[19] S. Wang et al. "Scattering interference signature of a pair density wave state in the cuprate pseudogap phase". *Nature Communications* 12.1 (2021), p. 6087.

[20] S. Martin et al. "Normal-state transport properties of $Bi_{2+x}Sr_{2-y}CuO_{6+\delta}$ crystals". *Physical Review B* 41.1 (1990), p. 846.

[21] P. W. Anderson. "The resonating valence bond state in La_2CuO_4 and superconductivity". *Science* 235.4793 (1987), pp. 1196–1198.

[22] B. Edegger, V. N. Muthukumar, and C. Gros. "Gutzwiller–RVB theory of high-temperature superconductivity: Results from renormalized mean-field theory and variational Monte Carlo calculations". *Advances in Physics* 56.6 (2007), pp. 927–1033.

[23] M. R. Norman. "Unconventional superconductivity". *arXiv preprint arXiv:1302.3176* (2013).

[24] V. J. Emery. "Theory of high-T_c superconductivity in oxides". *Physical Review Letters* 58.26 (1987), p. 2794.

[25] F. C. Zhang and T. M. Rice. "Effective Hamiltonian for the superconducting Cu oxides". *Physical Review B* 37.7 (1988), p. 3759.

[26] M. Sigrist. "Introduction to unconventional superconductivity". *AIP Conference Proceedings*. Vol. 789. 1. American Institute of Physics. 2005, pp. 165–243.

[27] G. Binnig et al. "Surface studies by scanning tunneling microscopy". *Physical Review Letter* 49.1 (1982), p. 57.

[28] Ø. Fischer et al. "Scanning tunneling spectroscopy of high-temperature superconductors". *Reviews of Modern Physics* 79.1 (2007), p. 353.

[29] J. Tersoff and D. R. Hamann. "Theory of the scanning tunneling microscope". *Phys. Rev. B* 31 (2 Jan. 1985), pp. 805–813.

[30] J. Bardeen. "Tunnelling from a many-particle point of piew". *Physical Review Letter* 6 (2 Jan. 1961), pp. 57–59.

[31] J. Ge, M. Ovadia, and J. E Hoffman. "Achieving low noise in scanning tunneling spectroscopy". *Review of Scientific Instruments* 90.10 (2019).

[32] C. K. Kim. "Complementary visualization of the pseudogap states in $Bi_2Sr_2CaCu_2O_{8+x}$: SI-STM study in real and momentum space". PhD thesis. Cornell University, May 2013.

[33] M. H. Hamidian et al. "Detection of a Cooper-pair density wave in $Bi_2Sr_2CaCu_2O_{8+x}$". *Nature* 532.7599 (2016), pp. 343–347.

[34] X. Liu et al. "Discovery of a Cooper-pair density wave state in a transition-metal dichalcogenide". *Science* 372.6549 (2021), pp. 1447–1452.

[35] D. Cho et al. "A strongly inhomogeneous superfluid in an iron-based superconductor". *Nature* 571.7766 (2019), pp. 541–545.

[36] S. M. O'Mahony et al. "On the electron pairing mechanism of copper-oxide high temperature superconductivity". *Proceedings of the National Academy of Sciences* 119.37 (2022), e2207449119.

[37] B. D. Josephson. "Possible new effects in superconductive tunnelling". *Physics Letters* 1.7 (1962), pp. 251–253.

[38] P. W. Anderson and J. M. Rowell. "Probable observation of the Josephson superconducting tunneling effect". *Physical Review Letters* 10.6 (1963), p. 230.

[39] J. Clarke and A. I. Braginski. *The SQUID handbook*. Vol. 1. Wiley Online Library, 2004.

[40] H. Ohta, H. D. Hahlbohm, and H. Lübbig. "A self-consistent model of the Josephson junction". *IC SQUID* 76 (1976), pp. 35–49.

[41] V. Ambegaokar and A. Baratoff. "Tunneling between superconductors". *Physical Review Letters* 10.11 (1963), p. 486.

[42] F. Tafuri. *Fundamentals and frontiers of the Josephson effect*. Vol. 286. Springer Nature, 2019.

[43] Y. M. Anchenko and L. A. Zil'Berman. "The Josephson effect in small tunnel contacts". *Soviet Phys. JETP* 28 (1969).

[44] S. H. Pan and J. C. Davis. "^{3}He refrigerator based very low temperature scanning tunneling microscope". *Review of scientific instruments* 70.2 (1999), pp. 1459–1463.

[45] R. C. Richardson. *Experimental techniques in condensed matter physics at low temperatures*. Boca Raton: CRC Press, 1988.

[46] F. Pobell. *Matter and methods at low temperatures*. Springer Science & Business Media, 1996.

[47] R. Sharma. "Advanced quasiparticle interference imaging for complex superconductors". PhD thesis. Cornell University, 2020.

[48] E. Berg et al. "Striped superconductors: how spin, charge and superconducting orders intertwine in the cuprates". *New Journal of Physics* 11.11 (2009), p. 115004.

[49] D. F. Agterberg et al. "The physics of pair-density waves: Cuprate superconductors and beyond". *Annual Review of Condensed Matter Physics* 11 (2020), pp. 231–270.

[50] D. Saint-James, G. Sarma, and E. J. Thomas. *Type II Superconductivity*. Commonwealth and International Library. Liberal Studies Divi. Elsevier Science & Technology, 1969.

[51] Y. Matsuda and H. Shimahara. "Fulde–Ferrell–Larkin–Ovchinnikov state in heavy fermion superconductors". *Journal of the Physical Society of Japan* 76.5 (2007), p. 051005.

[52] P. Fulde and R. A. Ferrell. "Superconductivity in a strong spin-exchange field". *Physical Review* 135.3A (1964), A550.

[53] R. Casalbuoni and G. Nardulli. "Inhomogeneous superconductivity in condensed matter and QCD". *Reviews of Modern Physics* 76.1 (2004), p. 263.

[54] A. I. Larkin. "Inhomogeneous state of superconductors". *Sov. Phys. JETP* 20 (1965), p. 762.

[55] P. M. Lozano et al. "Experimental evidence that zinc impurities pin pair-density-wave order in $La_{2-x}Ba_xCuO_4$". *Physical Review B* 103.2 (2021), p. L020502.

[56] E. Berg et al. "Dynamical layer decoupling in a stripe-ordered high-T_c superconductor". *Physical Review Letters* 99.12 (2007), p. 127003.

[57] B. Nachumi et al. "Muon spin relaxation studies of Zn-substitution effects in high-T_c cuprate superconductors". *Physical Review Letters* 77.27 (1996), p. 5421.

[58] S. H. Pan et al. "Imaging the effects of individual zinc impurity atoms on superconductivity in $Bi_2Sr_2CaCu_2O_{8+\delta}$". *Nature* 403.6771 (2000), pp. 746–750.

[59] A. Himeda, T. Kato, and M. Ogata. "Stripe states with spatially oscillating d-wave superconductivity in the two-dimensional $t - t' - J$ model". *Physical Review Letters* 88.11 (2002), p. 117001.

[60] M. Raczkowski et al. "Unidirectional d-wave superconducting domains in the two-dimensional $t - J$ model". *Physical Review B* 76.14 (2007), p. 140505.

[61] K-Y. Yang et al. "Nature of stripes in the generalized $t - J$ model applied to the cuprate superconductors". *New Journal of Physics* 11.5 (2009), p. 055053.

[62] F. Loder et al. "Mean-field pairing theory for the charge-stripe phase of high-temperature cuprate superconductors". *Physical Review Letters* 107.18 (2011), p. 187001.

[63] P. Corboz, T. M. Rice, and M. Troyer. "Competing states in the $t - J$ model: Uniform D-wave state versus stripe state". *Physical Review Letters* 113.4 (2014), p. 046402.

[64] S. S. Dash and D. Sénéchal. "Charge-and pair-density-wave orders in the one-band Hubbard model from dynamical mean field theory". *Physical Review B* 103.4 (2021), p. 045142.

[65] S. Yoshida, K. Yada, and Y. Tanaka. "Theory of a pair density wave on a quasi-one-dimensional lattice in the Hubbard model". *Physical Review B* 104.9 (2021), p. 094506.

[66] P. Mai et al. "Intertwined spin, charge, and pair correlations in the two-dimensional Hubbard model in the thermodynamic limit". *Proceedings of the National Academy of Sciences* 119.7 (2022), e2112806119.

[67] E. Koch. "Exchange mechanisms". *Correlated electrons: from models to materials* 2 (2012), pp. 1–31.

[68] J. C. Davis. *On the electron pairing mechanism of copper-oxide high-temperature superconductivity.* Condensed Matter Seminar at the University of Illinois at Urbana-Champaign. 2021.

[69] R. Coldea et al. "Spin waves and electronic interactions in La_2CuO_4". *Physical Review Letters* 86.23 (2001), pp. 5377–5380.

[70] D. Rybicki et al. "Perspective on the phase diagram of cuprate high-temperature superconductors". *Nature communications* 7.1 (2016), p. 11413.

[71] C. Weber et al. “Scaling of the transition temperature of hole-doped cuprate superconductors with the charge-transfer energy”. *Europhysics Letters* 100.3 (2012), p. 37001.

[72] N. Kowalski. “Dopage, température critique et étude du modèle de Hubbard à trois bandes”. PhD thesis. Master’s thesis, Université de Sherbrooke, Sherbrooke, QC, Canada, 2021.

[73] N. Kowalski et al. “Oxygen hole content, charge-transfer gap, covalency, and cuprate superconductivity”. *Proceedings of the National Academy of Sciences* 118.40 (2021), e2106476118.

[74] W. Metzner and D. Vollhardt. “Correlated lattice fermions in $d = \infty$ dimensions”. *Physical Review Letters* 62.3 (1989), p. 324.

[75] A. Georges et al. “Dynamical mean-field theory of strongly correlated fermion systems and the limit of infinite dimensions”. *Reviews of Modern Physics* 68.1 (1996), p. 13.

[76] J. W. Negele. *Quantum many-particle systems*. CRC Press, 2018.

[77] P. Coleman. *Introduction to many-body physics*. Cambridge University Press, 2015.

[78] T. Maier et al. “Quantum cluster theories”. *Reviews of Modern Physics* 77.3 (2005), p. 1027.

[79] C-H. Yee and G. Kotliar. “Tuning the charge-transfer energy in hole-doped cuprates”. *Physical Review B* 89.9 (2014), p. 094517.

[80] S. Acharya et al. “Metal-insulator transition in copper oxides induced by apex displacements”. *Physical Review X* 8.2 (2018), p. 021038.

[81] Y. Ohta, T. Tohyama, and S. Maekawa. “Electronic structure of insulating cuprates: Role of Madelung potential in the charge-transfer gap and superexchange interaction”. *Physica C: Superconductivity* 185 (1991), pp. 1721–1722.

[82] L. F. Feiner, M. Grilli, and C. Di Castro. “Apical oxygen ions and the electronic structure of the high-T_c cuprates”. *Physical Review B* 45.18 (1992), p. 10647.

[83] E. Pavarini et al. “Band-structure trend in hole-doped cuprates and correlation with $T_{c\,\max}$”. *Physical Review Letters* 87.4 (2001), p. 047003.

[84] K. Foyevtsova, R. Valentí, and P.J. Hirschfeld. “Effect of dopant atoms on local superexchange in cuprate superconductors: A perturbative treatment”. *Physical Review B* 79.14 (2009), p. 144424.

[85] Y. Tokura et al. “Cu-O network dependence of optical charge-transfer gaps and spin-pair excitations in single-CuO 2-layer compounds”. *Physical Review B* 41.16 (1990), p. 11657.

[86] S. L. Cooper et al. “Optical studies of gap, exchange, and hopping energies in the insulating cuprates”. *Physical Review B* 42.16 (1990), p. 10785.

[87] M. C. Aronson et al. “Pressure dependence of the superexchange interaction in antiferromagnetic La_2CuO_4”. *Physical Review B* 44.9 (1991), p. 4657.

[88] W. Ruan et al. “Relationship between the parent charge transfer gap and maximum transition temperature in cuprates”. *Science Bulletin* 61 (2016), pp. 1826–1832.

[89] S-L. Yang et al. “Revealing the Coulomb interaction strength in a cuprate superconductor”. *Physical Review B* 96.24 (2017), p. 245112.

[90] M. Le Tacon et al. “Intense paramagnon excitations in a large family of high-temperature superconductors”. *Nature Physics* 7.9 (2011), pp. 725–730.

[91] Y. Y. Peng et al. “Influence of apical oxygen on the extent of in-plane exchange interaction in cuprate superconductors”. *Nature Physics* 13.12 (2017), pp. 1201–1206.

[92] G. Levy et al. “Experimental determination of superexchange energy from two-hole spectra”. *arXiv preprint arXiv:2107.09181* (2021).

[93] P. Mai et al. “Pairing correlations in the cuprates: A numerical study of the three-band Hubbard model”. *Physical Review B* 103.14 (2021), p. 144514.

[94] J. A Slezak et al. “Imaging the impact on cuprate superconductivity of varying the interatomic distances within individual crystal unit cells”. *Proceedings of the National Academy of Sciences* 105.9 (2008), pp. 3203–3208.

[95] D. Grebille et al. “Static disorder in the incommensurate structure of the high T_c superconductor $Bi_2Sr_2CaCu_2O_{8+\delta}$”. *Acta Crystallographica Section B: Structural Science* 52.4 (1996), pp. 628–642.

[96] W. Kohn and D. Sherrington. “Two kinds of bosons and Bose condensates”. *Reviews of Modern Physics* 42.1 (1970), p. 1.

[97] B. I. Halperin and T. M. Rice. “Possible anomalies at a semimetal-semiconductor transistion”. *Reviews of Modern Physics* 40.4 (1968), p. 755.

[98] J. P. Eisenstein and A. H. MacDonald. “Bose–Einstein condensation of excitons in bilayer electron systems”. *Nature* 432.7018 (2004), pp. 691–694.

[99] A. Kogar et al. “Signatures of exciton condensation in a transition metal dichalcogenide”. *Science* 358.6368 (2017), pp. 1314–1317.

[100] T. Kaneko. “Theoretical study of excitonic phases in strongly correlated electron systems”. PhD thesis. Chiba University, 2016.

[101] J. A. Wilson. “Modelling the contrasting semimetallic characters of TiS_2 and $TiSe_2$”. *Physica Status Solidi (b)* 86.1 (1978), pp. 11–36.

[102] G. Li et al. “Semimetal-to-Semimetal Charge Density Wave Transition in $1T - TiSe_2$”. *Physical Review Letters* 99.2 (2007), p. 027404.

[103] J. C. E. Rasch et al. “$1T$- $TiSe_2$: Semimetal or Semiconductor?” *Physical Review Letters* 101.23 (2008), p. 237602.

[104] R. A. Craven, F. J. Di Salvo, and F. S. L. Hsu. “Mechanisms for the 200 K transition in $TiSe_2$: A measurement of the specific heat”. *Solid State Communications* 25.1 (1978), pp. 39–42.

[105] F. J. Di Salvo, D. E. Moncton, and J. V. Waszczak. “Electronic properties and superlattice formation in the semimetal $TiSe_2$”. *Physical Review B* 14.10 (1976), p. 4321.

[106] C. Monney et al. “Probing the exciton condensate phase in $1T$-$TiSe_2$ with photoemission”. *New Journal of Physics* 12.12 (2010), p. 125019.

[107] H. Cercellier et al. "Evidence for an excitonic insulator phase in $1T$-$TiSe_2$". *Physical Review Letters* 99.14 (2007), p. 146403.

[108] Y. Peng et al. "Observation of orbital order in the Van der Waals material $1T$-$TiSe_2$". *Physical Review Research* 4.3 (2022), p. 033053.

[109] J. A. Slezak. "Atomic-scale impact of unit cell dimensions on pairing in a high-temperature superconductor". PhD thesis. Cornell University, 2007.